A Micromachined Millimeter-Wave Radar Technology for Indoor Navigation

By

Meysam Moallem

A dissertation submitted in partial fulfillment
of the requirements for the degree of
Doctor of Philosophy
(Electrical Engineering)
in The University of Michigan
2014

Doctoral Committee:

Professor Kamal Sarabandi, Chair
Professor Mark A. Burns
Research Scientist Jack R. East
Professor Eric Michielssen
Emeritus Professor Kensall D. Wise

© Meysam Moallem
2014 All Rights Reserved

To my parents with love and gratitude.

ACKNOWLEDGEMENTS

First of all, I would like to sincerely thank my advisor, Professor Kamal Sarabandi, for all his support and encouragement throughout these years. I am truly grateful for having the opportunity to work with him and have always been inspired by his exceptional passion and perseverance towards research. I am deeply grateful to Dr. Jack East for his continuous assistance and support during these years. I would also like to thank Professor Kensall Wise, Professor Eric Michielssen, and Professor Mark Burns for their service on my dissertation committee.

I would like to specifically thank Dr. Mehrnoosh Vahidpour for her invaluable support and encouragement throughout the course of this work. I am truly grateful for having the opportunity to collaborate with her during the first three years of this project.

I would like to extend my gratitude to all my current and former group members, especially Armin Jam, Amr Alaa, Jiangfeng Wu, Hamid Nejati, Adel Elsherbini, Michael Benson, Young Jun Song, Fikadu Dagefu, Jungsuek Oh, Jacquelyn Vitaz, Michael Thiel, Ju Seop Lee, and Mojtaba Dehmollaian.

Experimental research cannot be completed without the assistance of many colleagues. I would like to thank Dr. Adib Nashashibi and Dr. Leland Pierce for their assistance and advice on technical and measurement problems. I would like to acknowledge all the staff and users in the Lurie nanofabrication facility (LNF), especially Jae Yoong Cho, Razi Haque, Greg Allion, Pilar Herrera-Fierro, Nadine Wang, Katharine Beach, Thomas Latowsky, Kevin Owen, Brian Armstrong, Onnop Srivannavit, Ali

Besharatian, Brian VanDerElzen, Robert Hower, and Siddharth Gaba for all their assistance, valuable ideas, and recommendations for the microfabrication process.

I would like to express my gratitude to all my friends in Radiation Laboratory and University of Michigan, and my Iranian friends in Ann Arbor.

Finally, I am most grateful to my family for their endless love and support throughout my life. In particular, I would like to give my greatest gratitude to my parents, Mahnaz Etehad Tavakol and Mehdi Moallem, to whom I owe everything that I have achieved in my life.

Meysam Moallem

December 2013

TABLE OF CONTENTS

DEDICATION ... **ii**

ACKNOWLEDGEMENTS ... **iii**

LIST OF FIGURES ... **viii**

LIST OF TABLES ... **xv**

LIST OF APPENDICES ... **xvi**

LIST OF ABBREVIATIONS ... **xvii**

ABSTARCT ... **xviii**

CHAPTER 1 INTRODUCTION ... **1**

1.1 Motivation ... 1

1.2 Current Navigation and Collision-Avoidance Sensors ... 4

1.2.1 LADAR Systems ... 4

1.2.2 SONAR Systems ... 6

1.2.3 UWB Systems ... 8

1.3 MMW Radar Technology ... 9

1.4 The MMW Micromachined Beam-Stearing Radar ... 11

1.5 MMW Radar Phenomenology in Indoor Environment ... 15

1.6 Dissertation Overview ... 17

CHAPTER 2 MICROMACHINED RADAR INTEGRATION ... **21**

1.7 MMW/THZ Design Challenges ... 23

1.8 Cavity-Backed CPW Lines ... 24

1.8.1 Design Characteristics ... 27

1.8.2 Design Optimization ... 28

1.9 Impedance-Taper Waveguide to CBCPW Transition ... 33

1.9.1 Characteristic Impedance in Waveguides ... 34

1.9.2 CBCPW to Reduced-Height Waveguide Transition ... 36

1.9.3 In-Plane Impedance Taper Transitions ... 37

1.10 Chip Integration ... 41

1.11 Directional Couplers ... 46

1.11.1 Waveguide Couplers ... 47

1.12 Summary ... 50

CHAPTER 3 THE MICROFABRICATION PROCESSES ... **51**

1.13 Bottom Wafer ... 53

1.13.1 DRIE Multistep etching ... 53

1.13.2 Backside Through Etch 59
1.13.3 Metalization 59

1.14 Top Wafer 60
1.14.1 Free-Standing Membrane 61
1.14.2 Gold Patterning 61
1.14.3 Membrane Release 62

1.15 Au-Au Thermocompression Bonding 63

1.16 Summary 64

CHAPTER 4 MMW AND SUB-MMW ON-WAFER MEASUREMENT METHODOLOGY 65

1.17 Introduction 65

1.18 Conventional Measurement Methods 66
1.18.1 GSG Probes 66
1.18.2 Test Fixtures 68

1.19 The On-Wafer Waveguide Probe Measurement Technique 69
1.19.1 E-Plane Step Transition 70
1.19.2 Waveguide Choke 71
1.19.3 Measurement Setup 74
1.19.4 Measurement Results 75

1.20 Chip Integration 77

1.21 The Non-Contact S-Parameter Measurement Technique for Characterization of Multi-Port Components 79
1.21.1 Theory 81
1.21.2 Coupling Slot Array Design 84
1.21.3 Match Load Design 88
1.21.4 Coupler Measurements 90
1.21.5 Sensitivity Analysis 94

1.22 Summary 96

CHAPTER 5 MMW IMAGE-REJECTION SPATIAL FILTER 98

1.23 Introduction 98
1.23.1 Frequency Selective Surfaces (FSS) 99

1.24 Image-Rejection Filter Circuit Design 103

1.25 The Patch-Wire MEFSS 105

1.26 Design Challenges 107

1.27 Design Analysis 109

1.28 Microfabrication Process 112

1.29 Free-Space Measurements 115

1.30 Summary 117

CHAPTER 6 MMW RADAR INDOOR PHENOMENOLOGY 119
1.31 Introduction 119
1.32 Instrumentation Y-band Radar System 120
1.32.1 Radar Front-End Module 121
1.32.2 Measurement Setup 122
1.33 Data Collection and Image Formation 123
1.34 Polarization Analysis 126
1.35 Mapping the Building Interior Layout 129
1.36 Image Processing and Feature Extraction 131
1.36.1 Linear Feature Extraction 131
1.36.2 Ghost Image Elimination 134
1.36.3 False Passage Blocking Elimination 135
1.37 Y-band Backscatter Measurements 136
1.37.1 Measurement Setup 137
1.37.2 Data Acquisition and Calibration 139
1.37.3 Results and Analysis 143
1.38 Summary 147
CHAPTER 7 CONCLUSIONS AND FUTURE WORK 149
1.39 Summary and Conclusions 149
1.40 Future work 152
APPENDICES 154
BIBLIOGRAPHY 174

LIST OF FIGURES

Figure 1.1 Micro robotic systems (a) a miniature autonomous rotorcraft (Mesicopter) [4], (b) An autonomous 2.4g crawling hexapod robot (RoACH) [5] 1

Figure 1.2 Autonoumous navigation in a complex setting 2

Figure 1.3 A typical scenario in indoor navigation... 4

Figure 1.4 A typical LADAR system block diagram [13]... 5

Figure 1.5 Commercial compact LADAR system for robotic applications [18]................ 6

Figure 1.6 The measured attenuation at optical band (a) fog, (b) smoke [19].................... 6

Figure 1.7 Commercial ultra-compact imaging SONAR (Power requirement: 12 - 48V DC at 4VA, weight: 324 grams) [26]... 7

Figure 1.8 UWB radar sensor unit [29] 8

Figure 1.9 (a) A 77 GHz FMCW CMOS transceiver with horn antennas [33], (b) A 94 GHz CMOS 3-D image radar engine with dish antenna [34] 10

Figure 1.10 (a) 60 GHz CMOS Doppler radar with integrated patch antennas (beamwidth> 40°) [31], (b) 77GHz FMCW radar system with patch array antennas (beamwidth = 9°) [35]... 11

Figure 1.11 Schemetic of the proposed micromachined radar 12

Figure 1.12 Block diagram of the proposed beam scanning 240 GHz navigation radar.. 14

Figure 1.13 Passive components for radar front-end integration..................................... 14

Figure 1.14 MMW attenuation in poor atmosphere (a) attunation due to dust in 1-m dust tunnel [45], (b) attenuation in moist air [46]... 16

Figure 2.1 The proposed radar front-end micromachined structure 22

Figure 2.2 The proposed radar front-end block diagram 23

Figure 2.3 The proposed cavity-backed CPW line; the optimized dimensions are: s = 210µm, g = 45µm, h = 46µm, w = 300µm. 26

Figure 2.4 Magnetic field distribution in (a) conventional 50 Ω CPW line on silicon substrate (b) cavity-backed CPW line. The color scale is the same for both figures. 26

Figure 2.5 Attenuation rate of the optimized CBCPW line using the MOM and HFSS simulations 31

Figure 2.6 Normalized phase velocity and characteristic impedance of the optimized line 32

Figure 2.7 Sensitivity of characteristic impedance of CBCPW line with respect to misalignement 32

Figure 2.8 The rectangular waveguide.. 35

Figure 2.9 CBCPW to reduced-height waveguide transition: (a) schematic (b) full-wave analysis results. Optimized waveguide width is w_r = 800μm. 37

Figure 2.10 Schematic of the in-plane wedge impedance taper 38

Figure 2.11 (a) Cross-sectionel view of the in-plane wedge impedance taper, (b) characteristic impedance versus width of the deep waveguide (w_t) (h_1 =46μm, h_2 =200μm)... 39

Figure 2.12 Complete 3-step transition: (a) schematic with optimized dimensions: t_r = 1000μm, t_1 = 2000μm, t_2 = 1500μm; (b) full-wave analysis results of the optimized structure.. 40

Figure 2.13 Integration of active circuits into metal blocks [64]..................................... 42

Figure 2.14 The required components for integration of MMIC chips with micromachined radar front-end.. 42

Figure 2.15 The proposed thru wafer chip integration configuration............................... 43

Figure 2.16 The proposed transition from MMIC chip to CBCPW line 44

Figure 2.17 Performance of the chip transition with respect to parameters *d* and *g* (a) insertion loss, (b) return loss 45

Figure 2.18 Illustration of wave coupling in an *n*-aperture coupler [65].......................... 47

Figure 2.19 Micromachined sidewall aperture couplers:.. 48

Figure 2.20 Simulated performance of the optimized couplers: (a) 230-245 GHz 10-dB coupler, (b) Full-band 10-dB coupler, (c) Full-band 3-dB coupler 50

Figure 3.1 General diagram of the radar microfabrication processes: (a) The bottom wafer, (b) The top wafer, (c) Bonded wafers.. 52

Figure 3.2 Multi-step etching using the multi-mask method [36] 54

Figure 3.3 SEM photo of the transition between DRIE steps.. 54

Figure 3.4 Process flow diagram of multistep etching using glass reflow technique....... 56

Figure 3.5 Waveguide trenches filled with glass 57

Figure 3.6 Multi-step structures fabricated using glass-in-silicon reflow technique........ 57

Figure 3.7 Sidewall profile after oxidation 58

Figure 3.8 The bottom wafer after metallization (a) couplers, (b) chip integration transitions.. 60

Figure 3.9 Process flow diagram of lift-off process 62

Figure 3.10 Top wafer after membrane release (a) The membrane supported CBCPW line and the waveguide to CBCPW transition (top view), (b) slot array antennas (back view) (see Chapter 4) 63

Figure 3.11 Cross-section of diced waveguide sections (a) outside view (b) inside view 64

Figure 4.1 (a) GSG probe measurement setup (220GHz-325 GHz), (b) the probe tips in contact with the on-wafer pads 67

Figure 4.2 Examples of test fixtures for characterization of micromachined components [64, 74] 68

Figure 4.3 Schematic of the proposed waveguide probe measurement technique 69

Figure 4.4 E-plane transition (a) schematic (b) full-wave analysis results of the optimized structure ($h_b = w_b$= 230μm, l_t =540μm) 70

Figure 4.5 Cross section view of the waveguide choke 72

Figure 4.6 The optimized choke design with the parameters specified for WR-3 waveguide 72

Figure 4.7 Performance of the choke connection with 20μm gap between the two surfaces 73

Figure 4.8 Choke milled on the cross-section of waveguide probe 73

Figure 4.9 (a) The waveguide probe measurement setup (b) custom-made WR-3 waveguide probe 74

Figure 4.10 On-wafer waveguide calibration kits. The calibration kits includes three standards (shorts, line, and thru) to perform TRL calibration. Calibration kit #1 calibrates the system up to the on-wafer waveguides. Calibration kit #2 calibrates the system up to the CBCPW lines. 75

Figure 4.11 (a) Calibrated measurement of an on-wafer waveguide section (length=1cm) (b) Simulated and measured reflection and transmission coefficients of back-to-back CBCPW to rectangular waveguide transition 76

Figure 4.12 Simulated and measured attenuation of the CBCPW line 77

Figure 4.13 Delay lines implemented on 55 μm thick InP with the old launch pad design 78

Figure 4.14 The top view of the thru-wafer transition with the after chip insertion. The launch pads on the chips are in perfect alignment with the on-wafer transition traces. ... 78

Figure 4.15 Insertion loss and return loss of the chip transition shown in Fig. 4.14 79

Figure 4.16 Schematic of the proposed multi-port S-parameter measurement technique using two-port measurement system 80

Figure 4.17 The circuit model of the proposed S-parameter measurement method (a) N-port device measurement configuration, (b) reference measurement configuration 82

Figure 4.18 (a) Schematic of the optimized 14-slot array (a = 860μm, b = 430μm, l_s = 300μm, w_s = 35μm, g=5μm), (b) Reflection and transmission of the waveguide section with slots 86

Figure 4.19 (a) The optimized 14-slot array schematic, (b) Reflection (S11), transmission (S21), and the coupled power to waveguide probe (S31) versus the position of the waveguide probe with respect to center of the array (x_p,y_p) (h_p=300μm, f=300 GHz) .. 88

Figure 4.20 (a) The matching load based on slot array over micromachined waveguides (optimized dimensions: t_l=11.1 mm, l_{s1}=300 μm, l_{s2}=320 μm, l_{s3}=360 μm, l_{s4}=380 μm, l_{s5}=400 μm, l_{s6}=550 μm, w_{s1}=w_{s2}= w_{s3}= w_{s4}= w_{s5}=30 μm, w_{s6}=500 μm), (b) simulated return loss of the optimized load 90

Figure 4.21 Schematic of the test configuration for coupler characterization 91

Figure 4.22 The measurement setup; the signal coupled from the waveguide through the slot array is measured with the near-field probe. The frequency extenders are mounted on micropositioners to enable manipulation of the probe positions in three dirctions. 92

Figure 4.23 Through ($1/S_{21}$), coupling ($1/S_{31}$), and directivity (S_{31}/S_{41}) of the directional couplers: (a) 10-dB coupler (230-245 GHz), (b) 10-dB coupler (220-325 GHz), (c) 3-dB coupler (220-325 GHz) 93

Figure 4.24 Return loss of the directional couplers 94

Figure 4.25 (a) Repeated measurement of a 10-dB coupler, (b) the phase difference between the coupled signal and thru signal 96

Figure 4.26 Normalized standard deviation of repeated measurements of S21 and S31 . 96

Figure 5.1 The spectral output of the Y-band instrumentation radar system........ 98

Figure 5.2 An image-reject resonant-element FSS (a) Geometry, (b) Transmission response at 45˚ incidence [91] 100

Figure 5.3 One pole bandpass MEFSS (a) Geometry, (b) Transmission response at different incidences [93] 101

Figure 5.4 The proposed single face, membrane supported, MEFSS illuminated by a vertically polarized plane wave. 103

Figure 5.5 Circuit model for one pole bandpass filter with adjacent transmission zero. 104

Figure 5.6 A unit cell of the MEFSS. The optimized dimensions are: D_x = D_y = 470μm, g_c = 60μm, s = 20μm, t_m = 7μm, w_l = 5.7μm, w_c = 5μm, t_p = 10μm. 105

Figure 5.7 Equivalent circuit model of the patch-wire MEFSS for a vertically polarized wave front at a normal incident angle. The optimized parameters are: L = 0.5837 nH, C = 1.0105 fF, C_p = 7.147 fF, L_p = 0.0166 nH, R_L= 6.4479 Ω, Z_0 = 377Ω........ 106

Figure 5.8 Magnetic field distribution around a wire element for two different thicknesses: (a) t_m = 0.5μm, (b) t_m = 7μm 108

Figure 5.9 Simulation results for the patch-wire MEFSS with different element thicknesses. The insertion loss in the passband and the rejection out of the band improves as the element thicknesses increase. 108

Figure 5.10 Simulation results of the patch-wire MEFSS for different angles of incidence 110

Figure 5.11 Numerical simulations for patch-wire MEFSS at normal incidence........... 111

Figure 5.12 Full-wave simulation of the scaled MEFSS for terahertz applications....... 112

Figure 5.13 Schematic diagram of microfabrication of membrane-supported MEFSS . 113

Figure 5.14 The fabricated membrane-supported MEFSS (a) microscopic image, (b) Scanning electron microscope (SEM) image of electroplated gold elements. 114

Figure 5.15 The membrane-supported MEFSS after release.. 115

Figure 5.16 Free-space measurement setup. FSS screen is placed normal to antennas broadside.. 116

Figure 5.17 Measured and simulated transmission response of membrane-supported miniaturized-element FSS.. 117

Figure 6.1 The Y-band instrumentation radar.. 120

Figure 6.2 Block diagram of the Y-band radar front-end 121

Figure 6.3 The measurement setup for indoor backscatter phenomenology study (a) block diagram [100] (b) the setup placed on a portable cart 123

Figure 6.4 EECS building layout and the radar path in the corridors............................ 124

Figure 6.5 Time domain response of a sample backscatter measurement..................... 124

Figure 6.6 2D image created by 180° scan of the hallway (a) raw data (b) after applying peak detection method 125

Figure 6.7 (a) Photo of the scanned view (b) radar position in the hallway................... 126

Figure 6.8 The 2D image created by 180° scan of the scene shown in (a): (b) Vertical polarization (c) Horizontal polarization... 127

Figure 6.9 Ghost images are result of specular reflection of large scatterers from smooth surfaces at oblique angles of incidence.. 128

Figure 6.10 The target location is associated with an element in the global coordinate matrix corresponding to the discretized scanned area 129

Figure 6.11 The complete map of the building is created by integrating the radar images at each step.. 130

Figure 6.12 ρ-θ parameterization of straight line.. 132

Figure 6.13 Sinusoids corresponding to co-linear points (black points) intersect at a unique point in the image plane a) x-y plane, b) Hough transform image plane............ 132

Figure 6.14 The final map after linear feature extraction using Hough transform. Ghost images and fake blockings are still present in this image... 134

Figure 6.15 The final map after ghost image and fake blocking elimination................ 136

Figure 6.16 The backscatter measurements setup. The sample distance to the antenna is 2 meters. 137

Figure 6.17 The 3-inch dual-polarized lens antenna (a) front view (b) schematic 137

Figure 6.18 Antenna pattern (a) E-plane (b) H-plane 138

Figure 6.19 The 240 GHz polarimetric measurement system 139

Figure 6.20 Backscatter response of a tilted cylinder in the time domain 140

Figure 6.21 Backscatter response of a tilted cylinder before and after range gating 141

Figure 6.22 Backscatter response of copper cylinder (a=1.2cm) 142

Figure 6.23 Measured backscattering coefficients of (a) drywall without paint (b) drywall with paint 143

Figure 6.24 Cross section of (a) unpainted drywall and (b) painted drywall 144

Figure 6.25 Measured backscattering coefficient of (a) marble, (b) ceramic, (c) concrete blocks, (d) wood door with paint, (e) tile, (f) 6-mm wire mesh 146

Figure 6.26 Backside view of the measured tile 147

Figure A.1 (a) The GSG probe fed microstrip line model in an actual setup, (b) current launch pad configurations 155

Figure A.2 (a) The backside of the chip is trimmed reducing the distance to the launch pads, (b) RL and IL as a function of the distance of the tips from the edge of the chip (x) 156

Figure A.3 The proposed tapered transition from pads to the microstrip line 156

Figure A.4 The final transition design with optimum via positions 157

Figure B.1 The capacitance network representation of a coupled-line structure 159

Figure B.2 Cross section of the proposed CBCPW coupler (optimized dimensions: h = 45µm, g = 5µm, w = 100µm, s = 97.5µm, $w_b = h_b$ = 50µm) 160

Figure B.3 Electric field distribution in the proposed coupler structure (a) even mode, (b) odd mode 161

Figure B.4 Zigzag edge of the coupled line to create longer propagation path for the odd mode 163

Figure B.5 The micromachined coupler with port connections to CBCPW 164

Figure B.6 Simulated performance of the micromachined coupler 164

Figure B.7 Measurement configurations for full characterization of directional couplers; (a) coupled (b) through (c) isolated 165

Figure B.8 The proposed matched load design 167

Figure B.9 Simulated return loass of the optimized matched load 167

Figure C.1 Unit cell of the MEFSS/polarizer structure (Dx = Dy = 4.5mm, dx = dy = 265mm, w = 254µm, g = 254µm, t = 787µm, wp = 0.2mm, gp = 0.7mm) 168
Figure C.2 Numerical simulations of the patch-loop MEFSS 170
Figure C.3 Full-wave simulation of the combined polarizer and MEFSS for TE and TM polarizations 171
Figure C.4 Fabricated structure (a) patch-loop MEFSS (b) wire-grid polarizer............. 172
Figure C.5 Ka-band free space measurement setup.. 172
Figure C.6 Measured and simulated responses of the MEFSS structure........................ 173

LIST OF TABLES

Table 1.1 Characteristics of indoor navigation and range finding systems 9
Table 1.2 Beam scanning Y-band radar specifications... 13
Table 6.1 Data collection specifications 139
Table B.1 Even- and odd-mode characteristics of the proposed coupler 161
Table B.2 Return loss and impedances of various thin film resistances......................... 166

LIST OF APPENDICES

Appendix A Optimal Launch Pad Design for Microstrip Lines on InP Substrate

Appendix B Micromachined Coupled Line Directional Coupler Fabricated on CBCPW line

Appendix C Ka-Band Bandpass MEFSS and Polarizer

LIST OF ABBREVIATIONS

MMW	Millimeter-wave
Sub-MMW	Submillimeter-wave
THZ	Terahertz
MMIC	Monolithic millimeter-wave integrated circuit
CBCPW	Cavity-backed coplanar waveguide
S-parameters	Scattering parameters
FSS	Frequency selective surface
MEFSS	Miniaturized-element frequency selective surface
GSG	Ground-signal-ground
DRIE	Deep reactive ion etching
RCS	Radar cross section
RL	Return loss
IL	Insertion loss

ABSTARCT

A Micromachined Millimeter-Wave Radar Technology for Indoor Navigation

by

Meysam Moallem

Chair: Kamal Sarabandi

A compact, light-weight, low-power MMW radar system operating at 240 GHz is introduced to enable autonomous navigation of micro robotic platforms in complex environments. The short wavelength at the operating frequency band (1.25mm @ 240 GHz) enables implementation of the radar front-end components on a silicon wafer stack using micromachining techniques.

This work presents the design, fabrication technology, and measurement methodology of components for the micromachined MMW radar and the phenomenology of such radars in indoor environments. Novel passive structures are developed to realize a fully micromachined radar front-end. Low loss cavity-backed CPW (CBCPW) lines (0.12 dB/mm @ 240 GHz), broadband transitions from the CBCPW line to rectangular waveguide (IL<0.9 dB; RL>13 dB; BW: 39%), MMIC chip integration transitions, and waveguide directional couplers are designed to fully integrate active and passive components of the radar. Also a membrane-supported miniaturized-element FSS image-reject filter (IL<0.6 dB in the passband; rejection>25 dB in the stopband) is developed for MMW radar applications. The structures are designed compatible with micromachining

technology and optimized for minimum insertion loss. The designed components are then realized over a two layer stack of silicon wafers. Multi-step structures are realized on one of the wafers and the membrane-supported features are implemented on the other wafer. A novel multistep DRIE technique is utilized to enhance the profile quality of the fabricated structures. Measurement techniques are developed to enable accurate and repeatable characterization of the on-wafer components at MMW and higher frequency bands. A novel waveguide probe S-parameter measurement technique is introduced for non-contact characterization of the multi-port components using a two-port network analyzer.

To examine the utilization of the proposed 240 GHz radar for collision avoidance and building interior mapping applications, the interaction of electromagnetic waves with objects in the indoor environments is investigated. An instrumentation radar is utilized to collect backscatter data from corridors in an indoor setting. The collected data is used to form radar images for obstacle detection. The radar images are co-registered in a global coordinate matrix to form a complete map of the interior layout. Image processing techniques are used to enhance the final layout map.

CHAPTER 1
INTRODUCTION

1.1 Motivation

Micro robotic systems have gained great interest in the past two decades due to advances in microelectronic and MEMS technology (Figure 1.1). These small robots are used for applications such as remote sensing in complex and hazardous environment, ad-hoc sensor networks, and surveillance purposes [1-3].

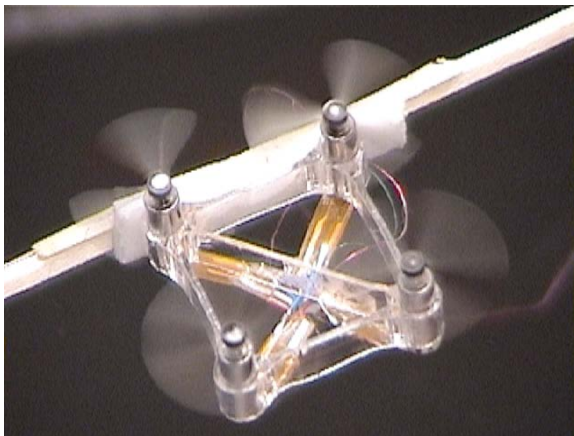

(a)

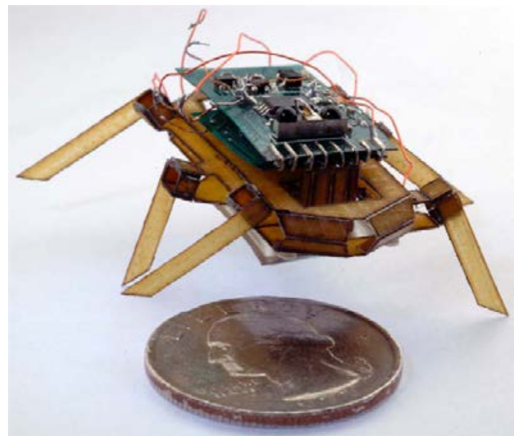

(b)

Figure 1.1 Micro robotic systems (a) a miniature autonomous rotorcraft (Mesicopter) [4], (b) An autonomous 2.4g crawling hexapod robot (RoACH) [5]

In Figure 1.2, an autonomous flyer is used to penetrate into a building, navigate through the complex and cluttered environments to collect and transmit data, and finally exit the building. To enable such application, the mobile platform requires a reliable sensor suite to navigate in urban and indoor environment.

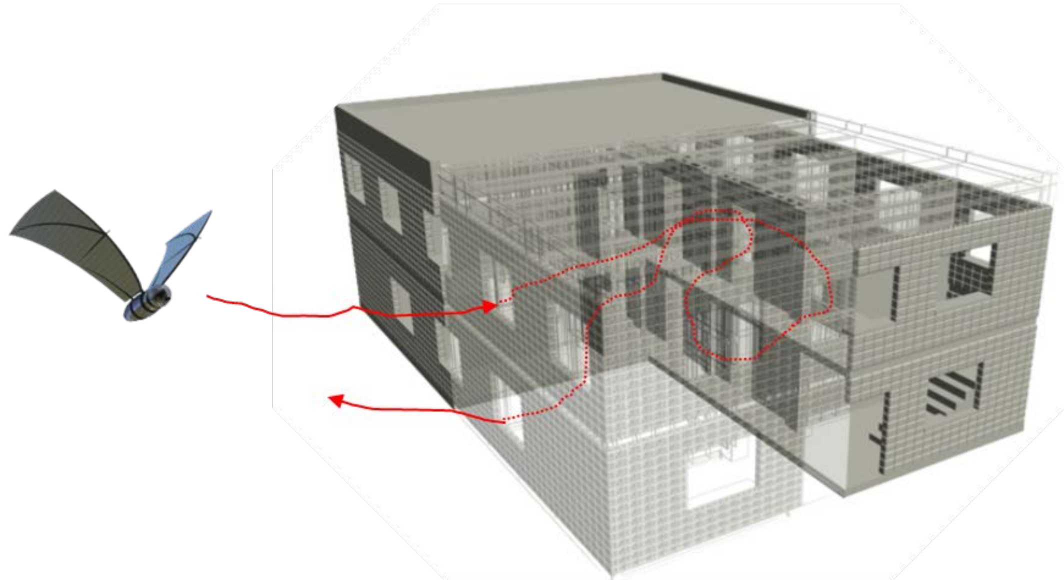

Figure 1.2 Autonoumous navigation in a complex setting

Inertial navigation systems (INS) are among the most popular navigation aids for robotic applications. These systems use motion and rotation sensors (i.e. accelerometers and gyroscopes) to calculate the position of the robot via dead reckoning [6]. With the advent of MEMS technology, micro inertial sensors have been realized and commercialized for a wide variety of applications [7]. However, the dead reckoning technique suffers from integration drift which results in large errors in position due to accumulation of small errors in measurement of acceleration. Global positioning system (GPS) receivers are also among the most common sensors for navigation. However, these receivers cannot operate in indoor and enclosed environment where the GPS satellite signal is not available.

The major drawback with INS and GPS sensors is that they cannot navigate robotic systems where the layout map of the environment is not known. For autonomous navigation in unknown settings, range finding and collision avoidance technologies including optical, ultrasonic and ultra-wide-band (UWB) systems have been used for

robotic applications. The characteristics of these sensors and the state of the art technology for each method are presented in the Section 1.2.

Due to limited space, onboard power, and processing capability the sensors mounted on micro autonomous robots must be low mass, compact size, low power, and run with minimal processing resources. It will be shown while the size and power consumption of the current sensors have been reduced over the years, they are still too bulky and power hungry for micro robotic applications.

The micro robotic platforms are intended to operate in hazardous environment where the atmosphere might be filled with smoke, dust, etc. Optical and camera-based sensors fail to operate in such optically opaque environments. The sensor also needs to detect smooth surfaces and obstacles (walls, doors, etc.) at oblique angles. Ultrasonic and UWB systems have a very narrow detection angle which limits their application in an indoor environment.

For autonomous navigation in a complex urban or indoor environment, an obstacle detection sensor with high angular resolution (narrow beamwidth) is necessary to enable detection of small passages and openings for the moving robot. For example, to detect an opening of 1 foot width from 10 meters distance the angular resolution of the detection device must be 2° or less in the azimuth direction (Figure 1.3). It will be shown that UWB and low MMW (<100GHz) radars require very large antennas to achieve such narrow beamwidth which makes them too bulky for micro robotic platforms.

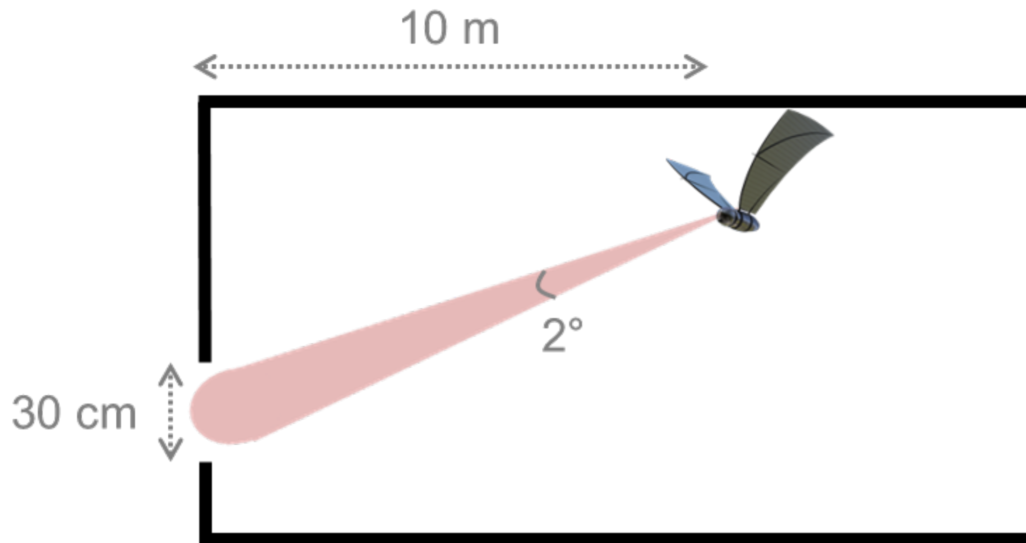

Figure 1.3 A typical scenario in indoor navigation

A compact, light-weight, low-power navigation system with the ability to function in poor atmospheric conditions is needed to enable the autonomous operation of micro robotic systems in a complex environment. We have proposed a micromachined MMW radar that encompasses all these requirements.

1.2 Current Navigation and Collision-Avoidance Sensors

1.2.1 LADAR Systems

Optical systems are among the most popular navigation and mapping systems used for autonomous robots [8-11]. Laser detection and ranging (LADAR) is a remote sensing technology that can measure the distance to a target by illuminating it with laser pulses. The operating wavelength of LADAR systems is mostly in the range of 800-1000 nm. Since the surface roughness of most obstacles and surfaces in the indoor environment is much larger than the wavelength, light reflection is dominated by the diffuse component

which is governed by Lambert's cosine law [12]. This allows for object detection from normal incidence up to near grazing incidence angles. Broad scanning angle and high resolution make these systems suitable for indoor navigation and mapping. However, application of LADAR systems for micro autonomous robots is mainly limited due to their size and power consumption. A typical LADAR system block diagram is shown in Figure 1.4.

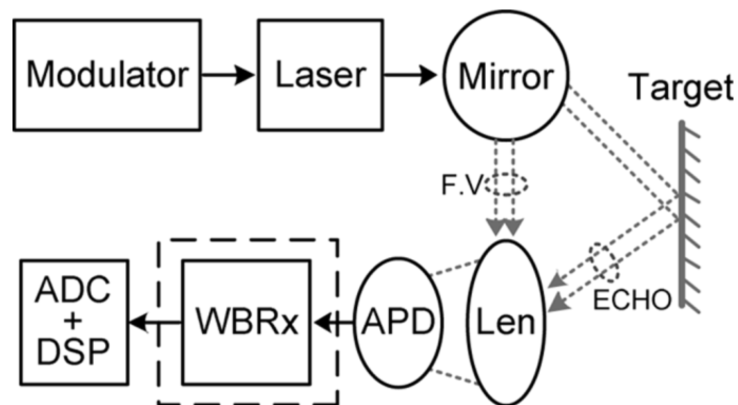

Figure 1.4 A typical LADAR system block diagram [13]

While the recent advances in the CMOS technology have enabled realization of high performance integrated optical receivers, the optical scanning module and the laser transmitter make the overall system bulky and power consuming [13-16]. A state of the art compact MEMS scanning LADAR system is shown in Figure 1.5. The camera box dimensions are 3.5"×6"×11" with a weight 5.8 lb. The power consumption is 30 Watts and the system is passively cooled. [17]

In addition, similar to other optical systems their performance is hampered by smoke and fog. The attenuation of optical wave in heavy fog or smoke can reach 1 dB/meter as shown in Fig. 1.6 which significantly limits the detection range of the optical sensor. Other drawbacks include mechanical scanning and performance degradation in the

presence of ambient infra-red (IR) sources and in highly lit environment in which the receiver saturates and degrades the detection range significantly.

Figure 1.5 Commercial compact LADAR system for robotic applications [18]

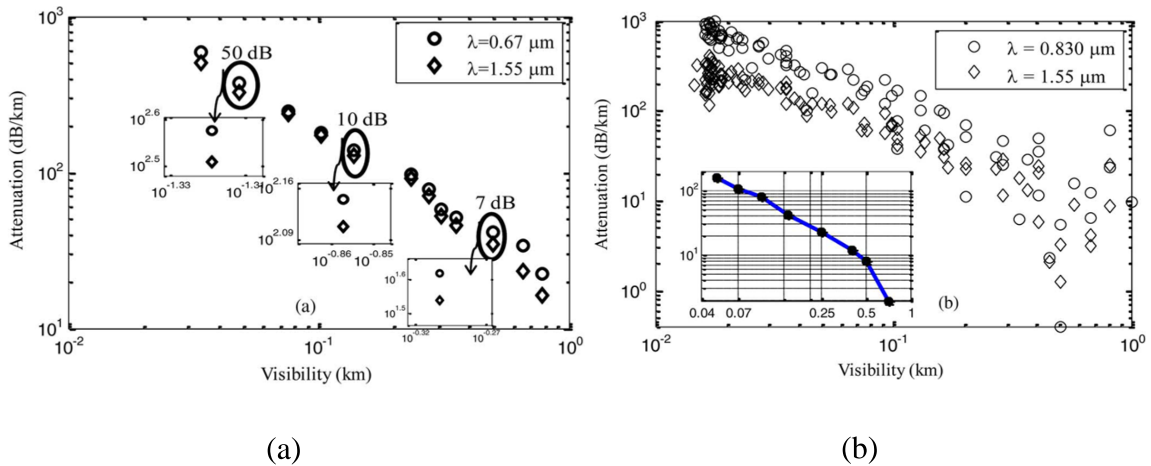

(a) (b)

Figure 1.6 The measured attenuation at optical band (a) fog, (b) smoke [19]

1.2.2 SONAR Systems

Another common method for indoor navigation and mapping is sound navigation and ranging (SONAR) using ultrasonic range sensors [20-22]. Most SONAR sensors operate using the time of flight (TOF) principle [23, 24]. In its most common form, it is a single transducer, which initially operates as a transmitter, transmitting an acoustic wave

into the environment, and then switches its mode to that of a receiver in order to receive the acoustic wave after reflection from an object [25]. There are certain drawbacks associated with these sensors as well. Such sensors have limited range and suffer from transducer's poor efficiency due to impedance mismatch. They also require relatively a large aperture (about 20 cm diameter for 2° beamwidth at 50 KHz), and mechanical scanning. A state of the art commercial imaging SONAR system is shown in Figure 1.7.

Figure 1.7 Commercial ultra-compact imaging SONAR (Power requirement: 12 - 48V DC at 4VA, weight: 324 grams) [26]

In addition, since the wavelength of ultrasonic ranging systems (6.6 mm at 50 KHz) is larger than surface roughness of interior walls, the reflection from most indoor surfaces is specular. Due to specular reflections, only perpendicular angles of incidence give correct estimation of the range from a wall. It is also noted that due to significant difference between the acoustic impedance of air and wall materials acoustic signal cannot penetrate and thus volume scattering cannot contribute to the backscatter.

1.2.3 UWB Systems

Ultra Wide Band (UWB) radar systems at low microwave frequencies (f <10 GHz) have recently been used for mapping in indoor environments [27-29]. However these systems share some of the drawbacks of SONAR systems. Since the wavelength is much larger than the surface roughness of indoor surfaces, the diffuse backscatter from these surfaces is very small. This limits the scan angle of such radars close to normal angle. In addition the antenna aperture needed for such systems to achieve narrow beamwidth is exorbitantly large to be useful for small robotic platforms. Figure 1.8 shows a UWB radar sensor unit. The dimensions of each sensor are 7.75” × 4.875” × 4.75” including antennas [29].

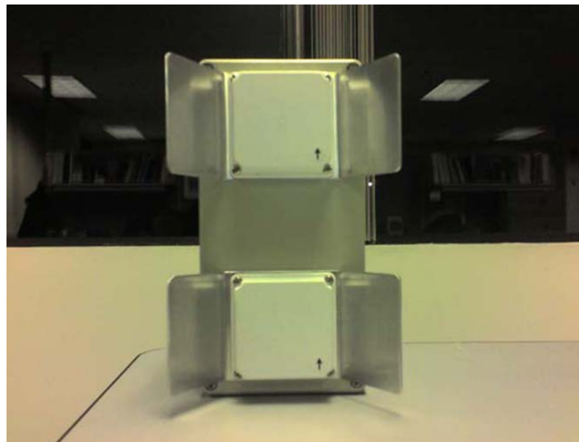

Figure 1.8 UWB radar sensor unit [29]

Table 1.1 summarizes the characteristics of the current indoor navigation systems. To overcome the problems associated with the current trends in indoor navigation of robotic systems, the use of MMW radars for indoor navigation and mapping is proposed. The characteristics of the proposed MMW radar are discussed in the next section.

Table 1.1 Characteristics of indoor navigation and range finding systems

Navigation systems	Size, Weight and Power (SWaP)	Operation in adverse condition	Detection angle
LADAR	89×152×29 mm^3, 2600 grams, 30W [18]	Non-functional in smoke, dust, …	Broad (near grazing)
SONAR	58×68×79 mm^3, 324 grams, 4W [26]	functional	Narrow (near perpendicular)
UWB	200×120×120 mm^3, 1.2W [29]	functional	Narrow (near perpendicular)
proposed MMW radar	**42×32×15 mm^3, 5 grams, 200 mW**	**functional**	**Broad**

1.3 MMW Radar Technology

With the advent of active and passive MMIC technology, there is an increasing interest in developing integrated high millimeter-wave (MMW) and terahertz systems for applications in ultra-fast wireless communication, vital-sign detection, and imaging [30-32]. While fully integrated transceiver modules have been reported in the literature, the integration of the antennas with the rest of the radar front-end remains a challenge. Some of the reported on-chip transceivers utilize external directional large horn or dish antennas which makes the radar to bulky for micro robotic applications (Figure 1.9).

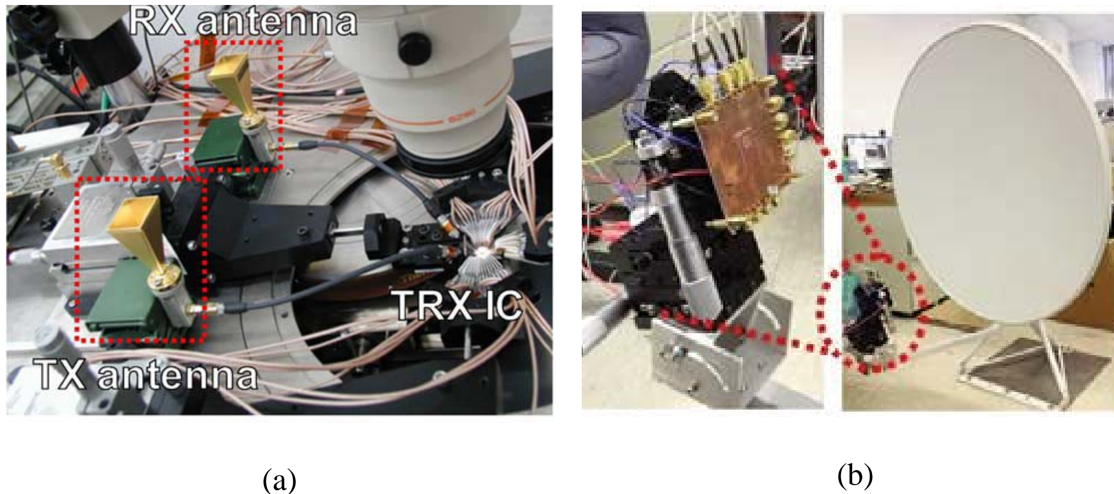

(a) (b)

Figure 1.9 (a) A 77 GHz FMCW CMOS transceiver with horn antennas [33], (b) A 94 GHz CMOS 3-D image radar engine with dish antenna [34]

Fully integrated radar systems have also been reported in the literature [31, 35]. These systems typically have patch antennas implemented on PC boards (Figure 1.10). There are two drawbacks associated with these antennas: 1) they have low efficiency at high MMW and sub-MMW frequencies. Significant substrate loss in the PCB at these high frequencies reduces the efficiency of the antennas, and hence, the overall radar system, 2) for indoor navigation purposes where the intended operation environment includes narrow hallways, the radar antenna is required to have a narrow beamwidth in the azimuth direction to provide enough angular resolution for the radar to detect obstacles the hallway. To achieve a narrow beamwidth a large array of patch antennas is required. This large array increases the overall radar size (>15cm for 2° beamwidth at 60 GHz). The power loss in the corporate feed also further reduces the radar efficiency.

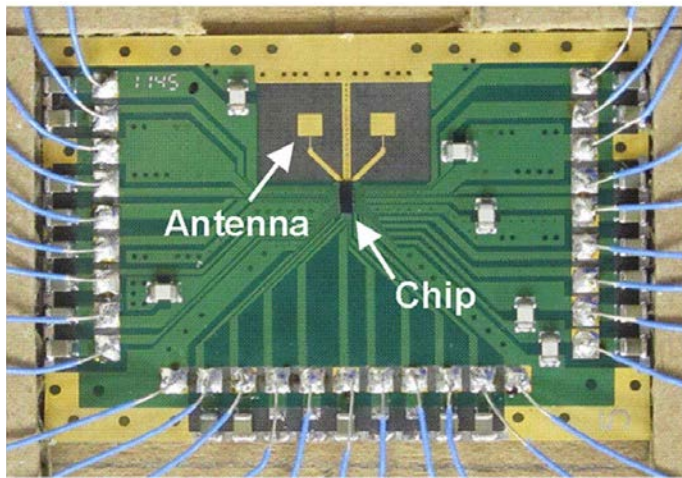

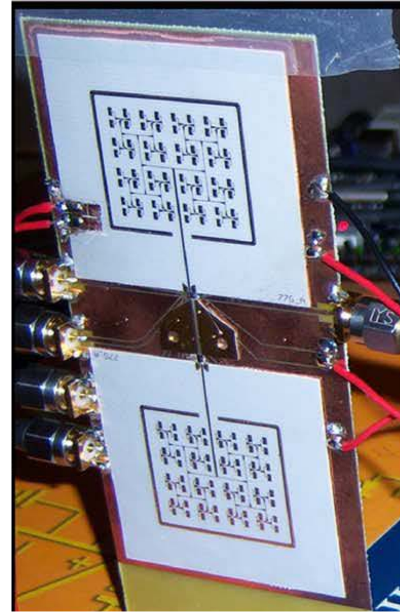

(a)

(b)

Figure 1.10 (a) 60 GHz CMOS Doppler radar with integrated patch antennas (beamwidth> 40°) [31], (b) 77GHz FMCW radar system with patch array antennas (beamwidth = 9°) [35]

1.4 The MMW Micromachined Beam-Stearing Radar

To overcome the difficulties associated with PCB antennas, we proposed a compact and low-power micromachined MMW beam-stearing radar system. The schematic of the proposed radar is shown in Figure 1.11.

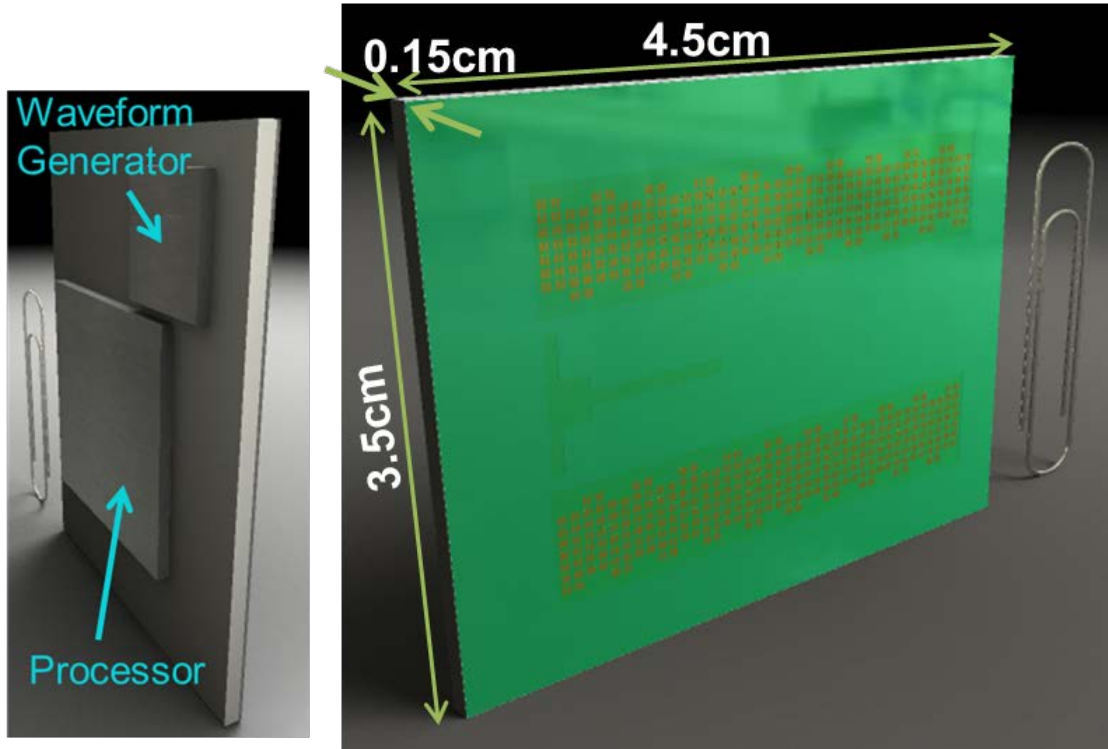

Figure 1.11 Schemetic of the proposed micromachined radar

The radar system is fabricated and assembled using silicon micromachining techniques with an overall mass of 5 grams, a peak power of 200 mW, and operational power of 6.7 mW for a one frame per second update rate, a field of view of ±25° , an angular resolution of 2°, a range resolution of 37.5cm, and an alias-free range of 400m. The transmit and receive antennas are hybrid-coupled patch arrays fed by a slot-waveguide travelling wave structure [36]. The beam steering is accomplished by frequency scanning and the range resolution is obtained from the standard FMCW technique utilizing a chirped signal waveform with step discontinuities. The specifications of the desired beam scanning radar are listed in Table 1.2.

Table 1.2 Beam scanning Y-band radar specifications

Micromachined FMCW Radar	
Power	200 mW
Weight	5 grams
Dimensions	4.2×3.2×0.15 = 2 cm^3
Wavelength	1.2 mm
Peak Tx Power	10 dBm
Rx Sensitivity with 5dB SNR	-135 dBm
Beamwidth	Az: 2° El: 8°
Antenna max directivity	27 dB
Waveform	Stepped FMCW
Operating Frequency	230 GHz-245 GHz
Field of view	±25°
Alias-free range	400 m
Range resolution	37.5 cm

The short wavelength at high MMW frequencies (1.25mm at 240 GHz) enables implementation of antennas and other waveguide-based components on silicon wafer using micromachining techniques. This significantly increases the radar efficiency by eliminating substrate loss associated with conventional PCB structures. On the other hand, the active modules (20 GHz to 240 GHz source chain on the transmitter end and

downconverting module on the receiver end) are implemented on chip using mHEMT technology. The block diagram of the proposed radar is shown in Figure 1.12.

A wide band, low loss, and robust integration method is introduced to integrate the active chips with the micromachined antennas. Micromachined passive components are developed to enable full integration of the radar front-end as shown in Figure 1.13.

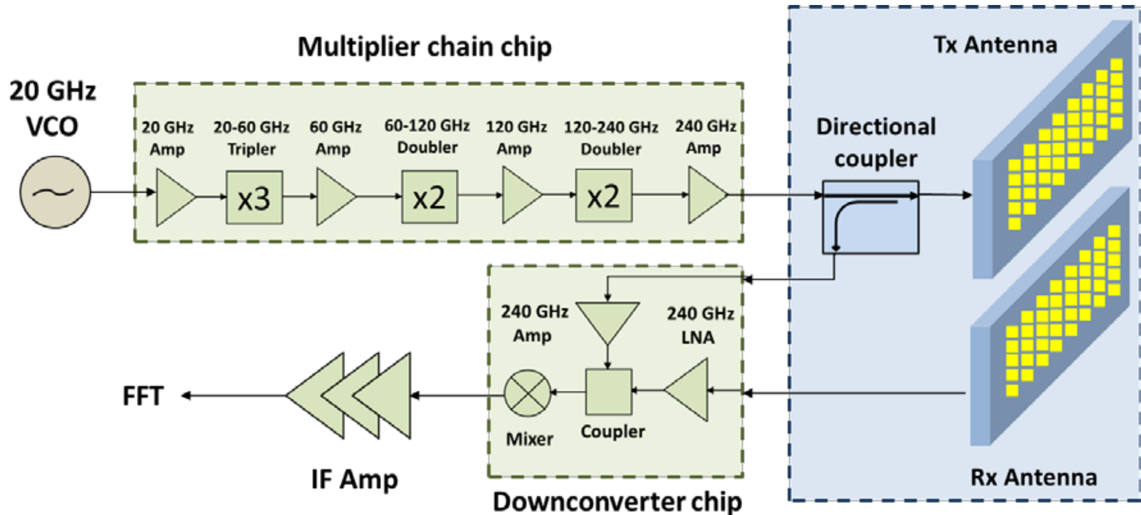

Figure 1.12 Block diagram of the proposed beam scanning 240 GHz navigation radar

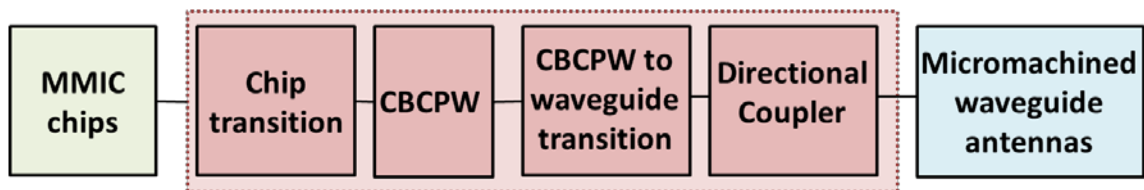

Figure 1.13 Passive components for radar front-end integration

To examine the utilization of proposed 240 GHz radar for collision avoidance and building interior mapping applications, a study of the interaction of electromagnetic wave with objects in the indoor environments is needed.

1.5 MMW Radar Phenomenology in Indoor Environment

In recent years, MMW radars have been widely investigated for applications ranging from automotive collision avoidance [37], to guidance systems for aircraft landing[38, 39], target detection and tracking [40] and clutter measurements [41]. The ability to penetrate poor weather, dust, smoke, cloth and other low loss but optically opaque materials makes these radars suitable for navigation and surveillance [42-44]. The MMW attenuation due to poor atmosphere is shown in Figure 1.14. The radars studied for these applications typically operate at lower MMW frequencies (<100 GHz). However, little investigation has been done for the application of radars operating at higher MMW and sub-MMW. While having the ability to operate in poor weather, these radars have certain advantages over the radars operating at lower MMW bands for indoor navigation and mapping: a) reduction in size and mass of the radar allows developing small ultra-light weight radars for navigation and mapping of micro-autonomous robotic platforms operating in indoor settings, and b) since the typical wall surfaces such as drywalls are smooth at MMW band, interior layout detection at oblique angles of incidence is only possible if enough volume or surface scattering in the backscatter direction can be observed from wall materials at oblique incidence by the radar. Since the size of inhomogeneities within most walls (small air bubbles, micro cracks, etc.) and the wall surface roughness is much smaller than the wavelength the backscatter (similar to Rayleigh scattering) is a very strong function of frequency ($\sim f^4$). This results in much higher backscatter at higher MMW and sub-MMW frequencies compared to the backscatter at lower MMW frequencies.

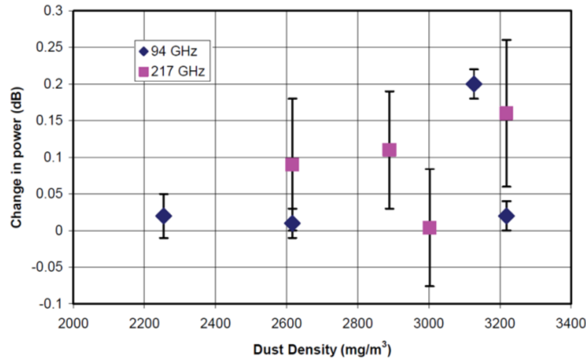

(a)

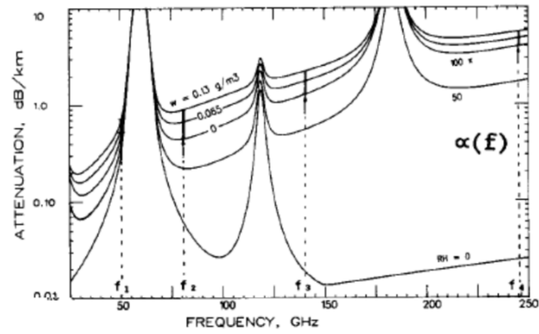

(b)

Figure 1.14 MMW attenuation in poor atmosphere (a) attunation due to dust in 1-m dust tunnel [45], (b) attenuation in moist air [46]

Due to the nature of obstacles and targets in an indoor setting and the issues confronted in navigation and mapping in such environment compared to other applications, a thorough study is required to verify the applicability of these radars to indoor navigation and mapping. The main targets in an indoor environment are relatively smooth surfaces made of drywalls, tiles, wood, brick, concrete, adobe, etc. Many of these surfaces are typically covered with a thin layer of paint (homogeneous dielectric) which makes the surface appear even smoother. The scattering phenomenology of EM waves from such targets has not been addressed before in other applications. In addition, as will be shown, the specular reflection from these smooth surfaces is rather strong causing significant multi-path among parallel and perpendicular walls in an indoor setting. The analogy for the optical band is to perform path-finding and navigation in relatively small pathways with mirror surfaces. To reduce the associated difficulties, the effect of the polarization on the reflection from interior layout is investigated. In addition image processing techniques are developed to eliminate the remaining effects in the final radar map.

1.6 Dissertation Overview

This dissertation presents the design, fabrication and measurement technology of a micromachined MMW radar and the phenomenology of such radars for indoor navigation applications.

In Chapter 2, the design of the integrated micromachined MMW radar front-end is presented. Novel passive components and structures have been designed to enable integration of the front-end using micromachining technology: 1) a cavity-backed CPW line (CBCBW) is designed and optimized for minimum loss with 50Ω characteristic impedance. This line has less than 0.12 dB/mm loss over the entire J-band (220GHz-325GHz). 2) A broadband fully-micromachined transition from rectangular waveguide to CBCPW line is presented. The transition from CBCPW to waveguide is realized in three steps to achieve a broadband response with a topology amenable to silicon micromachining. The first step is a tapered transition from the CBCPW line to a 50Ω reduced-height waveguide. The next two steps utilize a novel in-plane impedance tapering technique to transition from the reduced-height waveguide to the on-wafer regular height waveguide. The full transition has less than 0.9 dB insertion loss and more than 13 dB return loss over the entire J-band (39% bandwidth). 3) A through-wafer chip mounting configuration and transition from on-chip microstrip line to on-wafer CBCPW line is designed to enable active chip integration. 4) Waveguide directional couplers are designed to couple part of the transmit signal to receiver stage. Multiple apertures on the common wall between the adjacent waveguides are designed and optimized to achieve high directivity couplers over a broad frequency range.

In Chapter 3, the microfabrication processes to realize the proposed components and structures are discussed. The designed components are fabricated on two silicon wafers using micromachining technology. The multi-step structures are implemented on one of the wafers using the DRIE process. A new process to create multi-step structures based on glass-in-silicon reflow technique is proposed to improve the loss performance of the fabricated devices compared to the standard multi-mask method. The suspended lines and slots are implemented on the other silicon wafer. These features are patterned on a thin $SiO_2/Si_3N_4/SiO_2$ membrane which is released from the wafer at the final stage. The two wafers are bonded to form the complete structures using a gold-to-goldthemocompression bonding technique. At each process stage, diffrenet methods have been investigated to achieve the optimal sequence of processes.

In Chapter 4, the measurement technology for characterization of the designed structures is presented. Novel measurement techniques are developed to enable accurate and repeatable characterization of multi-port on-wafer components. First, a waveguide probe measurement technique for characterization of two-port components is proposed. This measurement technique is used to characterize the micromachined waveguides, CBCPW line, the waveguide to CBCPW transition and the chip transition. Then, a non-contact on-wafer S-parameter measurement technique for characterization of multi-port devices at MMW and higher frequencies is presented. The proposed method enables S-parameters measurement of multi-port micromachined devices using a two-port measurement setup. In this method, a small fraction of the signal at each waveguide port is weakly coupled to free space using a small array of reflection canceling slots which is then measured by an open-ended waveguide probe. The S-parameters of the device-under-

test (DUT) are calculated from the measured signals obtained from each port and from that of a reference match waveguide. A broadband waveguide slot array antenna with high return loss is designed as a matched load to terminate all ports of the device except the input port.

Chapter 5 presents the development of a spatial image-reject filter for MMW radar applications. A single-face, membrane-supported, miniaturized-element frequency selective surface (MEFSS) is designed for image rejection of a MMW upconvertor mixer. In this design, a new miniaturized-element patch-wire MEFSS configuration is proposed to select the upper-side band (USB) response of a wave radiated from an upconvertor. The proposed MEFSS produces a single pole and an adjacent transmission zero to suppress the lower sideband. It is shown that the frequency response of this MEFSS can be predicted by an equivalent circuit model and that the location of pole and zero can be tuned independently with physical parameters. MEFSS elements are supported and protected by a 10μm thick low-loss polymer membrane which allows flexible handling and minimizes substrate losses. The thickness of the metallic traces is increased to reduce the conductor loss. A salient feature of this design is the low sensitivity of its frequency response to the angle of incidence and the absence of a harmonic response. This feature allows placement of the spatial filter in close proximity to radiating elements with spherical wavefronts. The membrane-supported MEFSS is fabricated using a microfabrication method with tolerances that allow such filter implementations up to terahertz frequencies. Performance of the fabricated device is experimentally verified using a free-space measurement setup.

In Chapter 6, the application of MMW imaging radars for collision avoidance and navigation of autonomous platforms in indoor environments is investigated. The

polarimetric backscattering phenomenology of walls and doorways are studied to aid the design of such radar systems. Polarimetric backscatter measurements of different wall covers, such as dry-wall, concrete blocks, wood, etc., as a function of incidence angle are carried out using a network analyzer operating at J-band. An instrumentation radar is setup to collect backscatter data from corridors in an indoor setting. At each radar position, radar range profiles for both vertical and horizontal polarizations as a function of angle are used to form polar images for obstacle detection. It is shown that horizontally polarized incident wave can generate higher backscatter level and less reflection from smooth walls at steep angles of incidence and thus is the preferred polarization for this application. The polar images at each location are then co-registered in a global coordinate matrix to form a complete map of the interior layout. Feature extraction and image processing methods are then applied to remove multipath and enhance the radar map of building interiors.

This dissertation concludes with a summary of its contributions and the future directions for this research in Chapter 7.

CHAPTER 2
MICROMACHINED RADAR INTEGRATION

All the passive and active components of the radar front-end must be implemented or integrated on a single substrate to fully integrate the MMW micromachined radar. The proposed radar front-end monolithic design is shown in Figure 2.1. Different components and transitions are needed to enable embedding active components and fully integrate the radar front-end. An on-wafer planar transmission line design is required to facilitate transition from microstrip-based active chips to on-wafer components. A chip mounting configuration and transition design to the on-wafer planar transmission line is required to integrate the chips. A transition design from the on-wafer planar transmission line to on-wafer waveguides is essential to complete the integration chain. Finally, a directional coupler is required to couple part of the transmitted signal to the dowconvertor module. The connections between these components in the radar front-end are shown in the block diagram in Figure 2.2.

In this chapter, the design of passive components and structures for radar integration is presented. The design challenges at higher MMW and terahertz bands are discussed in Section 2.1. In Section 2.2, design of a novel low loss, non-dispersive, membrane-supported planar transmission line optimized for high frequency applications is presented. In Section 2.3, design of a broadband transition from waveguide to the planar transmission line designed in Section 2.2 using a novel in-plane impedance trapeing technique is presented. In Section 2.4, design of a through-wafer chip mounting configuration and the required transition from on-chip microstrip line to the on-wafer

tranmssion line is presented. In Section 2.5, design of micromachined waveguide directional couplers for radar integration is presented.

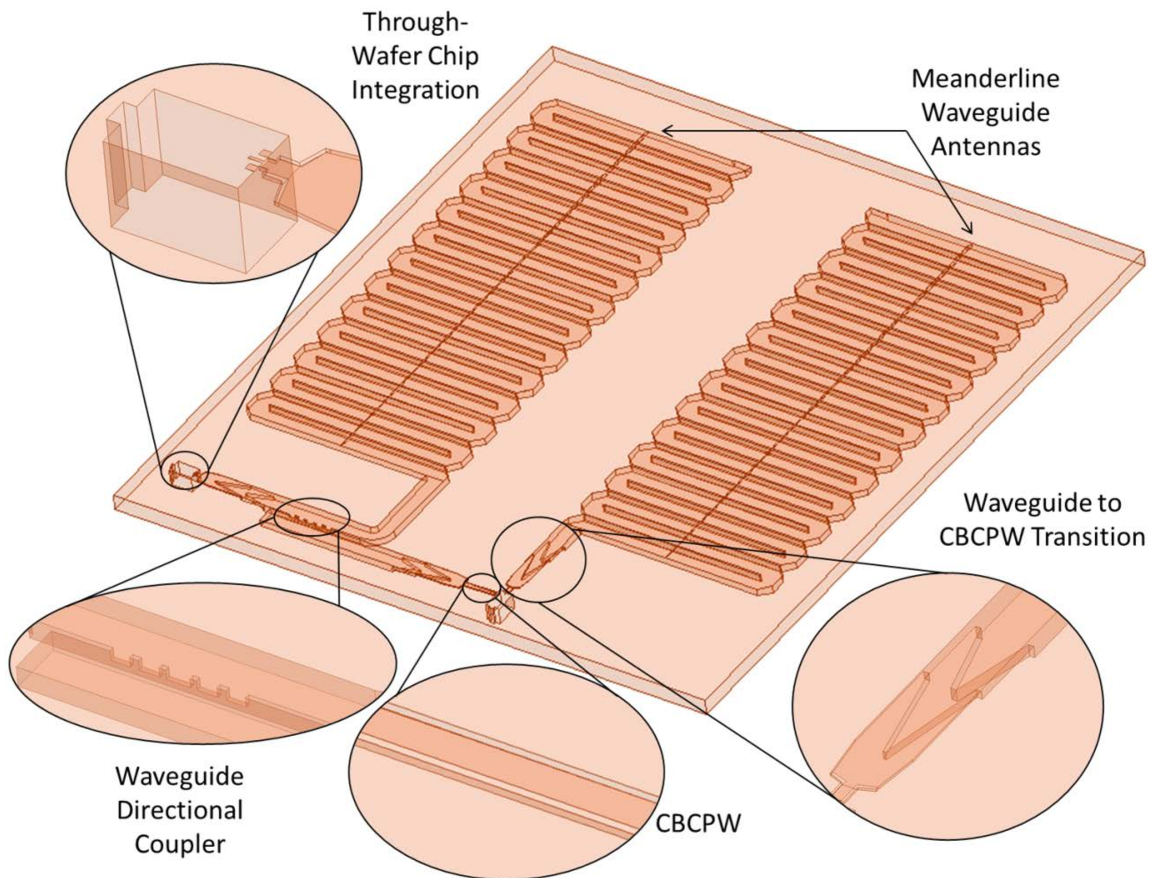

Figure 2.1 The proposed radar front-end micromachined structure

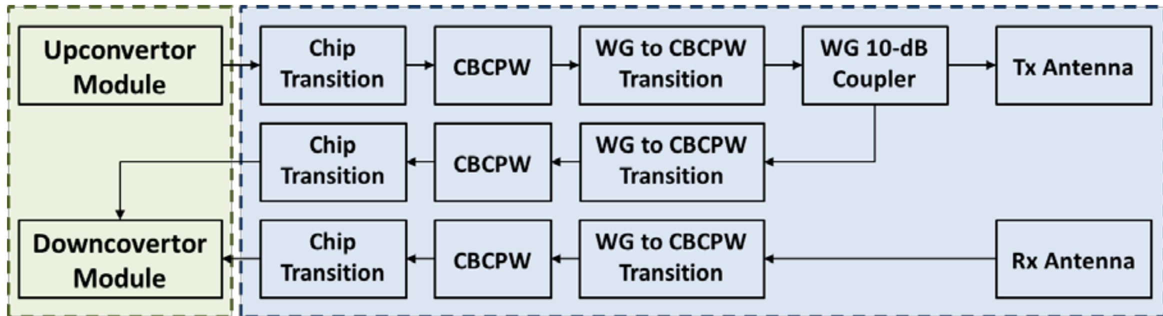

Figure 2.2 The proposed radar front-end block diagram

1.7 MMW/THZ Design Challenges

Designing passive components and structures is subject to certain challenges as the frequency of operation increases to the high MMW and terahertz region. Standard machining processes are utilized to fabricate passive components at microwave and low MMW bands. To maintain the same specifications, the dimensions of structures are scaled with the wavelength. As the dimensions shrink below certain level, standard machining techniques and assembelies are not suitable due to: 1) low fabrication tolerance and, 2) difficulties and high cost in assembly. Micromachining technology offers low cost, high-tolerance, fabrication methods suitable for high frequency applications. However, in order to fabricate components using the micromachining technology, the designed structures must satisfy the constraints associated with this fabrication method. Designs with complex three-dimensional structures, suspended parts, and arbitrary tapering in depth are not compatible with micromachining techniques. On the other hand, as will be described in Chapter 3, lithoghraphy and DRIE processes allow fabrication of structures with arbitrary shapes in the horizontal plane (xy-plane) and discrete steps in height (z-axis). In addition,

all these components and structures must have a compatible design which can be fabricated with a single chain of microfabrication processes.

Another challenge in designing components for high frequency applications is the power loss. Substrate loss and conductor loss limit the performance and efficiency of the components at these high frequencies. Due to limited on-board power, the proposed designs should be optimized to minimize the power loss associated with these sources of loss.

1.8 Cavity-Backed CPW Lines

Coplanar waveguides (CPW) are the most widely used planar transmission line in MMIC applications due to their simplicity of fabrication and integration of components in series or shunt. However, there are some inherent drawbacks with the conventional CPW design. These lines support quasi-TEM wave propagation which makes them dispersive and limits their performance for wideband applications. They can also support substrate higher order modes on relatively thick substrates. However, the most important factor that limits the performance of planar transmission lines in general and CPW lines in particular at sub-MMW and terahertz frequencies is the high insertion loss. Dielectric loss and ohmic loss are the two sources of loss in planar transmission lines. Different techniques have been used in the past to reduce the source of losses in CPW lines. Low-loss dielectric material such as GaAs and quartz have been used to decrease the loss associated with the substrate [47]. Thin polyamide films on silicon have also been used to decrease the substrate loss [48]. Modified CPW structures have also been reported adopting micromachining techniques to eliminate the substrate. V-grooved finite ground coplanar lines and

microshield lines have shown much lower losses compared to conventional designs [49]. Other membrane-supported lines have also been reported in which substrate under the line is removed, reducing the dielectric loss [50, 51]. In order to maintain certain characteristic impedance for these lines, the gap size between the line and the ground must be significantly reduced to compensate for the removal of the substrate in these substrate-less lines. Reduction in the gap size cause two problems: 1) the gap realization becomes difficult and sensitive to microfabrication errors; 2) the field intensity at the gap drastically increases which results in significant increase in ohmic loss and limits the maximum power handling on the line. Hence, low impedance (50Ω) designs are usually not considered for substrate-less membrane-supported designs reported in the literature [49-53]. However, since active circuit modules and MMIC components are mainly designed based on 50Ω impedance, a transmission line with 50Ω characteristic impedance is desirable to integrate these components without mismatch problems.

The design of a 50Ω, dispersion-less, planar transmission line optimized for minimum insertion loss while maintaining single TEM mode propagation for sub-MMW and terahertz applications is first presented here. The proposed CBCPW line is shown in Figure 2.3 [54]. The center conductor is suspended over an air-filled metallic trench with a thin dielectric membrane in this structure. Removal of dielectric substrate from the signal path eliminates the dielectric loss. It also allows for pure TEM mode propagation eliminating signal dispersion [55].

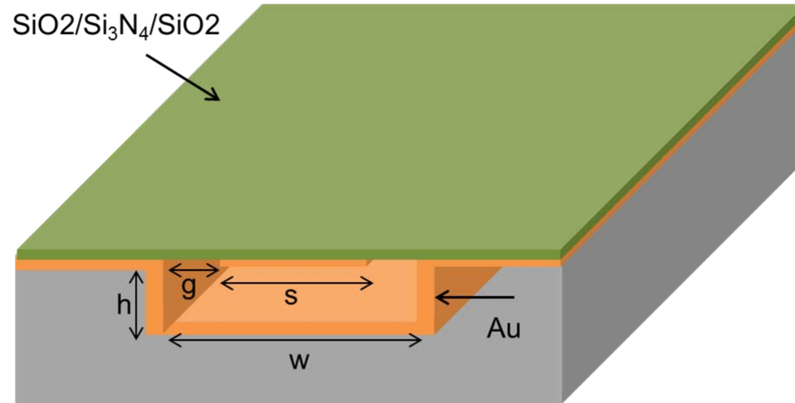

Figure 2.3 The proposed cavity-backed CPW line; the optimized dimensions are: s = 210µm, g = 45µm, h = 46µm, w = 300µm.

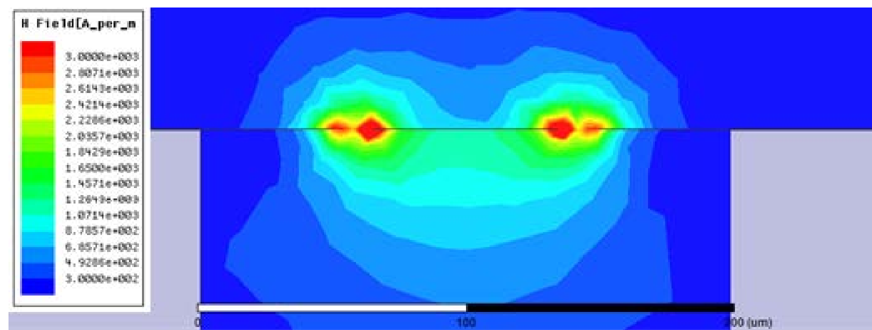

(a)

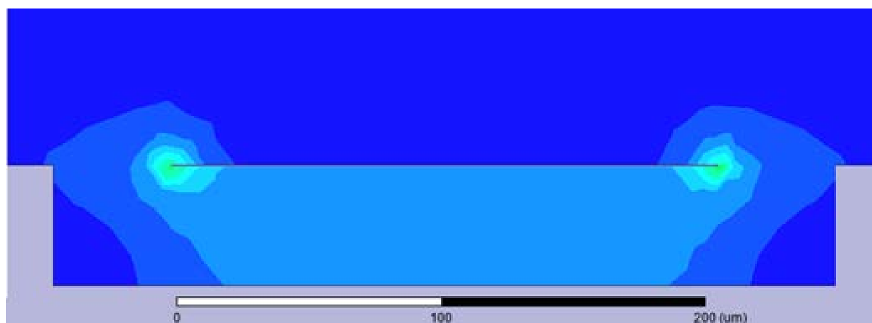

(b)

Figure 2.4 Magnetic field distribution in (a) conventional 50 Ω CPW line on silicon substrate (b) cavity-backed CPW line. The color scale is the same for both figures.

1.8.1 Design Characteristics

The metallic cavity ground under the center conductor offers a number of key characteristics to this line which makes it unique for sub-MMW and terahertz applications:

1) The ground on the bottom and sidewalls of the cavity result in a more uniform field and current distribution on both the center and the ground conductors, as shown in Figure 2.4. This reduces the ohmic loss which is dominated by the currents concentrated on the edges of the center conductor and side ground strips;
2) The presence of the side ground strips together with the lower ground trench creates a field distribution over the line cross section which is a hybrid of the conventional CPW and microstrip modes. This makes the transmission line versatile with benefits of both modes. The CPW mode allows for ease of integration of planar MMIC devices which is the main purpose of this design. On the other hand, the microstrip mode allows the design of the broadband transition from this line to the rectangular waveguides, as will be shown in the Section 2.3.
3) The cavity confines the field to the metallic box eliminating substrate modes and any higher order modes which might be excited at the discontinuities.
4) The added large capacitance between the cavity and the center conductor enables an increase in the gap size between the center conductor and the side grounds while maintaining a 50Ω characteristic impedance which eliminates the aforementioned problems with a small gap size.
5) The lower trench also ensures excitation of the proper mode of operation at the junctions and eliminates the need for the wire bridges commonly used in traditional CPW lines.

1.8.2 Design Optimization

1.8.2.1 Conductor Loss in CBCPW

From the theory of general ideal two-conductor transmission lines, we know that for TEM wave Maxwell's equations reduce to Laplace's equation. Hence, the electric and magnetic fields are decoupled and it suffices to solve for electrostatic potential in the two-dimensional transverse plane to find the transverse electric and magnetic fields on the line.

For non-ideal transmission lines, where the conductors have finite conductivity, attenuation of the line is calculated using perturbation method. It can be shown that the effect of finite conductivity in good conductors can may be accounted for by introducing the surface impedance Z_s where

$$Z_s = \frac{1+j}{\sigma\delta_s} = R_s + jX_s \tag{2.1}$$

where $\delta_s = \left(\frac{2}{\omega\mu\sigma}\right)^{1/2}$ is the skin depth.

If the field distribution around the line and the current flowing along the line are assumed to be the same as in the ideal case, then the power loss in the conductor per unit length is

$$P_L = \frac{1}{2} R_s \oint_{S_1+S_2} |J_s|^2 dl \tag{2.2}$$

where S_1 and S_2 are the cross section of the line and the ground (the cavity and the side grounds) respectively.

The attenuation constant can be found from the current distribution (J_s) over the line:

$$\alpha = \frac{P_L}{2P} = \frac{\frac{1}{2} R_s \oint_{S_1+S_2} |J_s|^2 dl}{Z_c I_0^2} = \frac{R_s}{2Z_c} \frac{\oint_{S_1+S_2} |J_s|^2 dl}{\left(\oint_{S_2} |J_s| dl\right)^2} \quad (2.3)$$

where Z_c is the characteristic impedance of the line.

From the above equation, it can be shown that the attenuation constant is minimized if the current distribution is uniform on the conductor surface. The loss performance of the transmission line, hence, can be optimized over the geometric parameters of the line.

1.8.2.2 Design Optimization using MOM

MOM techniques essentially solve integral equations where the unknown is the integrand [56]. Here we are interested in the charge distribution on the line $\rho(x, y)$ from the integral form of Poisson's equation:

$$\phi(x, y) = \frac{1}{4\pi\epsilon} \iiint \frac{\rho(x, y)}{r} dv \quad (2.4)$$

In order to determine the potential distribution in the two-dimensional plane, we represent the per-unit-length charge distribution over i-th conductor as a linear combination of N_i basis functions:

$$\rho_i = \sum_{k=1}^{N_i} \alpha_{ik} \rho_{ik} \quad (2.5)$$

The ρ_{ik} basis functions will be prescribed and the unknown coefficients α_{ik} are to be determined to satisfy the boundary condition that the potential over the i-th conductor is ϕ_i. The potential due to this representation will be a linear combination of the charge expansion functions. It can be shown that using the point matching method, the integral equation in (2.4) reduces to the following matrix equation:

$$\Phi = DA \tag{2.6}$$

where Φ is the vector of potentials and A is the vector of expansion coefficients of the charge distribution. If D is known, (2.6) can be solved for A to find the charge distribution on the conductors. Knowing the charge distribution $\rho(x, y)$, all the characteristics of the line can be calculated.

Hence, we have to find the elements of matrix D, d_{ij}, which denote the potential produced at the center of i-th subsection due to j-th charge filament. After a simple integration, it can be shown for a filament lying on x axis:

$$D_{ij} = -\frac{1}{4\pi\epsilon}\left[\left(x_p + \frac{w}{2}\right)\ln\left(\left(x_p + \frac{w}{2}\right)^2 + y_p^2\right) - \left(x_p - \frac{w}{2}\right)\ln\left(\left(x_p - \frac{w}{2}\right)^2 + y_p^2\right) - 2w + 2y_p\left(\tan^{-1}\left(\frac{x_p + \frac{w}{2}}{y_p}\right) - \tan^{-1}\left(\frac{x_p + \frac{w}{2}}{y_p}\right)\right)\right] \tag{2.7}$$

$$D_{ii} = \frac{1}{2\pi\epsilon}\left(1 - ln\left(\frac{w}{2}\right)\right) \tag{2.8}$$

where $x_p = x_i - x_j$, $y_p = y_i - y_j$.

The 2D MOM code is developed and used to optimize the dimensions of the CBCPW line structure, namely the line width (s), gap size (g) and cavity height (h), to minimize the attenuation subject to Z_c = 50Ω. The width of the cavity (w) is limited to ensure suppression

of higher order modes. The optimized dimensions are provided in the caption of Figure 2.3.

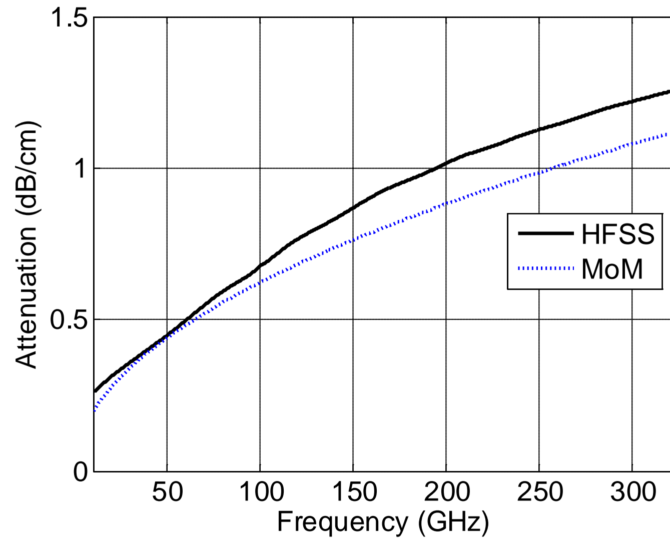

Figure 2.5 Attenuation rate of the optimized CBCPW line using the MOM and HFSS simulations

The performance of the optimized structure was verified using a full-wave simulation (HFSS). The insertion loss of the optimized structure as a function of frequency is shown in Figure 2.5. The phase velocity and characteristic impedance of the optimized structure over frequency is shown in Figure 2.6. It is shown that these parameters change by less than %1 over frequency. This indicates that the line only supports the TEM mode and is indeed dispersionless.

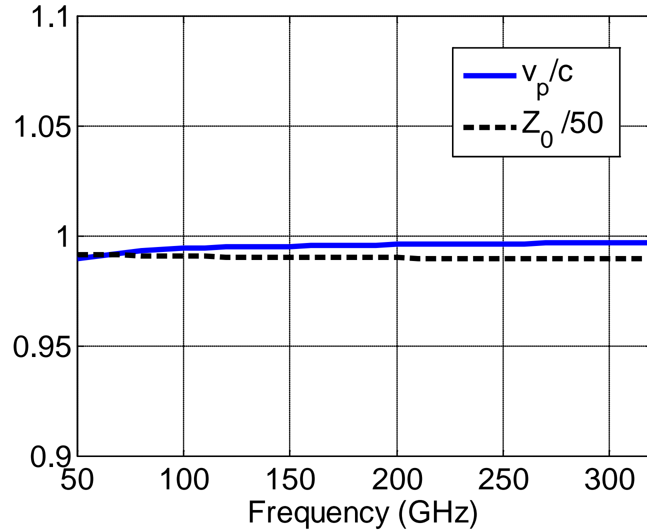

Figure 2.6 Normalized phase velocity and characteristic impedance of the optimized line

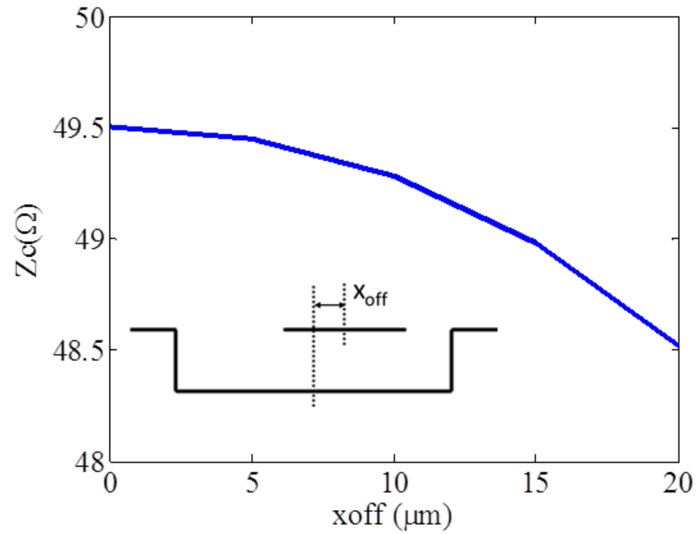

Figure 2.7 Sensitivity of characteristic impedance of CBCPW line with respect to misalignement

The sensitivity analysis of the optimized design with respect to fabrication tolrances is also performed. The sensitivity of the characteristic impedance of CBCPW to misalignment in the horizontal direction is shown in Figure 2.7. As can be seen the change in Z_c is less than 4% for 20um of misalignment.

1.9 Impedance-Taper Waveguide to CBCPW Transition

The radar antennas have been designed and implemented based on micromachined waveguides. On the other hand, active MMIC modules are implemented on planar transmission lines. Hence, a reliable transition from on-wafer waveguides to planar transmission lines is essential to realize fully integrated systems.

A number of transition approaches from planar transmission lines to rectangular waveguide using microfabrication technology for W-band and higher frequencies have been reported in the literature [57-59]. All these transitions have complex 3D geometries which require assembly of various parts. Considering the dimensions in sub-MMW and terahertz region, implementation of such transitions with acceptable accuracy becomes very difficult. Hence, fully micromachined transitions which do not require assembly of parts are preferred for these high frequency applications. A 2.5D fully micromachined resonant-based transition is proposed in [60]. In this design, the transition is realized using two resonant structures: a shorted section of transmission line with a pin inside the waveguide and an E-plane step discontinuity. However, due to the resonant nature of the transition, the fractional bandwidth is limited to 17%. In addition, the performance of the transition is sensitive to good contact with the shorting pin and the waveguide step height which are subject to micromachining tolerances.

Microstrip to rectangular waveguide transitions using impedance tapering technique have been reported in the literature [61-63]. In these structures, a multistep ridged-waveguide impedance taper is typically used to convert the quasi-TEM mode on the microstrip line to the TE_{01} mode in the rectangular waveguide. However, the particular geometry of these designs where the ridged section extends over the planar transmission

line (i.e. microstrip) cannot be easily fabricated with micromachining where both the waveguide ceiling and the planar transmission line are at same level (wafer's top surface). Hence, for high frequency applications, a novel impedance taper transition is proposed which is compatible with silicon micromachining.

Here the configuration and the design procedure for developing a full-band transition from CBCPW line to rectangular waveguide are presented. It should be emphasized that the transition topology is chosen in such way that can be easily fabricated using silicon micromachining. To achieve a broadband response, the transition is realized in three steps. The first step is a tapered transition from CBCPW line to a reduced-height waveguide with the same impedance. The second and third steps are novel in-plane wedge impedance tapers from the reduced-height waveguide to the final waveguide height.

1.9.1 Characteristic Impedance in Waveguides

As will be shown, the design of the proposed transition is based on matching the characteristic impedance (Z_0) of the transmission lines at each step. Therefore, the characteristic impedances of these transmission lines must be defined first. For TEM transmission lines (e.g. CBCPW line), Z_0 is defined by

$$Z_0 = \frac{V^+}{I^+} \tag{2.9}$$

where V^+ is the voltage between the two conductors and I^+ is the conduction current in the propagation direction. This definition uniquely defines the Z_0 in a TEM tranmssion line since the voltage between the conductors ($V^+ = -\int E.dl$) is independent of the integration path. However, in rectangular waveguides V^+ can not be uniquely defined and is a function of integration path.

Other expressions have been used to define the chracateristic impedance in waveguides based on power flow:

1) PI definition:
$$Z_{PI} = \frac{P}{I^{+2}} \tag{2.10}$$

1) PV definition:
$$Z_{PV} = \frac{V^{+2}}{P} \tag{2.11}$$

where P is the power flow in the direction of propagation. In this application, the PI definition is used since it gives the best agreement between transmission line theory and full-wave analysis.

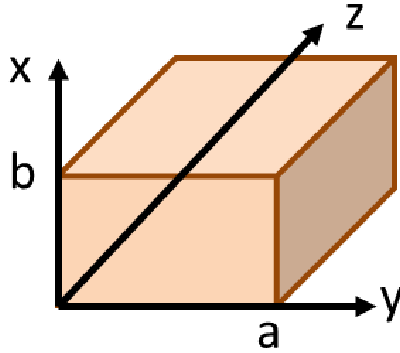

Figure 2.8 The rectangular waveguide

For the TE_{01} mode in the waveguide shown in Figure 2.8, we have:

$$E_x = E_0 \sin\frac{\pi}{a} x \exp -i\beta z \tag{2.12}$$

$$H_y = \frac{\beta}{\omega\mu_0} E_0 \sin\frac{\pi}{a} y \exp -i\beta z \tag{2.13}$$

where $\beta = \frac{2\pi}{\lambda}\sqrt{1-\left(\frac{\lambda}{2a}\right)^2}$.

Hence,

$$P = \iint_S \vec{E} \times \overrightarrow{H^*}.\overrightarrow{dS} = \int_0^a \int_0^b E_x H_y^* dxdy = \frac{\beta}{\omega\mu_0}\frac{ab}{2}|E_0|^2 \tag{2.14}$$

$$|I^+| = \int_0^a |H_y| dy = \frac{\beta}{\omega\mu_0}\frac{2a}{\pi}|E_0| \tag{2.15}$$

and

$$Z_{PI} = \frac{\omega\mu_0}{\beta}\frac{\pi^2}{8}\frac{b}{a} \tag{2.16}$$

It can be noted that with this definition the characteristic impedance is propotional to the height of the waveguide (*b*).

1.9.2 CBCPW to Reduced-Height Waveguide Transition

The first step of the complete transition is a transition from the CBCPW line to a rectangular waveguide with the same height as the cavity (trench) height is proposed (see Figure 2.8 (a)). The TEM mode on the CBCPW line is converted to the TE_{01} mode in the reduced height waveguide in this transition. This transition is enabled due to the fact that the electric field distribution in the CBCPW cavity resembles that of the TE_{01} mode in waveguide. In addition, the width of the reduced height waveguide is tapered to achieve an impedance match with the CBCPW line. The transition dimensions are optimized for minimum insertion loss and maximum return loss. Full-wave analysis of the transition shows more than 15 dB return loss and less than 0.7 dB insertion loss over the entire band (see Figure 2.9 (b)).

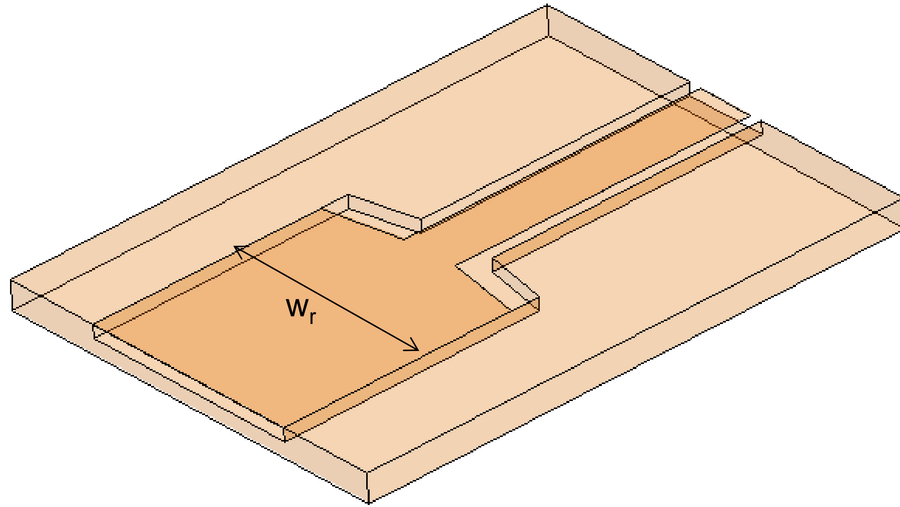

(a)

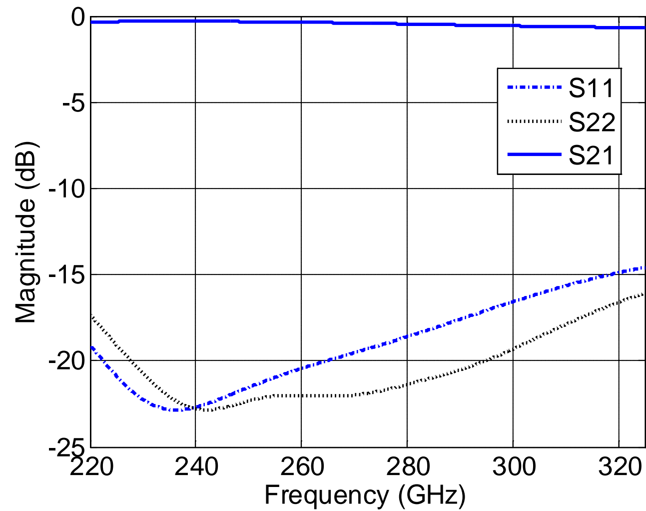

(b)

Figure 2.9 CBCPW to reduced-height waveguide transition: (a) schematic (b) full-wave analysis results. Optimized waveguide width is w_r = 800µm.

1.9.3 In-Plane Impedance Taper Transitions

To get to the standard waveguide height (WR-3), stepped transitions with an in-plane impedance taper is used. The standard approach to change the waveguide height is to

gradually taper the waveguide height, but this cannot be easily implemented. The proposed stepped and in-plane transition requires only two height transitions to taper the impedance of the reduced-height waveguide (50 Ω) to the impedance of the WR3 waveguide (340 Ω). Considering that a limited number of steps (preferably less than 4 steps) can be realized using multi-step micromachining technique (see Chapter 3), the height of the waveguide cannot be tapered since the step discontinuities in the height of the waveguide (and the impedance) do not allow a wideband transition between the two waveguides. On the other hand the lithography process allows fabrication of in-plane features with fine features. Utilizing this characteristic, an in-plane wedge transition, as shown in Figure 2.10, is proposed to create the desired impedance taper.

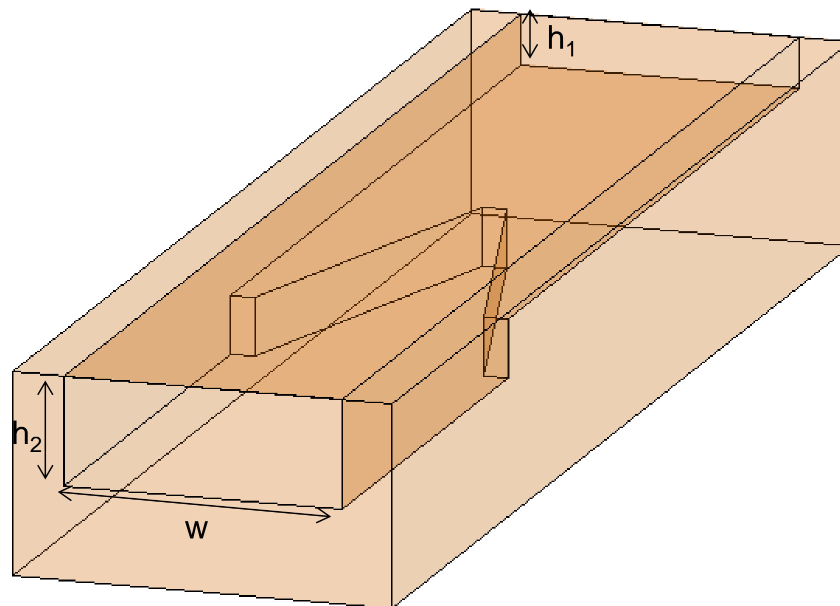

Figure 2.10 Schematic of the in-plane wedge impedance taper

In this transition, the step heights between the waveguides (h_1, h_2) are tapered along the width of the waveguide (w). The cross sectional view of the wedge transition is shown in Figure 2.11 (a). Impedance analysis of this structure shows that the characteristic

impedance (Z_c) smoothly increases as w_t increases (Figure 2.11 (b)). To maximize the transition bandwidth, this technique must be used in at least two steps: 1) from reduced-height waveguide (h_1=46µm) to h_2=200µm, 2) from h_1=200µm to h_2=430µm.

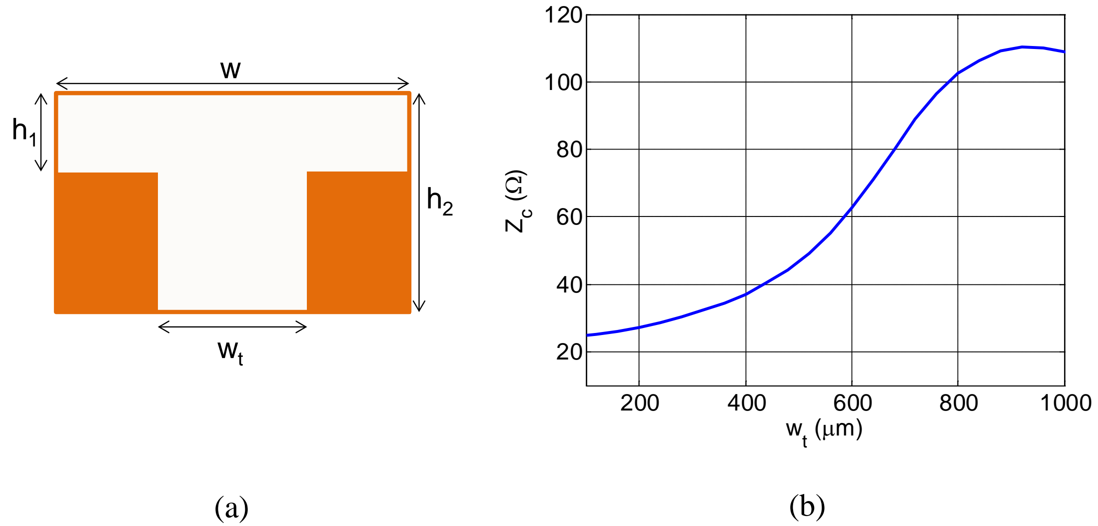

(a) (b)

Figure 2.11 (a) Cross-sectionel view of the in-plane wedge impedance taper, (b) characteristic impedance versus width of the deep waveguide (w_t) (h_1 =46µm, h_2 =200µm)

The complete 3-step transition is shown in Figure 2.12 (a). The length of the two wedge transitions are optimized for maximum return loss over the band. In addition a width of the reduced-height waveguide is tapered to the final waveguide width in the combined transition. Full-wave analysis of the transition shows less than 0.9 dB insertion loss and more than 13 dB return loss over the entire J-band (see Figure 2.12 (b)). The return loss of the transition can be improved by increasing the taper length (t_1 and t_2) or adding more in-plane step transitions.

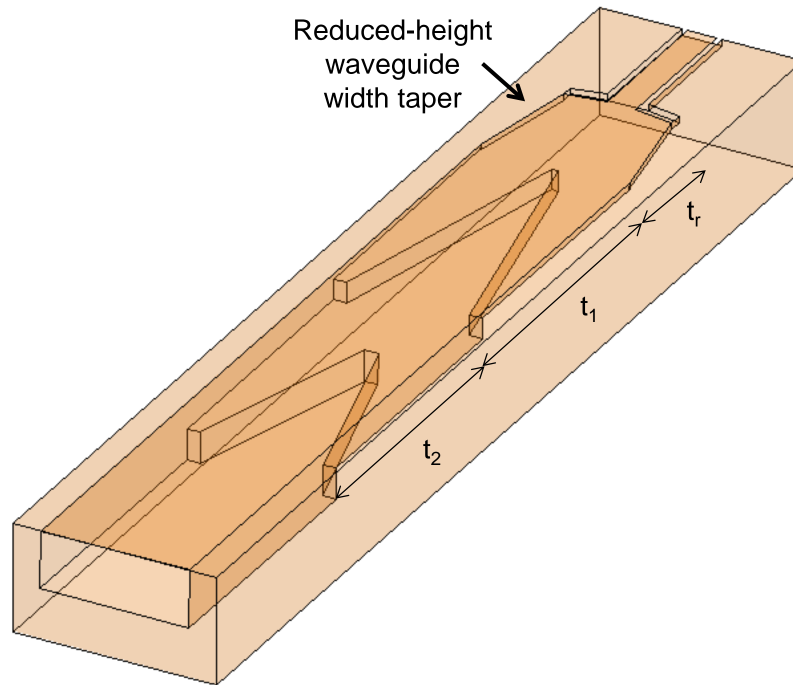

(a)

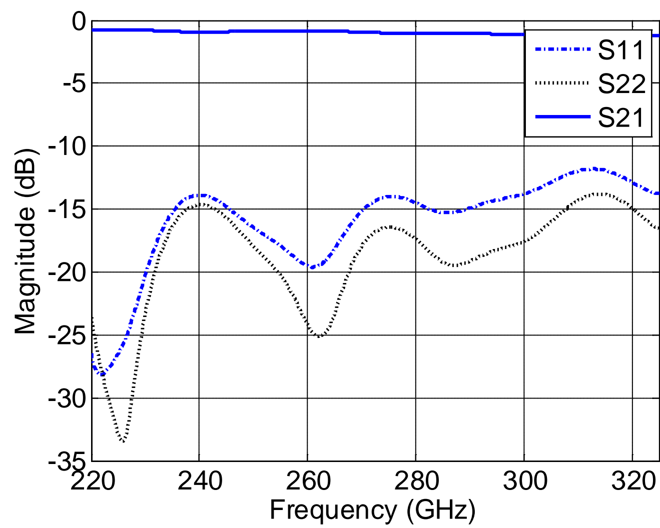

(b)

Figure 2.12 Complete 3-step transition: (a) schematic with optimized dimensions: t_r = 1000µm, t_1 = 2000µm, t_2 = 1500µm; (b) full-wave analysis results of the optimized structure

A major advantage of this transition is that it can conveniently be scaled for terahertz applications. The processes used for the fabrication of this transition offer sufficient accuracy making the design and microfabrication method suitable for extension of the design to higher frequencies.

1.10 Chip Integration

Integration and packaging of active components with the on-wafer micromachined antennas and other passive components is a significant step in the development of the fully integrated MMW radar. As shown in the block diagram of the proposed radar (Figure 1.12), a multiplier chain source is needed to upconvert the output signal from the 20 GHz VCO to feed the antenna on the transmitter channel. A downconverting module (compromised of an LNA, an amplifier, and a mixer all at 240 GHz) is also needed in the receiver channel. A transition from these chips to the on-wafer components is needed to complete the signal chain in the radar front-end.

Conventionally, the active components have been assembled into waveguide-fed blocks which are bulky and not compatible with micromachining technology (Figure 2.13).

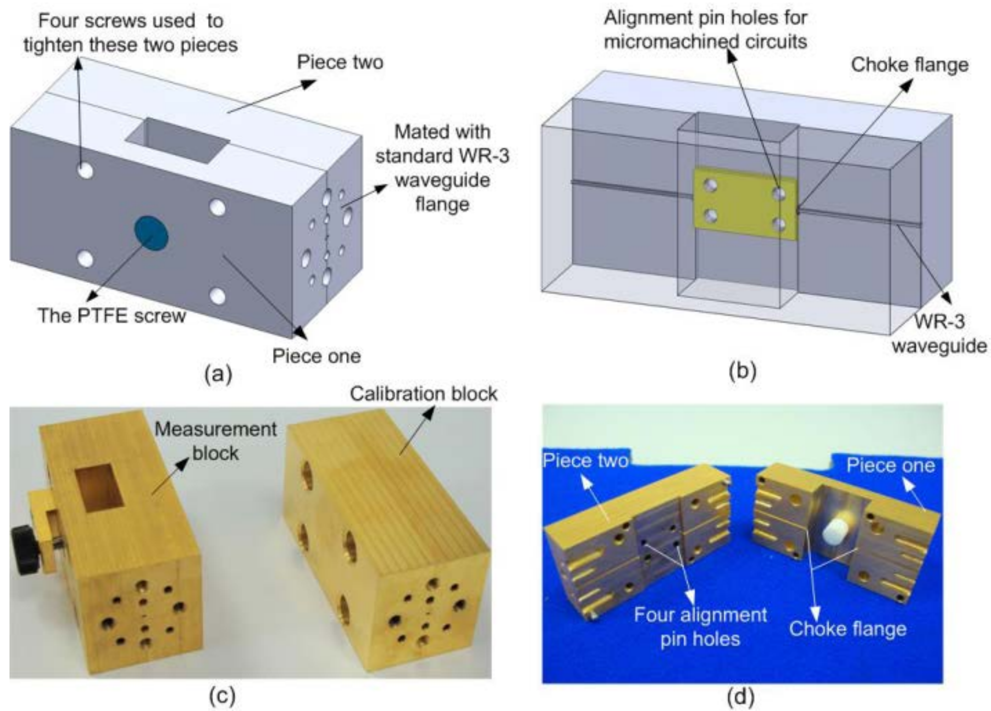

Figure 2.13 Integration of active circuits into metal blocks [64]

To overcome the issues with the conventional methods, a wide band, low loss, and robust integration method compatible with the micromachined radar structure is introduced to integrate the active chips with the on-wafer passive components. This integration method is implemented in three steps as shown in Figure 2.14. The design of the CBCPW line and the CBCPW to waveguide transitions have been presented in the last two sections. The last link needed to complete this chain is an effective transition from the MMIC chip to the CBCPW line.

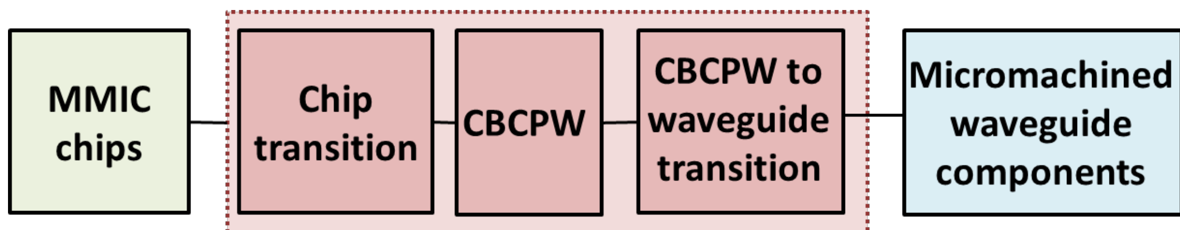

Figure 2.14 The required components for integration of MMIC chips with micromachined radar front-end

A thru wafer chip integration configuration is proposed to complete the signal chain from active components to the antennas as shown in Figure 2.15. In this method the back side of the bottom wafer is patterned and etched to create openings to insert the MMIC chip. The chip is supported from the top by the extension of the top wafer over the opening and fixed in the hole from bottom with a support (i.e. a piece of Styrofoam).

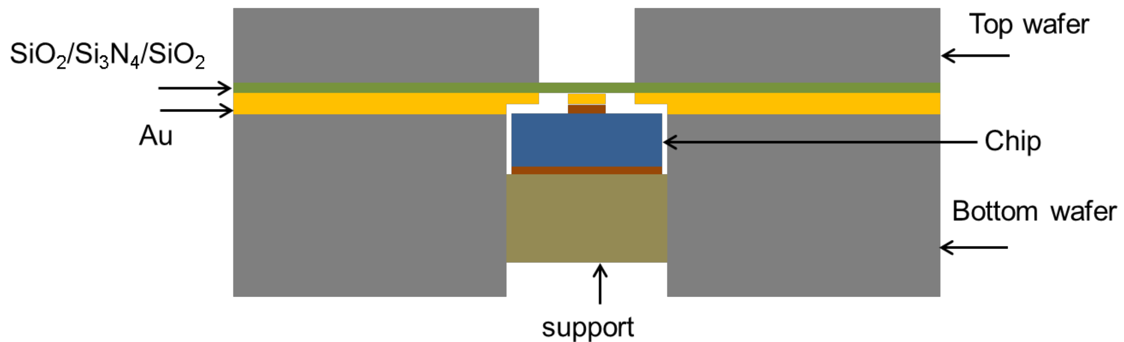

Figure 2.15 The proposed thru wafer chip integration configuration

An RF transition is needed to enable signal transmission from on-chip microstrip line to the CBCPW line. A DC bias path is needed for active MMICs. The design shown in Figure 2.16 is proposed and optimized for minimum insertion loss in the radar operating band. The transition is comprised of a small section of a small-width 50Ω CBCPW section and extensions of membrane-supported signal and ground conductors overlapping with the pads on the MMIC chip.

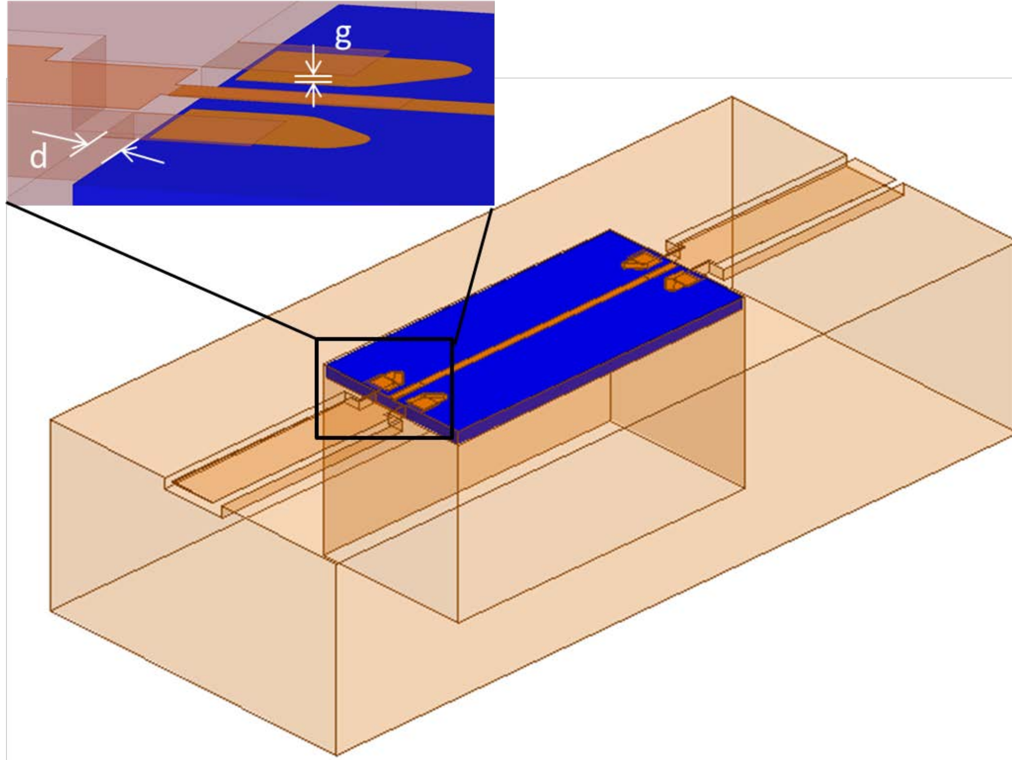

Figure 2.16 The proposed transition from MMIC chip to CBCPW line

Full-wave analysis of the transition is performed in HFSS. The performance of the transition is dependent on two variable parameters: 1) distance from chip edge to the opening wall (d), 2) gap between the chip metal traces to membrane-supported traces (g). Sensitivity analysis results subject to this two parameters is shown in Figure 2.17.

To enhance the transition performance as well as for accurate GSG probe measurements of the MMIC chips, the launch pad design on the chips must be optimized for minimum mismatch loss and substrate mode excitation. Analysis of the current pad design on the chips provided by BAE systems shows poor performance at the radar frequency band. An optimal launch design on the chips is presented in Appendix A.

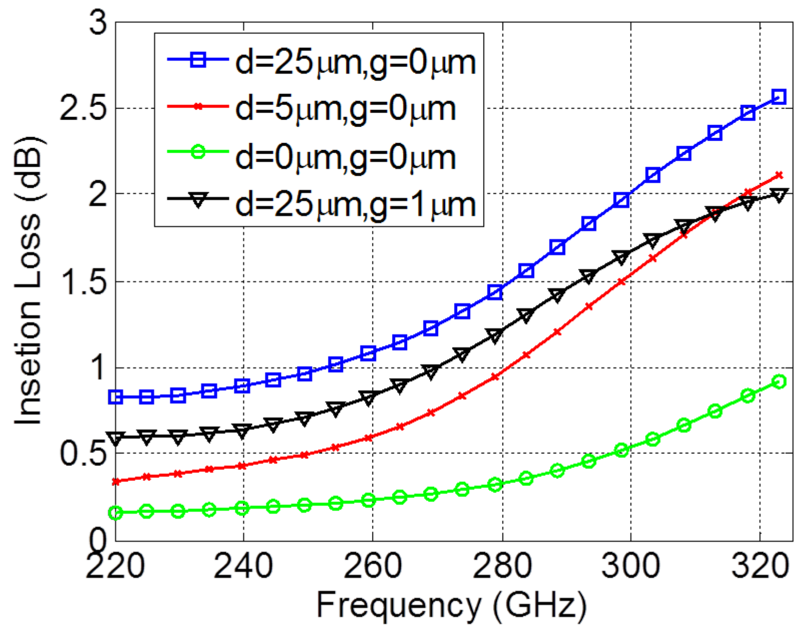

(a)

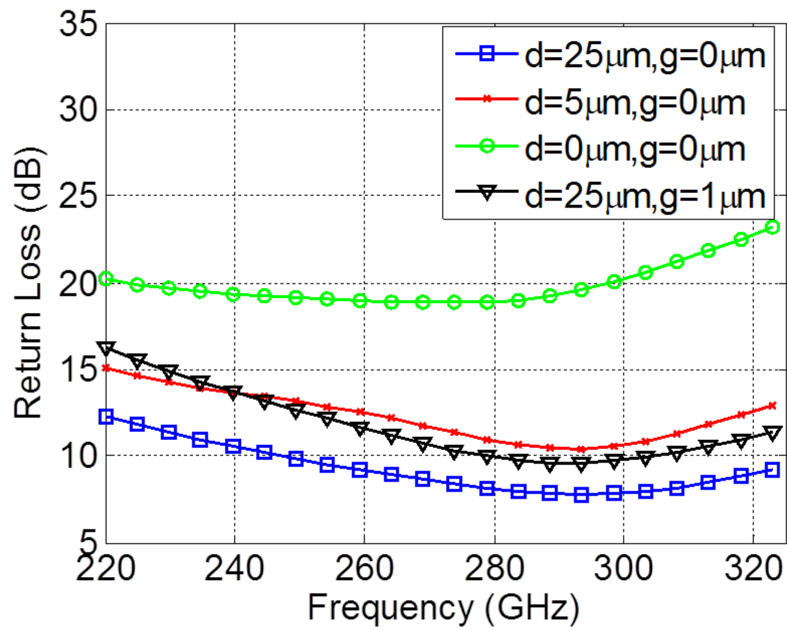

(b)

Figure 2.17 Performance of the chip transition with respect to parameters *d* and *g* (a) insertion loss, (b) return loss

1.11 Directional Couplers

Directional couplers are essential components in the design of RF and microwave systems. As shown in the radar block diagram (Figure 1.12), a single chip is used to provide the 240 GHz signal for both transmitter and receiver to maintain the coherence of the signal in the radar system. Thus, a directional coupler is required to divide the power between transmit antenna and the input to the downconvertor chip on the receiver side. A tight coupling factor (less than 10 dB) is required to provide enough power to drive the mixer on the receiver side.

A wide variety of couplers have been invented and characterized in the past. Coupled line directional couplers based on planar transmission lines are of great interest for MMIC applications due to their simple integration and inherent compatibility with planar circuits. Initially, we designed a micromachined coupled line directional coupler based on the optimal CBCPW line with tight coupling factor (4.4 dB) for the micromachined radar. The proposed design is compatible with the micromachining technology and can be integrated with the radar front-end through CBCPW line. The design of this novel coupler and an on-wafer CBCPW matched load for coupler characterization is presented in Appendix B. Waveguide couplers are another widely used type of directional couplers. These couplers typically have better efficieny compared to coupled line couplers. The microfabrication described in Chapter 3 and the measurement technique described in Chapter 4 allows for fabrication and characterization aperture-coupled couplers. In the next section, design of multiple aperture waveguide couplers with wide band performance and high effieciecy is presented. One of this waveguide couplers are

selected for the MMW radar front-end due to the better performance and simpler fabrication compared to the proposed coupled line CBCPW coupler.

1.11.1 Waveguide Couplers

Waveguide directional couplers are of interest for sub-MMW and terahertz applications due to their low loss and simplicity of integration with other micromachined components. The coupling is achieved through apertures on the common wall between the two adjacent waveguides in these couplers. The multi-step etching process allows realization of multiple apertures with arbitrary heights along the common wall between two adjacent waveguides. Multiple-aperture couplers have been extensively studied in the past [65-67]. The coupling mechanism in an adjacent waveguide coupler with multiple apertures is shown in Figure 2.18. The input power to port 1 is coupled to the adjacent waveguide through the apertures. The quarter-wavelength spacing between the apertures results in cancellation of coupled powers in the backward direction (port 2) and addition of these signals in the forward direction (port 3). A non-uniform taper of the coupled amplitues is typically used to enhance the bandwidth of the coupler [66].

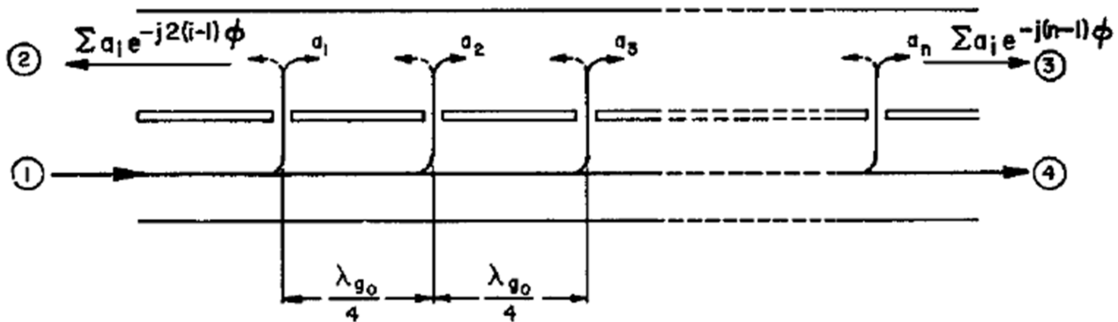

Figure 2.18 Illustration of wave coupling in an *n*-aperture coupler [65]

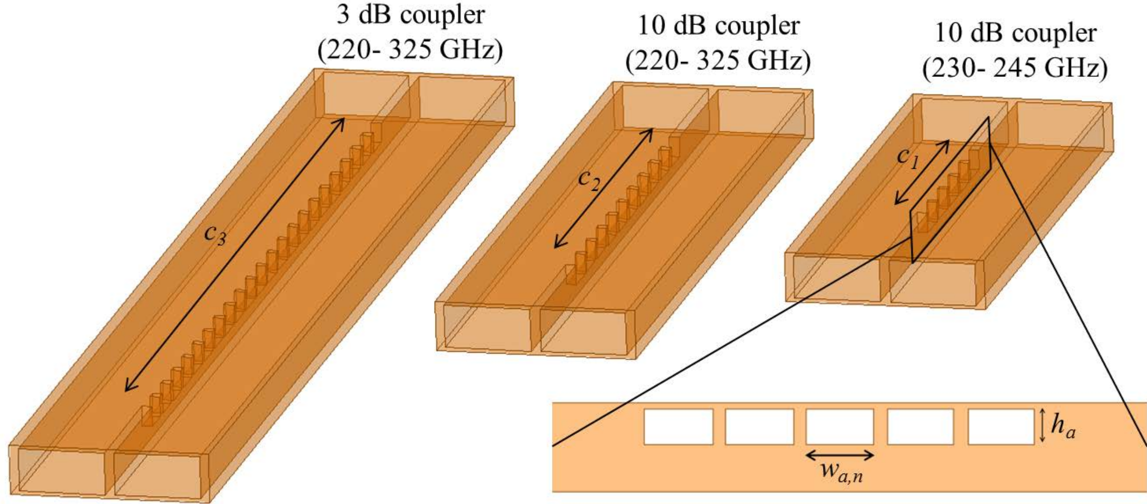

Figure 2.19 Micromachined sidewall aperture couplers:

1) 230-245 GHz 10-dB coupler (c_1=2.76 mm, $w_{a,1}$= $w_{a,5}$=0.4 mm, $w_{a,2}$= $w_{a,4}$= 0.42 mm, $w_{a,3}$=0.495 mm)

2) Full-band 10-dB coupler (c_2=4.36 mm, $w_{a,1}$= $w_{a,10}$=0.31 mm, $w_{a,2}$= $w_{a,9}$= 0.33 mm, $w_{a,3}$= $w_{a,8}$=0.36 mm, $w_{a,4}$= $w_{a,7}$= 0.375 mm, $w_{a,5}$= $w_{a,6}$=0.385 mm)

3) Full-band 3-dB coupler (c_3=9.785 mm, $w_{a,1}$= $w_{a,22}$=0.335 mm, $w_{a,2}$= $w_{a,21}$= 0.34 mm, $w_{a,3}$= $w_{a,20}$=0.345 mm, $w_{a,4}$= $w_{a,19}$= 0.35 mm, $w_{a,5}$= $w_{a,18}$=0.355 mm, $w_{a,6}$= $w_{a,17}$=0.36 mm, $w_{a,7}$= $w_{a,16}$=0.365 mm, $w_{a,8}$= $w_{a,15}$=0.37 mm, $w_{a,9}$= $w_{a,14}$=0.375 mm, $w_{a,10}$= $w_{a,13}$=0.38 mm, $w_{a,11}$= $w_{a,12}$=0.385 mm). h_a=0.2 mm for all apertures.

Following the design procedure for non-uniform aperture arrays, different directional couplers with different bandwidths and coupling coefficients are designed. These designs are then optimized using full-wave simulations. Figure 2.19 shows the optimized design of three different couplers: 1) 10-dB coupler (230-245 GHz) for the MMW radar integration, 2) 10-dB coupler (220-325 GHz), 3) 3-dB coupler (220-325 GHz). The first coupler is designed for integration with the proposed radar front-end. The

two other couplers full band designs that can be utilized for wideband application. The simulated performances of the optimized designs are shown in Figure 2.20.

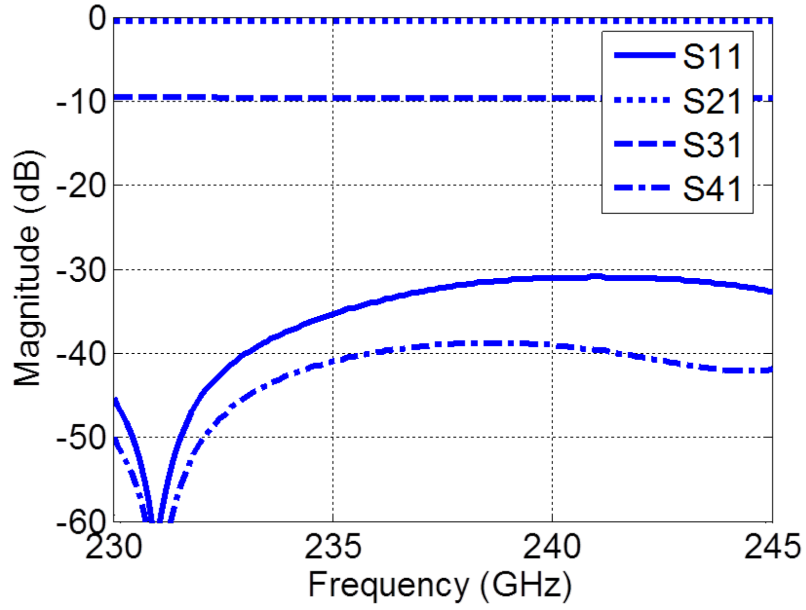

(a)

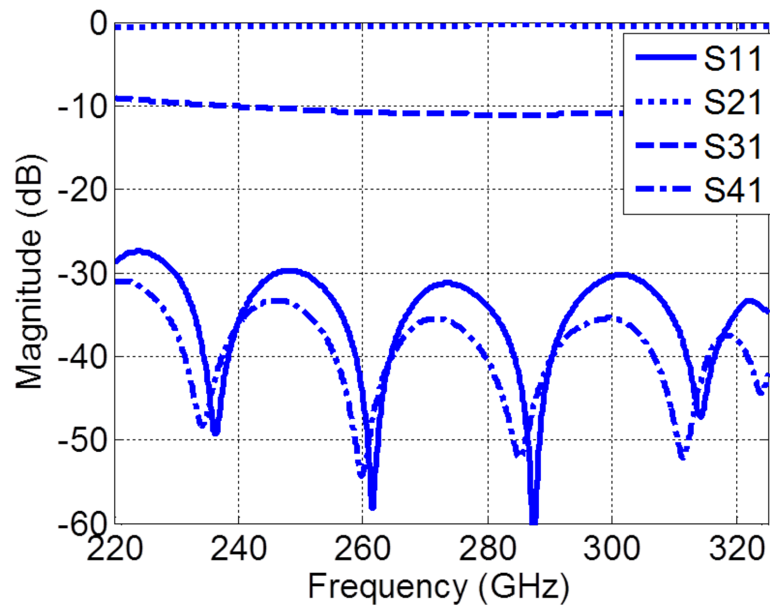

(b)

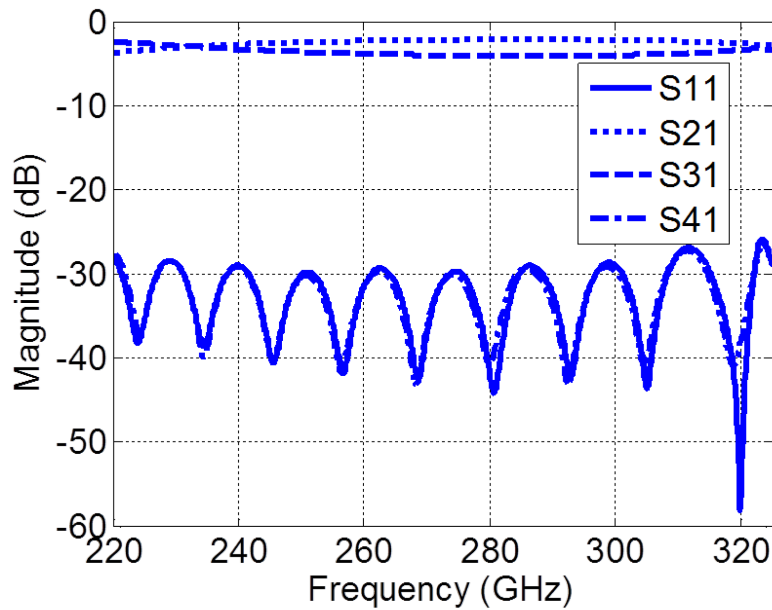

(c)

Figure 2.20 Simulated performance of the optimized couplers: (a) 230-245 GHz 10-dB coupler, (b) Full-band 10-dB coupler, (c) Full-band 3-dB coupler

1.12 Summary

The design and optimization of the micromachined components needed for the MMW radar has been discussed in this chapter. The designed components and transitions are compatible with micromachining technology and can be fabricated using the same set of microfabrication processes. The fabrication and characterization of these components are described in Chapter 3 and Chapter 4 respectivly.

CHAPTER 3
THE MICROFABRICATION PROCESSES

In this chapter, the microfabrication processes for realization of the micromachined radar structure are presented. As discussed in Chapter 2, the passive components (e.g. the waveguide antenna, CBCPW, CBCPW to waveguide transition, chip integration, and waveguide coupler) are designed in such a way that they can be fabricated on the same wafer through the same series of microfabrication processes.

The fabrication of the micromachined radar components is performed on two 4" silicon wafers. The schematic steps of the radar integration process are shown in Figure 3.1. The rectangular waveguide antenna and the other multi-step (2.5 dimensional) structures are realized on a 1-mm thick silicon wafer that is named "bottom wafer". DRIE multi-step etching processes are used to realize these structures. The top cover for the waveguide-based structures, suspended CBCPW line, and the antenna slots are realized on a 0.25-mm thick silicon wafer that is named "top wafer". The suspended features are implemented on a thin dielectric membrane ($SiO_2/Si_3N_4/SiO_2$). The two wafers are then bonded using a gold-to-gold thermocompression bonding technique to form the complete micromachined structure.

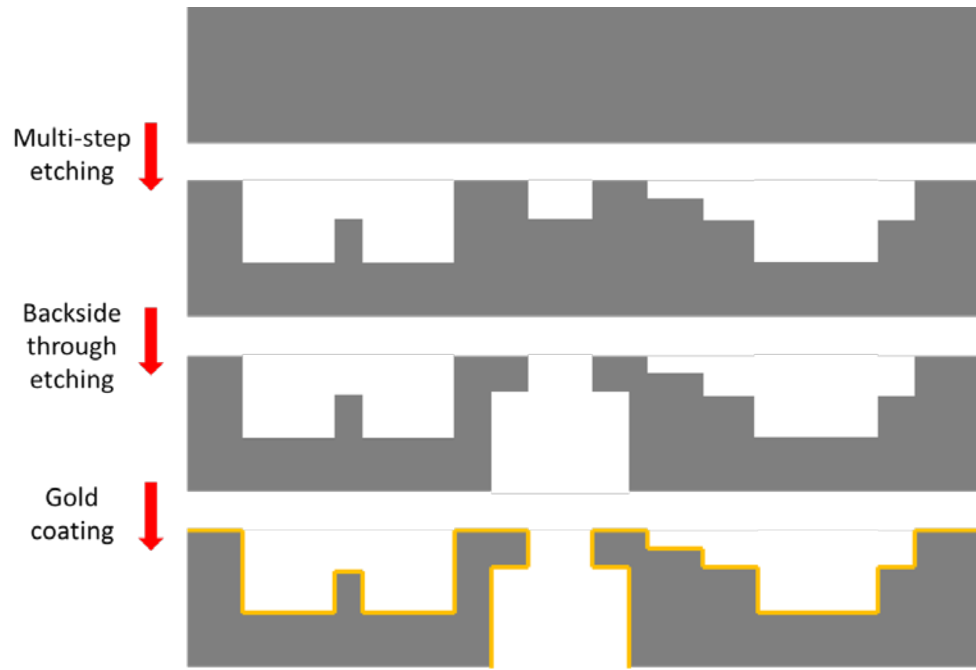

(a)

(b)

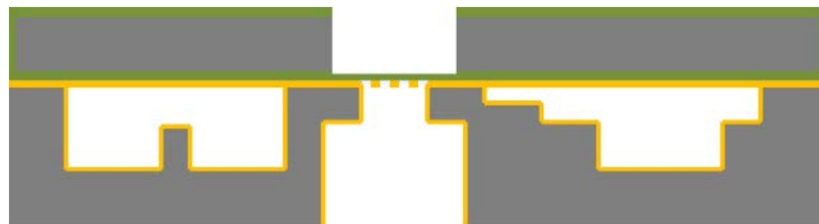

(c)

Figure 3.1 General diagram of the radar microfabrication processes: (a) The bottom wafer, (b) The top wafer, (c) Bonded wafers

1.13 Bottom Wafer

As shown in Figure 3.1 (a), the fabrication of the bottom wafer involves three major steps. In the first step, the multi-step components are etched on the top side of the wafer using a deep reactive ion etching (DRIE) process. The second step is etching through the wafer from the backside to create openings for chip integration. In the last step, the surface of the wafer is coated with a layer of gold.

1.13.1 DRIE Multistep etching

The DRIE method is a highly anisotropic etch process suitable for creating deep features with vertical walls in silicon substrates. In the Bosch process which is utilized here, the vertical structures are achieved through repetition of a two-phase cycle: 1) the standard plasma etch with SF_6 flow, 2) deposition of a passivation layer with flow of C_4F_8 gas.

The standard method to create multi-step structures is to use multiple-masks as described in [36]. In this method, to achieve an *N*-step structure, the wafer is patterend successively with *N* different mask layers (Figure 3.2 (a)). The Nth step is etched first and then the Nth mask is removed to continue with the $(N\text{-}1)^{th}$ step etch. This process is repeated to realize all the *N* steps (Figure 3.2 (b)-(g)). For our application, three different mask layers are used to realize three-step structures. Silicon dioxide (SiO_2) layers are deposited and patterned as masks for the first and second step etching and photoresist (5µm thick SPR 220) is used as the mask layer for the third step etching.

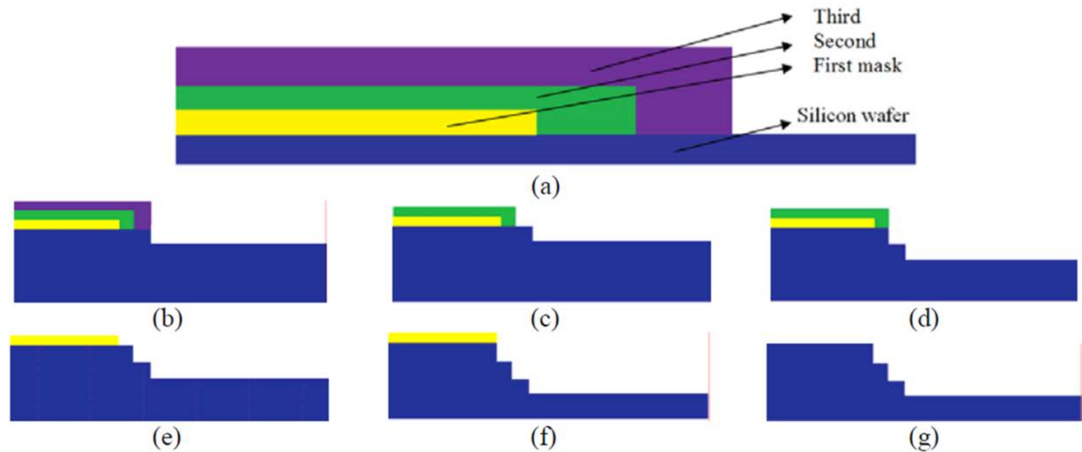

Figure 3.2 Multi-step etching using the multi-mask method [36]

Further examination of the micromachined waveguides fabricated using this method revealed that this process can cause roughness and irregularities in the transitions between successive DRIE steps on the sidewalls as shown in Figure 3.3. This roughnesses increase power loss along the waveguide and since the beam scanning antenna is comprised of meanderline waveguides the overall efficiency of the antenna will deteriorate.

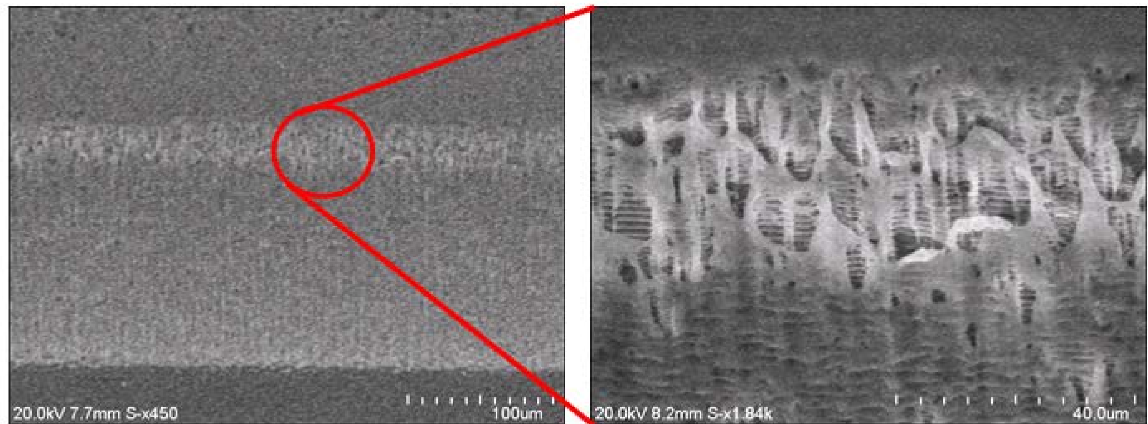

Figure 3.3 SEM photo of the transition between DRIE steps

1.13.1.1 The Glass-in-Silicon Reflow Technique

A novel method for multi-step etching of the silicon wafer based on a glass reflow technique was proposed and investigated to improve the sidewall surface quality. The glass-in-silicon technique has been used for the packaging of microsystems [68]. The schematic diagram of the steps for this method is shown in Figure 3.4. In the first step, a thick photoresist layer (10µm thick AZ 9260) is spun on the wafer and patterned with the mask for the deepest trenches on the wafer (Figure 3.4 (a)). The sample is then etched to the final desired depth using a single DRIE run (Figure 3.4 (b)). In the next step the trenches are filled with glass. This is done by anodically bonding a borosilicate glass wafer to the silicon wafer under vaccum at 300°C and 1000V (Figure 3.4 (c)). The bonded wafer is then heated at 750°C (Figure 3.4 (d)), where the vaccum in the trenches pulls in the glass (see Figure 3.5). At this stage the surface of the bonded stack is highly nonplanar. The excess glass is removed using mechanical lapping to reach the silicon surface (Figure 3.4 (e)). A subsequent chemical-mechanical polishing (CMP) step is necessary to prepare the surface for the next lithography step. Next, the surface is patterned with the second mask and etched to the desired depth (Figure 3.4 (f)-(g)). The glass in the trenches is removed using a wet etching process in hydrofluoric acid (Figure 3.4 (h)) to realize a two-step structure. Steps (c) to (h) can be repeated to add another step each time for multistep structures. Alternatively, since steps other than the main waveguide part form a very small fraction of the meanderline antenna array, these steps can be realized with multiple masks without adding much to the overall loss of the array due to sidewall roughness. The waveguide sidewalls fabricated using this method is shown in Figure 3.4. Surface profile measurements using introferometry shows less than 1µm roughness on the sidewalls.

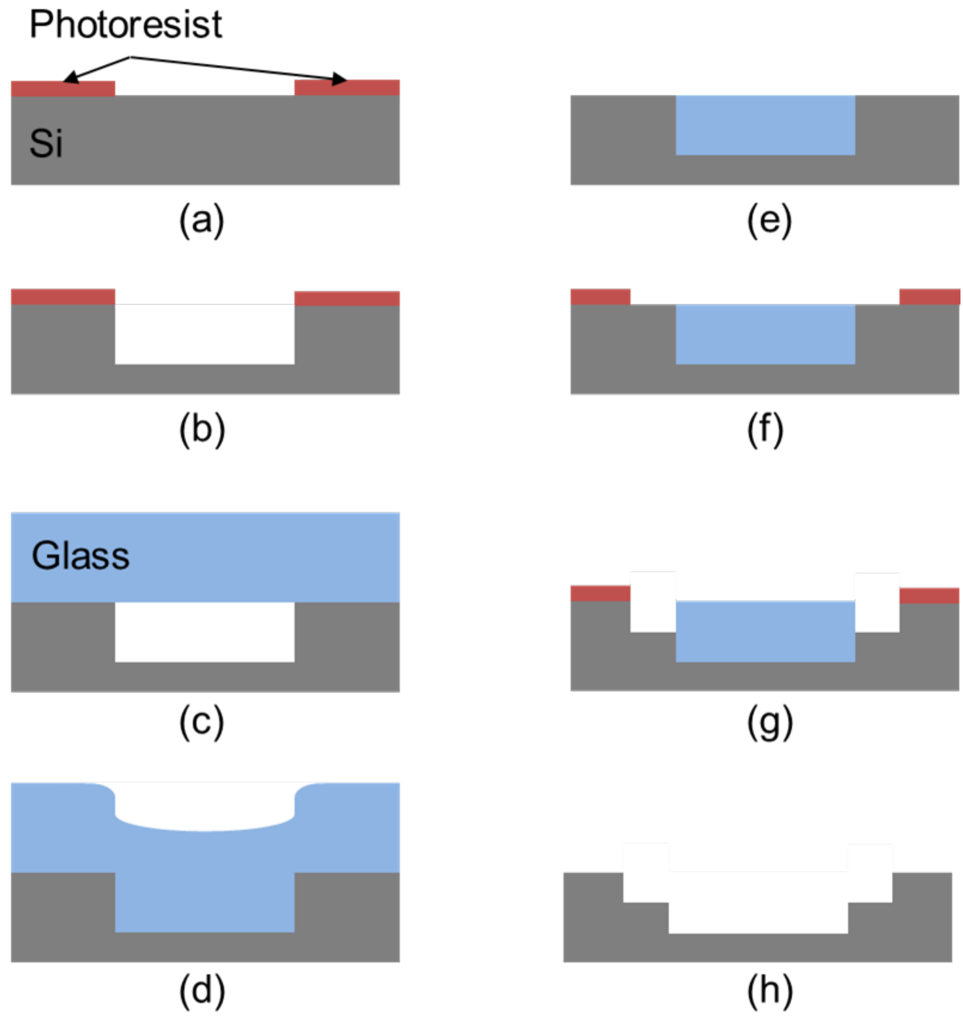

Figure 3.4 Process flow diagram of multistep etching using glass reflow technique

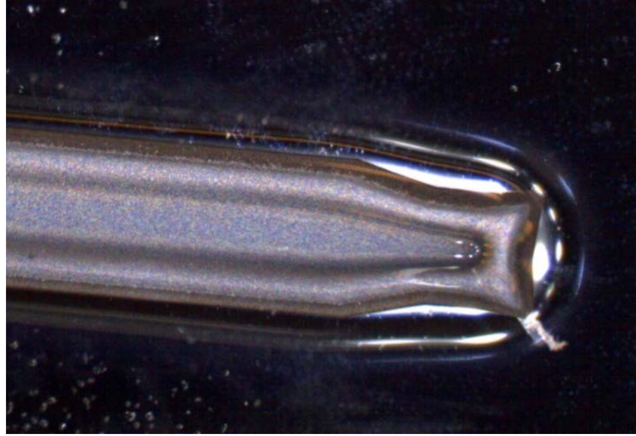

Figure 3.5 Waveguide trenches filled with glass

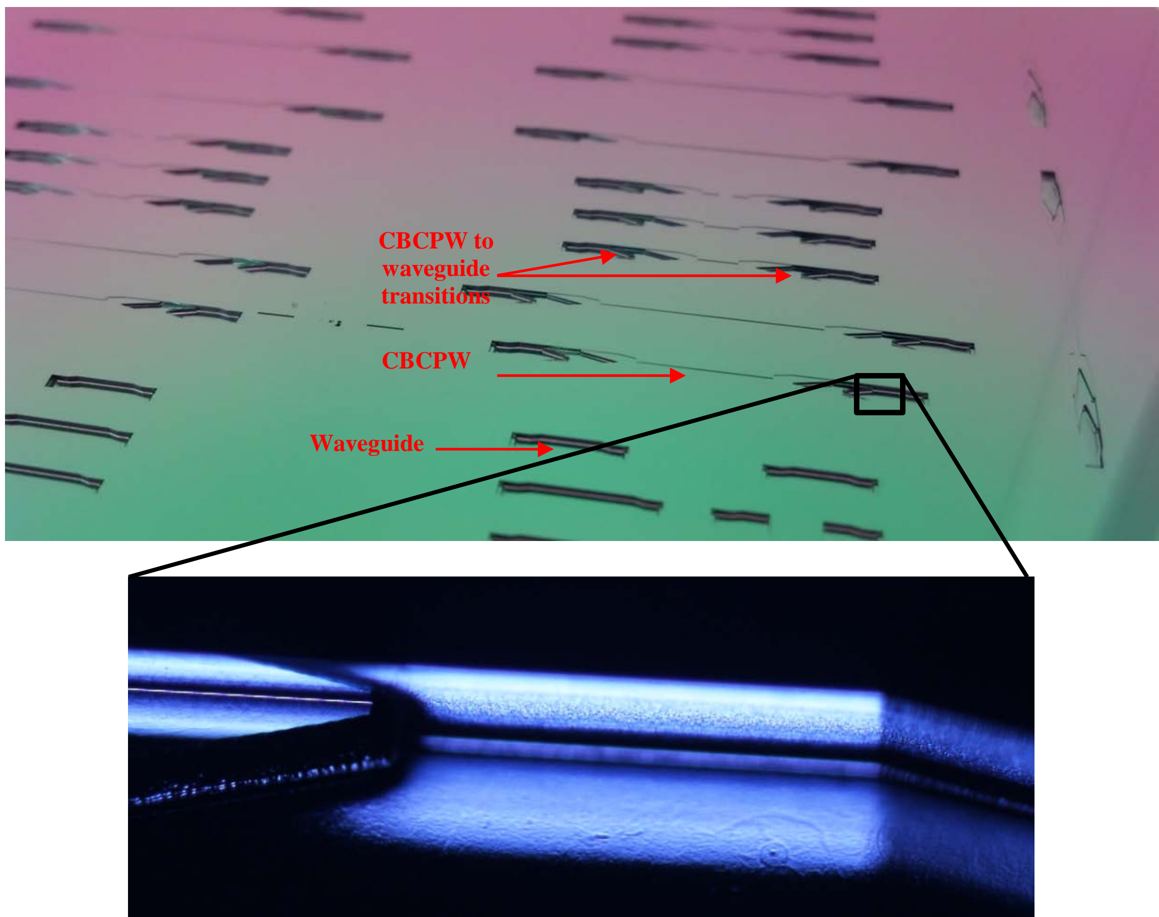

Figure 3.6 Multi-step structures fabricated using glass-in-silicon reflow technique

1.13.1.2 Side-Wall Smoothing

A wet chemical oxidation process is employed in order to further reduce the sidewall roughness on the multi-step micromachined sample. The phenomenon of roughness reduction by oxidation smoothing is explained by the Gibbs–Thompson relation [69]. The relation signifies that the chemical potential of a surface is dependent on the curvature of the surface. Essentially, the peaks of a rough surface have a higher reactivity than the troughs of the roughness. The differential reaction rate occurring on a rough surface results in roughness amplitude reduction. In other words, the smoothing is mainly due to the isotropic nature of oxidation. The surface is oxidized in the wet oxidation furnace at atmosphere pressure and 1100°C temperature. It takes 9 hours to reach 2µm oxide thickness. The oxide layer is then stripped in hydrofluoric acid. This process can be repeated to further smooth the sidewalls. The sidewall profile after one oxidation process shows that roughness is less than 0.5µm as shown in Figure 3.7.

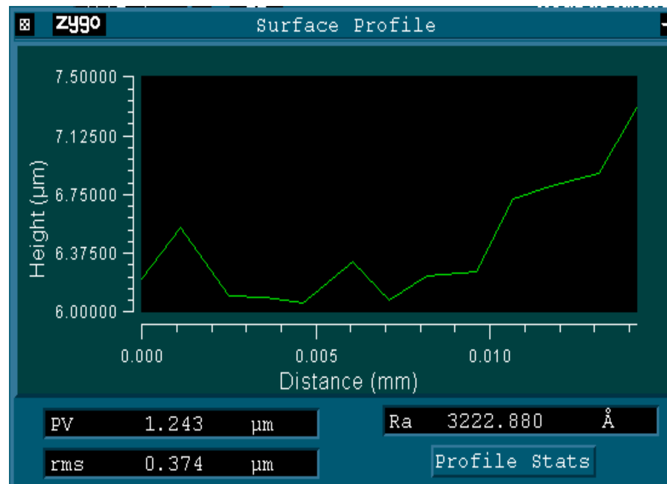

Figure 3.7 Sidewall profile after oxidation

1.13.2 Backside Through Etch

As shown in the chip integration design, the MMIC chips are inserted form the backside of the wafer. The openings are etched from the topside of the wafer down to the depth of the waveguides (430μm) with dimensions equal to the size of the chips. The backside of the wafer is patterned with the openings of much larger size to facilitate the chip insertion process. The mask layer for the backside etch is a 10 μm thick AZ 9260 photoresist layer. The backside opening patterns are aligned with the top patterns using the backside alighnment technique.

1.13.3 Metalization

The last step in prepration of the bottom wafer is to cover the surface of the micromachined structurs with a conducting material. Gold is selected as the coating material due to its unique characteristics: high conductivity, resistanse to oxidation, and compatibility with the thermocompression bonding process. Before gold deposition, a barrier layer (silicon dioxide) is deposited on the surface to stop silicon diffusion into the gold layer during the high temperature bonding process. Sputtering is used for gold deposition to ensure sufficient coverage on the sidewalls (50% sidewall coverage). A thin layer of Titanium (1500˚A) is sputterd as adheision layer. Then 1.5μm of gold is sputterd to ensure complete coverage of sidewalls.

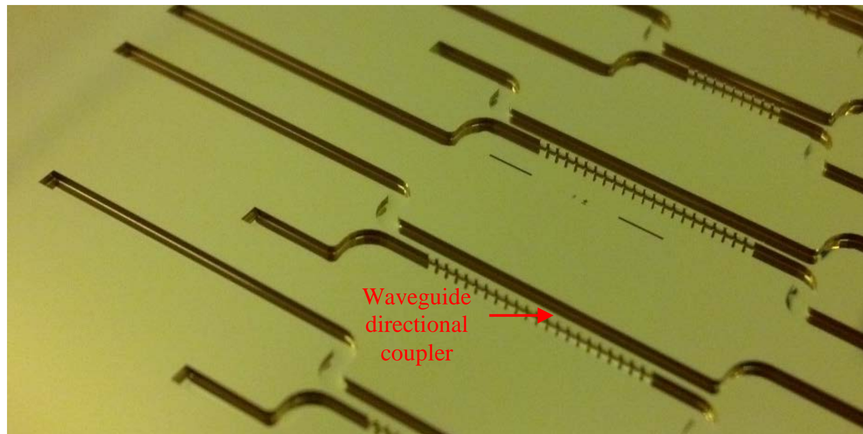

(a)

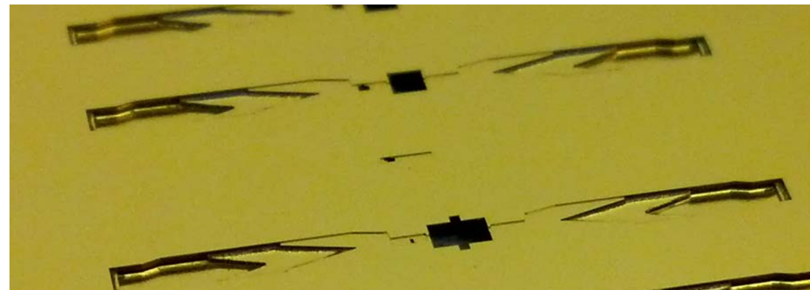

(b)

Figure 3.8 The bottom wafer after metallization (a) couplers, (b) chip integration transitions

1.14 Top Wafer

The patterns of the CBCPW center conductor, the transition to reduced-height waveguide described in Chapter 2 and the waveguide openings and slot arrays described in Chapter 4 are implemented on the top wafer. Since in design of these features are suspended over the bottom wafer structures, these patterns must be realized over a thin membrane which will be released from the silicon wafer.

1.14.1 Free-Standing Membrane

The membrane required for this application should be very thin to minimize its effect as a dielectric layer on the performance of the designed structures. At the same time, it should be strong enough to be released over relatively large areas. In addition, it should withstand the high temperature (~400˚C) of thermocompresion bonding process. A 1 μm thick low-stress stack of $SiO_2/Si_3N_4/SiO_2$ film is selected which encompasses all the above mentioned characteristics. The stack is deposited using low-pressure chemical vapour deposition (LPCVD) process.

1.14.2 Gold Patterning

The features are patterned on the top wafer using a lift-off process. This technique is selected over standard wet etching process since it can create features with the sharp edges and high resolution required for this application. In this method, first a layer of photoresist (5μm thick SPR220) is spun over the wafer and patterned with a mask with the complement pattern of the actual features. Then the metal layers (Cr 500˚A / Au 5000˚A) are evaporated over the surface. Evaporation method is used for metal deposition since it has very poor sidewall coverage which is essential for the lift-off process. Finally, the metal layer over the patterned areas is lifted-off by removing the photoresist in a solvent (acetone, nanostrip, etc.). The lift-off steps are shown in Figure 3.9.

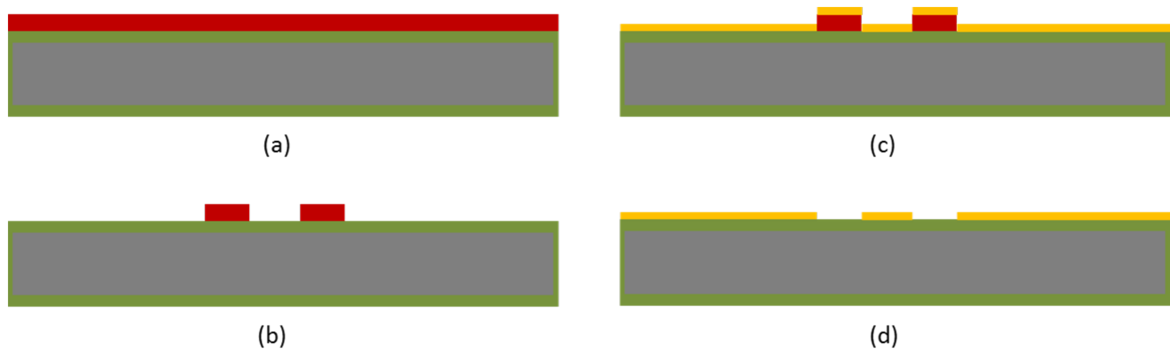

Figure 3.9 Process flow diagram of lift-off process

1.14.3 Membrane Release

The silicon substrate must be etched over the features down to the membrane layer to release the suspended structures. The $SiO_2/Si_3N_4/SiO_2$ layer on the backside of the top wafer is patterned with the desired openings over the features. The openings are aligned with the topside features using backside alignment. The openings are then etched using DRIE. Fabricated top wafer samples are shown in Figure 3.10.

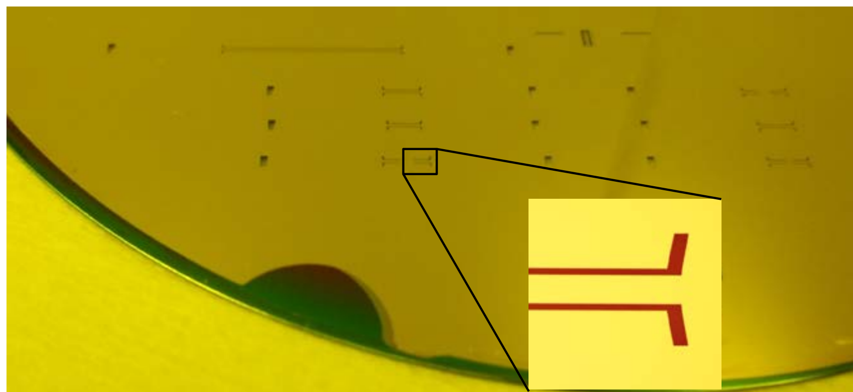

(a)

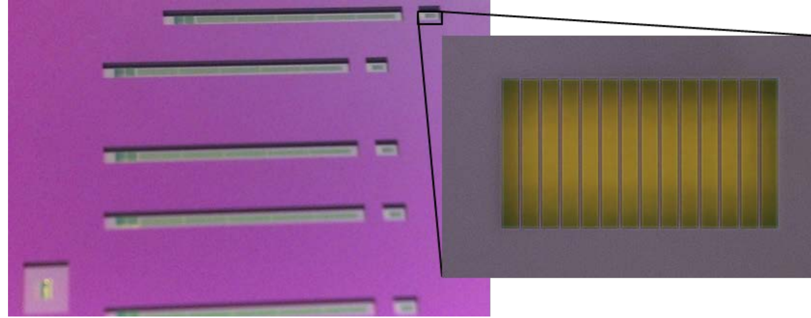

(b)

Figure 3.10 Top wafer after membrane release (a) The membrane supported CBCPW line and the waveguide to CBCPW transition (top view), (b) slot array antennas (back view) (see Chapter 4)

1.15 Au-Au Thermocompression Bonding

The bottom and top wafers are aligned and bonded using Au-Au thermocompression bonding to form the completed structures. This bonding process ensures continuity of current flow between top and bottom surfaces of thewaveguides and structures. The bonding is performed under approximately 2000 kPa pressure and 380˚C temperature for 40 minutes [70, 71]. The quality of the bonding between the surfaces is visually inspected by checking the cross section of diced waveguide sections (Figure 3.11).

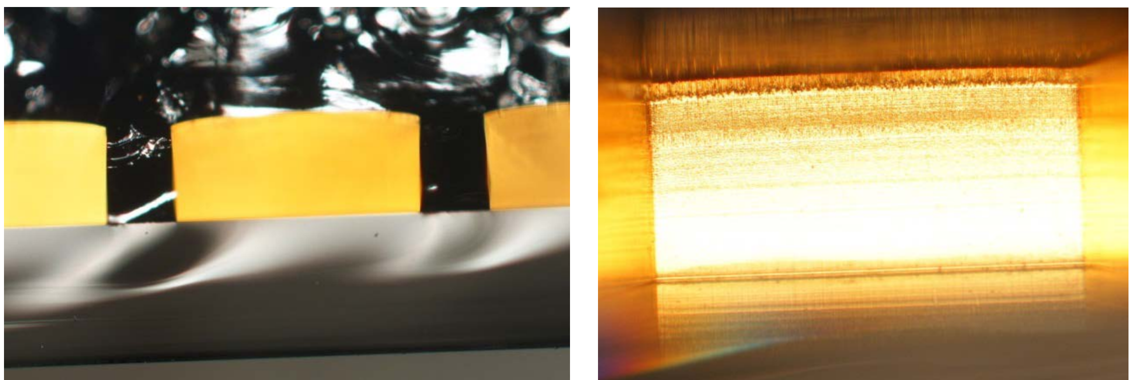

(a) (b)

Figure 3.11 Cross-section of diced waveguide sections (a) outside view (b) inside view

1.16 Summary

The microfabrication steps for realization of the components for the proposed MMW radar are discussed in this chapter. Fabrication of the components is performed on two silicon wafers. DRIE techniques are used to create multistep structures on the bottom silicon wafer. A novel multistep etching process using glass-in-silicon reflow technique is utilized to enhance the sidewall profile quality. The membrane-supported features are realized on the top silicon substrate. The two substrates are ultimately bonded to form the complete structures. The characterization of the fabricated structures is described in the next chapter.

CHAPTER 4
MMW AND SUB-MMW ON-WAFER MEASUREMENT METHODOLOGY

1.17 Introduction

In recent years, significant efforts have been made towards development of active and passive components for sub-MMW and THZ radars and communication systems in recent years. Waveguides are of particular interest to realize passive components at these high frequencies due to their low insertion loss and high power handling capability compared to planar transmission lines. Mechanical machining cannot provide the needed accuracy and flexibility in fabrication of RF front-ends for sub-MMW band and above. For this reason various waveguide-based passive components are being developed using silicon micromachining [57, 64, 72-76]. However, measurement and characterization of such components has always been a serious challenge.

In this chapter, novel measurement methods for characterization of on-wafer components are presented. In Section 4.2, the conventional methods for on-wafer S-parameter measurement and their limitations are discussed. Then a novel on-wafer waveguide probe measurement technique is proposed in Section 4.3. This measurement technique is used to characterize the micromachined waveguides, CBCPW line, the waveguide to CBCPW transition and the on-wafer chip transition. A novel non-contact S-parameters measurement technique for characterization of multi-port on-wafer devices is proposed in Section 4.5. First the theory of the measurement technique is described based on the circuit model. Then

the design of the coupling slot array and the analysis of the probe measurement configuration are presented. A broadband matched load is realized by a micromachined waveguide slot array traveling-wave antenna. This measurement technique is utilized to characterize the micromachined waveguide directional couplers. Finally, a summary of this chapter is presented in Section 4.6.

1.18 Conventional Measurement Methods

1.18.1 GSG Probes

Ground-signal-ground (GSG) probes have been conventionally used for characterization of on-wafer planar components. We initially utilized this method to characterize the micromachined components. The GSG probe measurement setup is shown in Figure 4.1 (a). A transition from the CBCPW to on-substrate conventional CPW is required to enable measurement of the micromachined components using GSG probes. The design of this transition is presented in Appendix A. In order to perform measurements, GSG probes are brought into contact with the corresponding pads on the wafer as shown in Figure 4.1 (b).

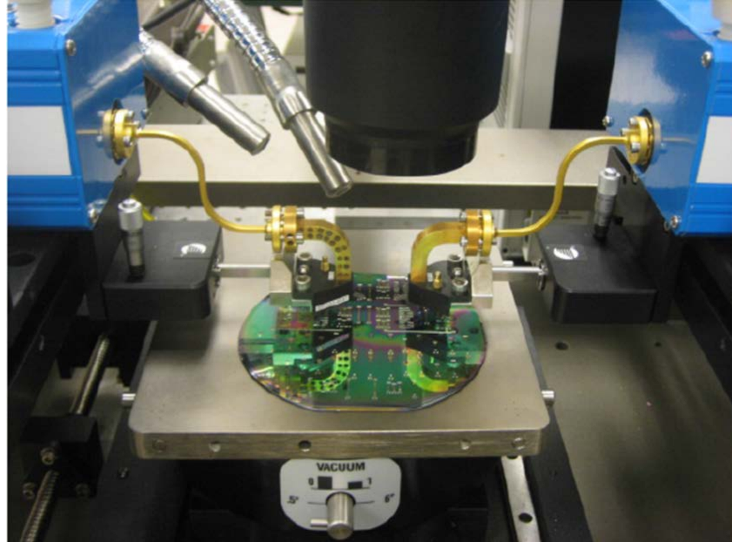

(a)

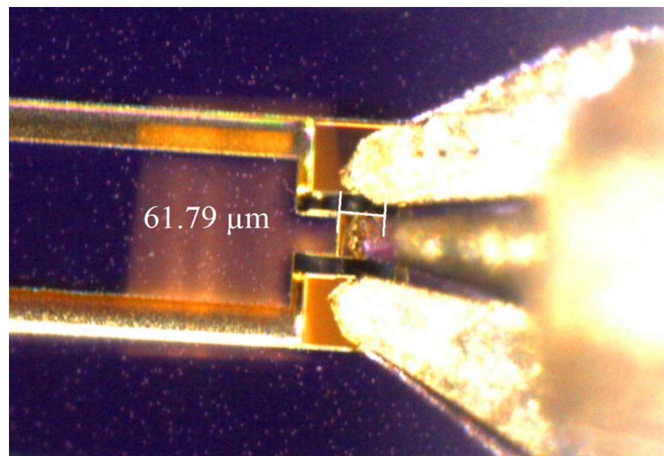

(b)

Figure 4.1 (a) GSG probe measurement setup (220GHz-325 GHz), (b) the probe tips in contact with the on-wafer pads

However, application of these probes at high frequencies are severely limited due to the errors associated with probe tips and the pad parasitics, probe positioning, unbalanced ground currents, contact resistivity [77-80]. These probes also have a limited lifetime due to wear and damage to the gold contacts resulting from repeated use [79]. The

on-wafer calkits needed for calibrating GSG probe systems are also very sensitive and subject to wear and damage due repeated contact with probes.

1.18.2 Test Fixtures

The other common method for characterization of micromachined components is dicing and mounting the individual components onto a test fixture with standard waveguide flanges [64, 72-75] (see Figure 4.2).

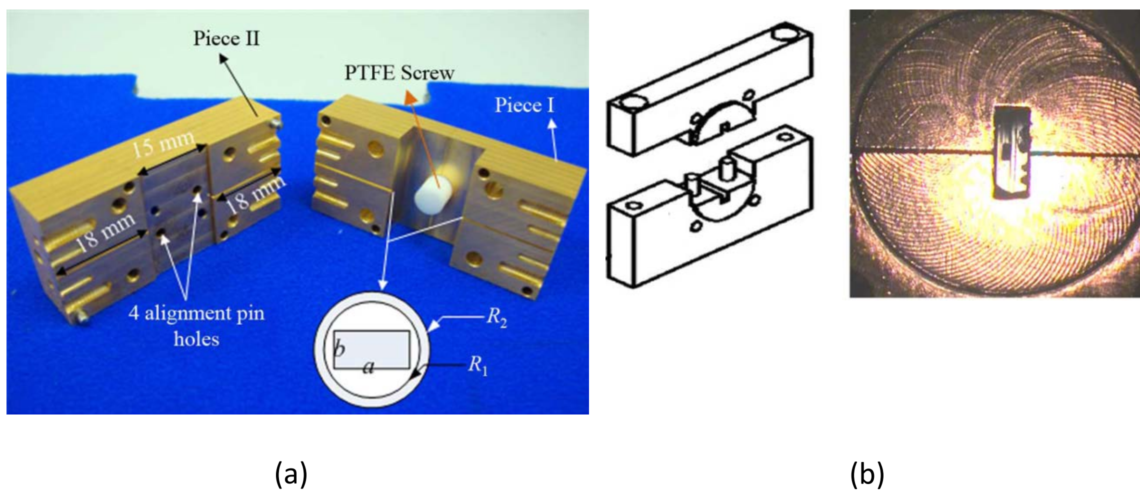

(a) (b)

Figure 4.2 Examples of test fixtures for characterization of micromachined components [64, 74]

This method is subject to measurement errors due to misalignment and fixture imperfections. Calibration of rectangular waveguides at high frequencies is also very sensitive to waveguide aperture dimensions and mechanical alignment [81]. In addition, characterization of many components on a single wafer using this method would take significant amount of time and effort.

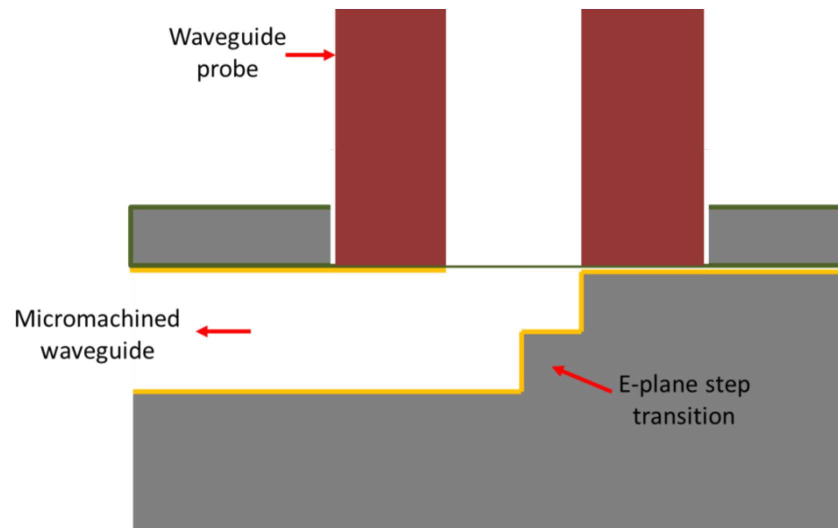

Figure 4.3 Schematic of the proposed waveguide probe measurement technique

1.19 The On-Wafer Waveguide Probe Measurement Technique

A novel waveguide probe measurement method is developed in collaboration with another student in our research group to circumvent the issues associated with the GSG probe measurements at MMW and higher frequencies. In this technique, waveguide probes are used to perform full S-parameter characterization of the transitions. The schematic of the proposed method is shown in Figure 4.3. An E-plane transition from the horizontal on-wafer micromachined waveguides to the vertically directed WR-3 waveguide is designed. The top wafer is etched over the E-plane transition to enable direct contact of the waveguide probe with the on-wafer waveguide. The openings on the top wafer have the same dimensions as those of the WR-3 probe cross section to facilitate the probe alignment with the on-wafer waveguides.

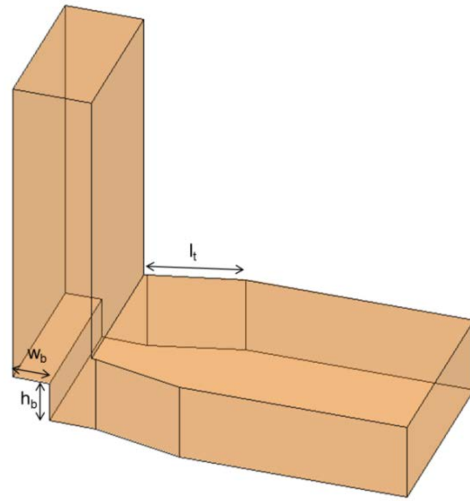

(a)

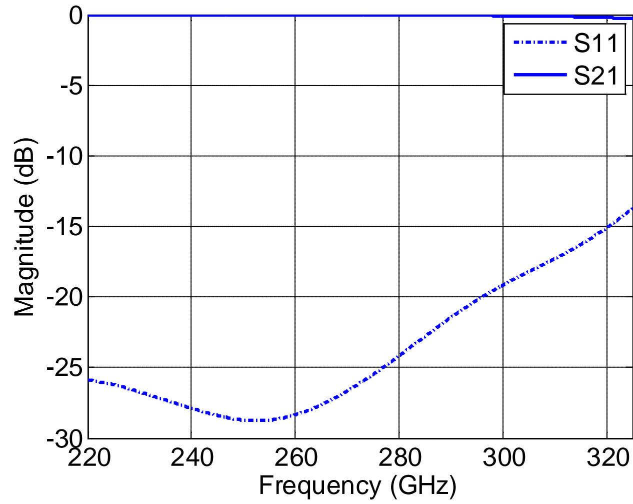

(b)

Figure 4.4 E-plane transition (a) schematic (b) full-wave analysis results of the optimized structure ($h_b = w_b$= 230μm, l_t =540μm)

1.19.1 E-Plane Step Transition

The transition consists of a width taper section followed by an E-plane bend with a single step to the vertical WR-3 waveguide, as shown in Figure 4.4 (a). The height and

width of the step (h_b ,w_b) and the taper length (l_t) are optimized to achieve maximum return loss over the entire J-band. Full-wave analysis of this transition shows more than 13.5 dB return loss and less than 0.3 dB insertion loss in the entire J-band (Figure 4.4 (b)).

1.19.2 Waveguide Choke

As can be noticed in Figure 4.3, the thin dielectric membrane on the top wafer does not allow direct electrical contact between the waveguide probe and the on-wafer waveguide surface. In addition, the interface between the probe and the waveguide opening may be uneven due to mechanical cut of the waveguide probe which can result in a non-perfect contact between the two surfaces. This imperfection can result in reflections and resistive loss by interrupting the currents on the waveguide walls. This also affects the repeatability of the measurement method since the return loss at contact point would be a function of the electrical contact quality.

A waveguide choke on the cross section of the waveguide probes is designed to solve this problem. A waveguide choke presents low input impedance where it meets the broad wall of the waveguide. Figure 4.5 shows the cross section view of a probe with choke where it meets the wafers surface. The quarter-wave shorted stub presents a high impedance at the wafer surface:

$$Z_1 = 0, \qquad Z_2 = \frac{Z_{w1}^2}{Z_1} \to \infty \tag{4.1}$$

where Z_{w1} is the characteristic impedance of the vertical stub. Therefore, there would be low impedance (Z_a) at the transition point from the waveguide probe to the on-wafer probe regardless of the quality of the contact between the surfaces (Z_f):

$$Z_a = \frac{Z_{w2}^2}{Z_2 + Z_f} = 0 \quad (4.2)$$

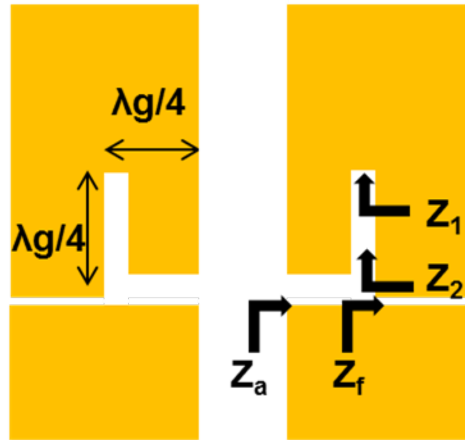

Figure 4.5 Cross section view of the waveguide choke

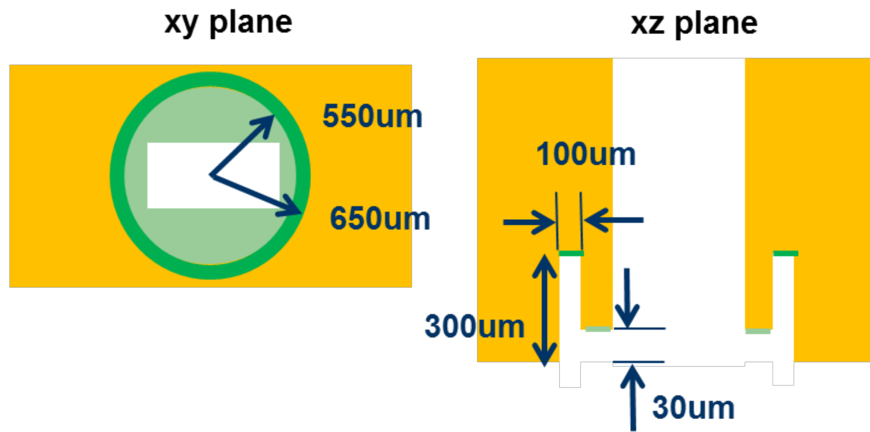

Figure 4.6 The optimized choke design with the parameters specified for WR-3 waveguide

The choke is designed on the cross-section of the probe to form an effective radial transmission line in the narrow gap between the two surfaces. The design includes a short at the bottom of the milled slot, a quarter wave stub to an open at the bottom edge of the figure and a final quarter wave transition to a short at the edge of the waveguide. The design parameters have been optimized to minimize return loss over J-band (see Figure 4.6). Full-

wave analysis of the optimized structure shows return loss better than 20dB over the J-band for a 20μm gap between the two surfaces as shown in Figure 4.7.

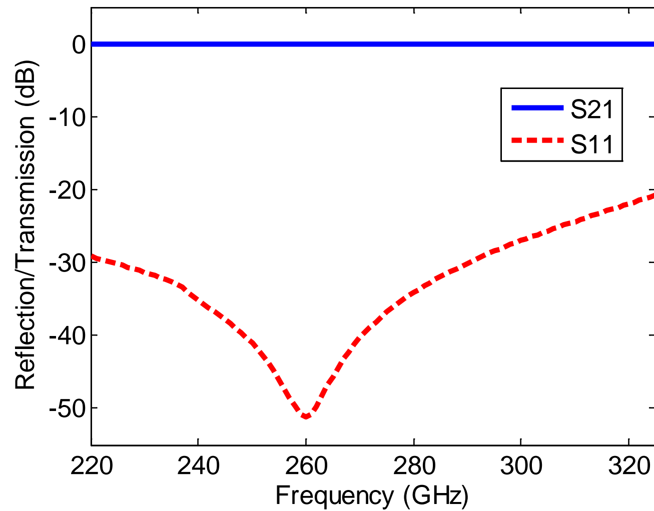

Figure 4.7 Performance of the choke connection with 20μm gap between the two surfaces

Grooves are milled using an electrical discharge machining (EDM) technique to fabricate the choke on the probe cross section. A thin single-strand metal wire, usually brass, is fed through the work piece, submerged in a tank of dielectric fluid, typically deionized water [82]. The fabricated choke is shown in Figure 4.8.

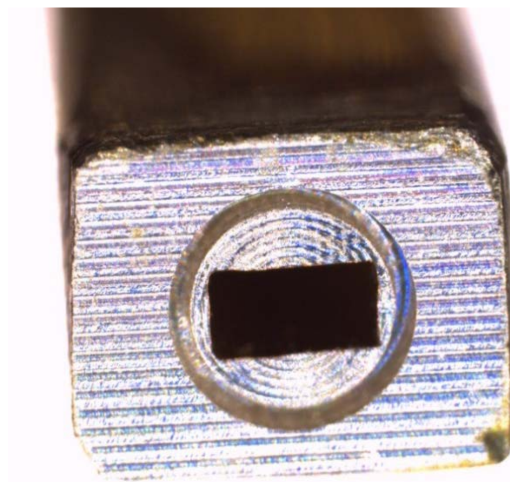

Figure 4.8 Choke milled on the cross-section of waveguide probe

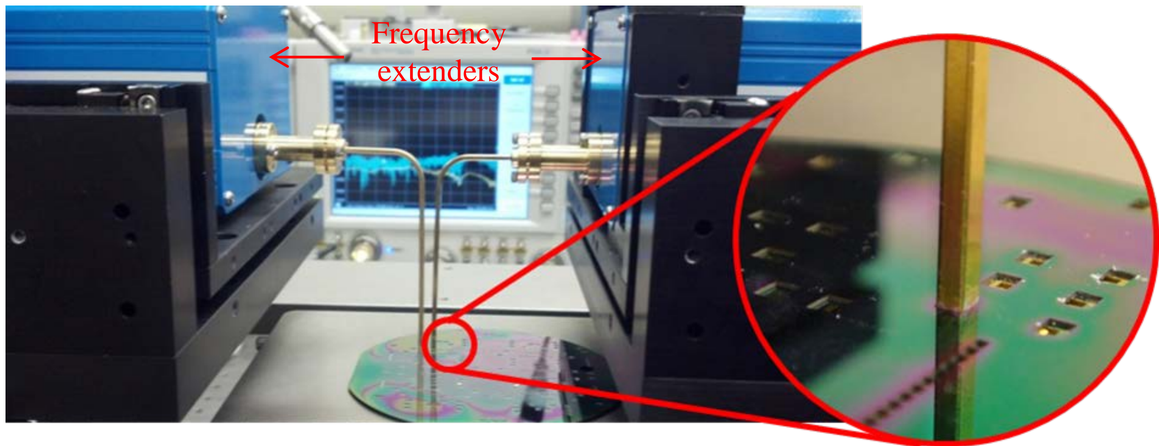

(a)

(b)

Figure 4.9 (a) The waveguide probe measurement setup (b) custom-made WR-3 waveguide probe

1.19.3 Measurement Setup

The measurement setup is shown in Figure 4.9. An Agilent N5245 4-port Performance Network Analyzer (PNA) is used along with OML MMW frequency extending modules to perform full 2-port S-parameter measurements at J-band. Two custom-made waveguide probes are connected to the OML frequency extenders. The two frequency extending modules are mounted on micropositioners to allow accurate positioning of the waveguide probes on the wafer. The probes are accurately positioned

over the waveguide opening on the wafer and brought in contact with the surface to perform S-parameter measurements.

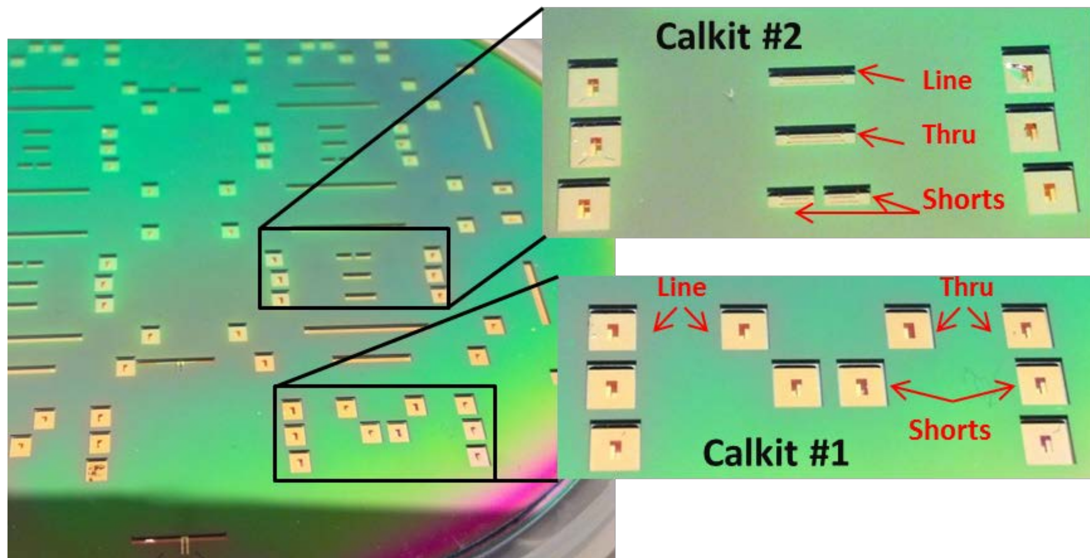

Figure 4.10 On-wafer waveguide calibration kits. The calibration kits includes three standards (shorts, line, and thru) to perform TRL calibration. Calibration kit #1 calibrates the system up to the on-wafer waveguides. Calibration kit #2 calibrates the system up to the CBCPW lines.

1.19.4 Measurement Results

To calibrate the system for characterization of the transition and CBCPW line, two sets of TRL calibration kits are fabricated on the wafer as shown in Figure 4.10. Calibration kit #1 which includes the E-plane transitions and calibrates the system up to the on-wafer waveguides is used for characterization of the transitions. Calibrated S-parameter measurement of a 1-cm long waveguide section is shown in Figure 4.11 (a). It is shown that the calibrated return loss is more than 20 dB over the entire band.

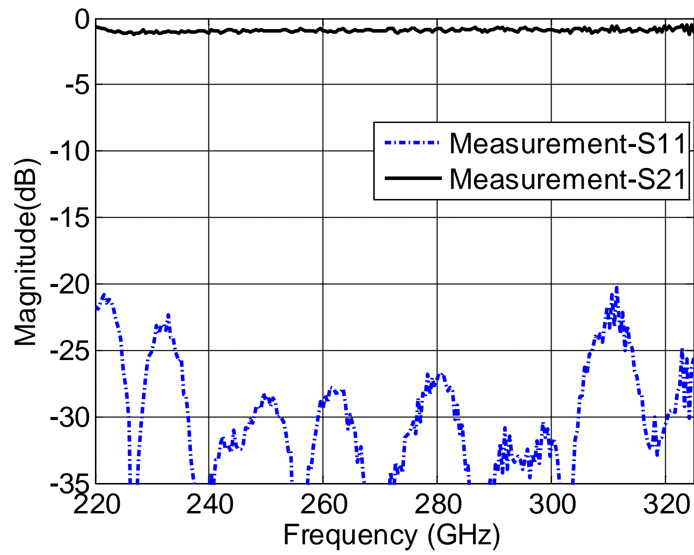

(a)

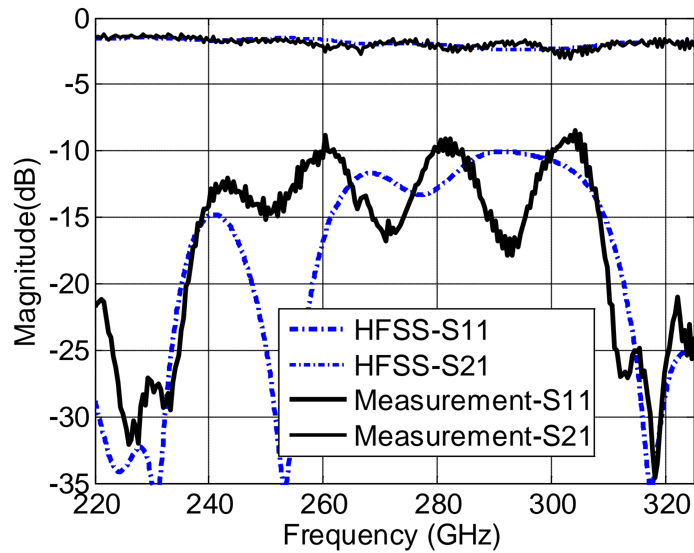

(b)

Figure 4.11 (a) Calibrated measurement of an on-wafer waveguide section (length=1cm) (b) Simulated and measured reflection and transmission coefficients of back-to-back CBCPW to rectangular waveguide transition

Calibrated S-parameter measurements of the back-to-back transition are presented in Figure 4.11 (b). The measured results show good agreement with the full-wave analysis

results. Calibration kit #2 which includes the back-to-back transitions and calibrates the system up to the CBCPW line is used for characterization of CBCPW lines. Measured attenuation of the fabricated CBCPW line is in good agreement with the simulated results (see Figure 4.12).

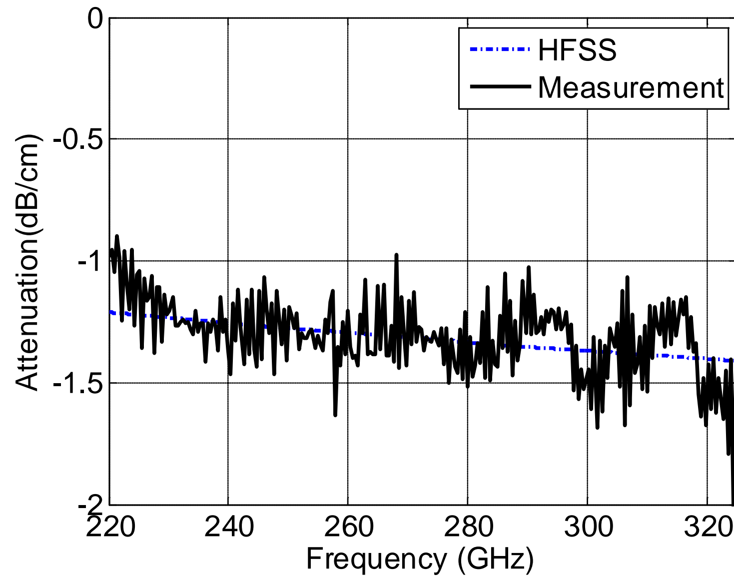

Figure 4.12 Simulated and measured attenuation of the CBCPW line

1.20 Chip Integration

As described in Section 2.4, a thru-wafer chip packaging structure is designed to enable integration of active chips with the radar front-end. The active chips are developed by BAE systems using 50 nm MHEMT Technology [83, 84]. The MMIC modules are implemented on a 55 μm thick Indium-Phosphide (InP) substrate.

Delay lines implemented on 55 μm thick InP substrate are acquired from BAE systems to test the performance of the chip integration structure, (Figure 4.13). The delay line chips are dropped into the openings from the backside of the wafer. The top side view

of the chip after insertion into the opening shows excellent alignment of the chip with on-wafer traces as shown in Figure 4.14. The measured performance of the chip transition is shown in Figure 4.15. The return loss of the transition is more than 14 dB and the insertion loss is about 2 dB in the 220-270 GHz band. The excess insertion loss compared to the simulations is mainly due to current microstrip line design on the chips which supports higher order modes. To further improve the current transition performance, BAE systems is modifying the design on their chips to the optimal design presented in Appendix A.

Figure 4.13 Delay lines implemented on 55 μm thick InP with the old launch pad design

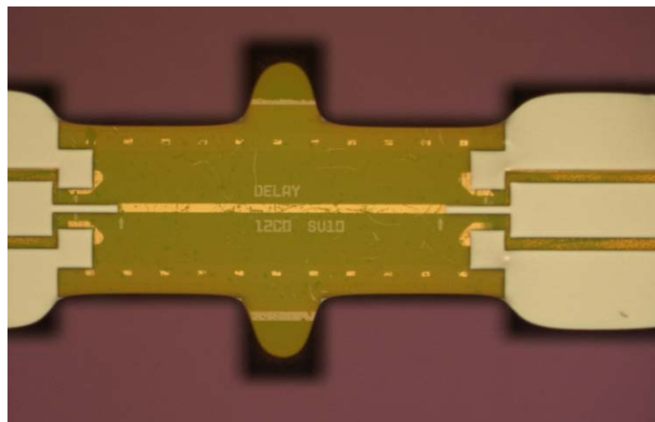

Figure 4.14 The top view of the thru-wafer transition with the after chip insertion. The launch pads on the chips are in perfect alignment with the on-wafer transition traces.

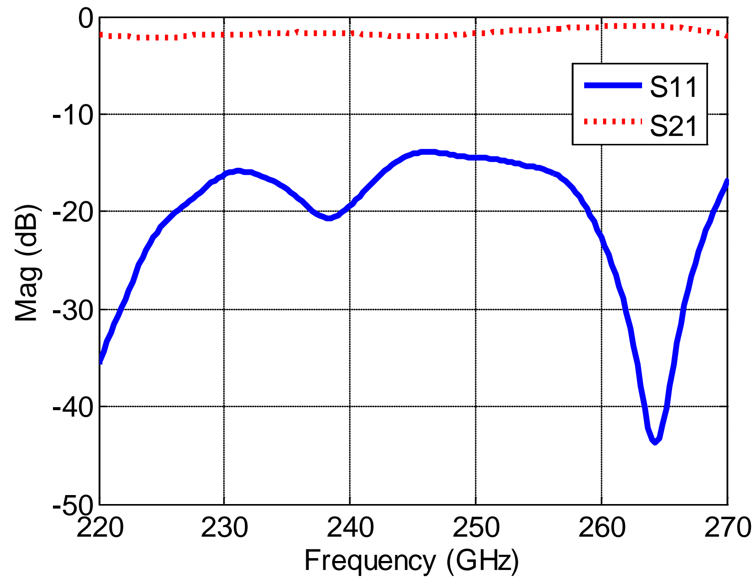

Figure 4.15 Insertion loss and return loss of the chip transition shown in Fig. 4.14

1.21 The Non-Contact S-Parameter Measurement Technique for Characterization of Multi-Port Components

Characterization of multi-port components, such as directional couplers, hybrids, power splitters, etc., using two-port measurement systems require independent measurements of pairs of ports one at a time while all the other ports are terminated with matched loads. Since matched loads are usually integrated with the device, identical devices must be fabricated with different ports terminated with matched loads in order to complete the S-parameter measurements [85, 86]. Thin-film resistors are typically used as on-wafer loads to terminate the desired ports. Performance of thin film resistors, however, degrade rapidly as the frequency is increased due to parasitic effects, thus limiting their application to frequencies below 60 GHz. Precision waveguide loads are required to

terminate the desired ports to characterize devices attached to test fixtures,. These loads are difficult to realize for sub-MMW and terahertz bands and cause the same errors mentioned for waveguide calibration [81].

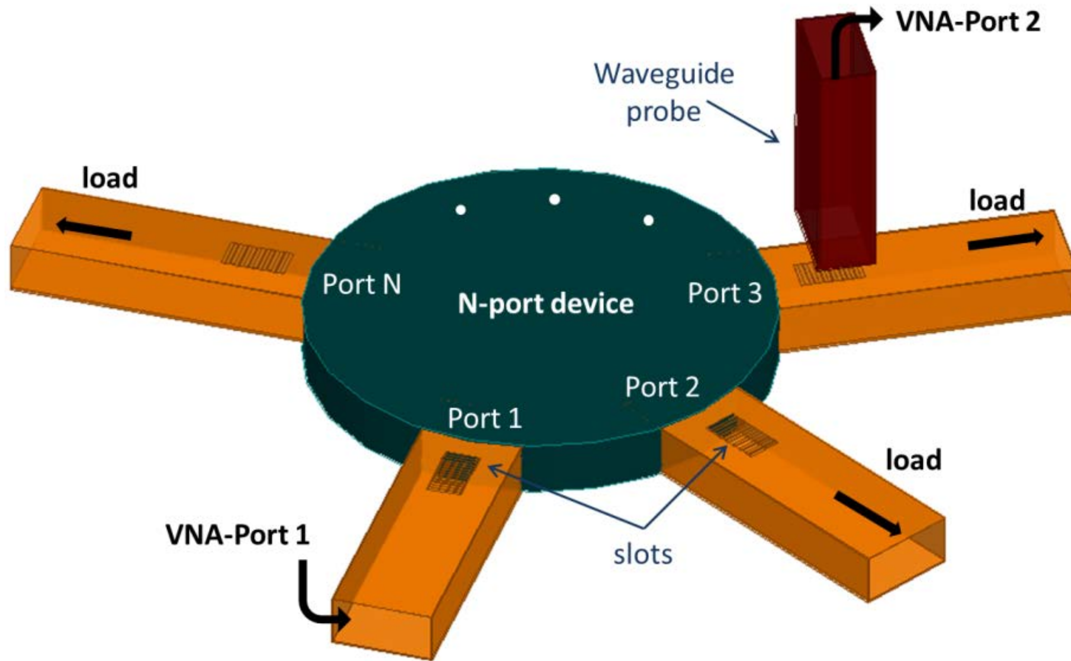

Figure 4.16 Schematic of the proposed multi-port S-parameter measurement technique using two-port measurement system

In this Section, a novel S-parameter measurement method for characterization of on-wafer multiport devices and components is developed to circumvent the aforementioned difficulties associated with high frequency device measurements. The proposed method requires a two-port vector network analyzer (VNA) with the ability to perform S-parameter measurements in the desired frequency band. The schematic of the proposed method is shown in Figure 4.16. The input port (port 1) of the multi-port device is fed with port 1 of the VNA. The input power at port 1 and the output power at the other ports of the multiport component are measured by port 2 of the VNA through a coupling

mechanism using an open-ended waveguide. Identical rectangular slots are fabricated over the micromachined waveguides to couple a small fraction of the input/output power at each port. A waveguide probe is used to measure the amplitude and phase of the coupled signal from the slots at all ports including port 1. All the output ports are terminated with on-wafer micromachined loads to avoid reflections. The S-parameters of the device can then be calculated using the measured signals collected by the waveguide probe.

1.21.1 Theory

The complete scattering matrix of the N-port device must be measured using a two-port VNA to characterize an N-port device. In the conventional method, *N(N-1)/2* device test configurations must be arranged with a 2-port VNA in order to fully characterize the scattering matrix. In each configuration, two ports of the device are connected to the VNA and the rest are terminated with matched loads. For symmetric devices (e.g. directional couplers), the device can be fully characterized by measuring a single column of the scattering matrix. This requires measuring $N-1$ different device configurations using the conventional method.

In our proposed technique, a single column of the scattering matrix of an N-port device can be retrieved based on N non-contact VNA transmission (S_{21}^{VNA}) measurements for a single device measurement configuration (see Figure 4.16) plus a reference non-contact measurement of the input (port 1) structure which is terminated with a matched load. The input port can be excited using any method (GSG probe, waveguide connection, etc.). This way the response of the excitation method (return loss and insertion loss of the input transition) can be removed from the S-parameter measurements.

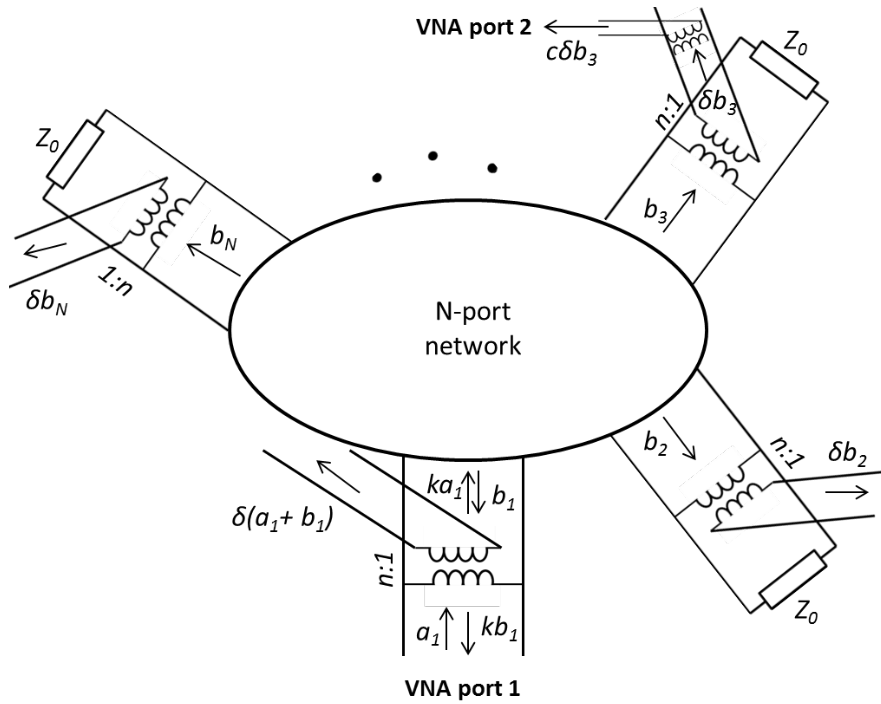

(a)

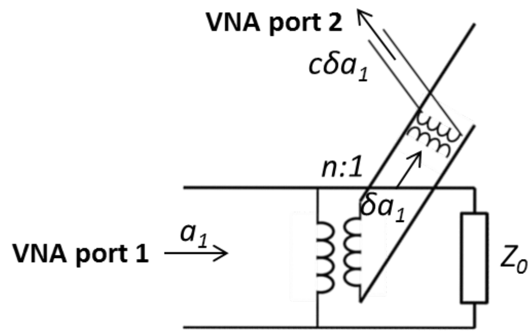

(b)

Figure 4.17 The circuit model of the proposed S-parameter measurement method (a) N-port device measurement configuration, (b) reference measurement configuration

The circuit model for the proposed N-port device measurement and the reference measurement are shown in Figure 4.17. As mention before, a number of small rectangular slots on the broad wall of micromachined waveguides are used as a coupling mechanism.

The rectangular slots over the waveguides at each port are modeled as transformers that couple a very small portion of energy to the free space ($n \gg 1,\ \delta \ll 1$). The coupled signal is proportional to the total signal in the waveguide at the slot location. It is important that these slots be designed in such a way as to minimize the reflection in the waveguide (<-20dB). The outputs of the other ports are terminated with matched load Z_0 to ensure:

$$a_m = 0, \qquad m \neq 1 \tag{4.3}$$

The measured signal at port 2 of the VNA is the coupled signal from the slots to a near-field waveguide probe at an exact height and lateral position with respect to the slots at each port. Thus the measured S_{21} of the network analyzer for each port of the N-port device can be written as:

$$S_{21,1}^{VNA} = \frac{c\delta(a_1 + b_1)}{a_1} \tag{4.4}$$

$$S_{21,1}^{VNA} = \frac{c\delta b_m}{a_1}, \qquad m \neq 1 \tag{4.5}$$

In the measurement configuration shown in Figure 4.17 (b), the input port is terminated with matched load Z_0 and hence:

$$b_1 = 0 \tag{4.6}$$

for the reference waveguide transition. Since the excitation method and the position of the slots are identical to the input port of the N-port device, the measured S_{21} of the reference waveguide transition is equal to:

$$S_{21,ref}^{VNA} = \frac{c\delta a_1}{a_1} \tag{4.7}$$

The coupling coefficient $c\delta$ is a complex number which is equal for all the measurements since the slots positions are at the reference planes (designated port location) and the probe position are kept identical with respect to the slots.

The input power to the device is the input power from port 1 of the VNA minus the power radiated by the slot ($ka_1, k \cong 1$). Hence, the S-parameters of the device are:

$$S_{m1}^{D} = \frac{b_m}{ka_1}, \qquad m = 1, \ldots, N \tag{4.8}$$

From (4.4) and (4.7), the return loss of the device is computed from:

$$S_{11}^{D} = \frac{b_1}{ka_1} = \frac{1}{k}\frac{S_{21,1}^{VNA} - S_{21,ref}^{VNA}}{S_{21,ref}^{VNA}} \tag{4.9}$$

And from (4.5) and (4.7), the rest of the S_{m1} parameters of the device are found to be:

$$S_{m1}^{D} = \frac{b_m}{ka_1} = \frac{1}{k}\frac{S_{21,m}^{VNA}}{S_{21,ref}^{VNA}} \tag{4.10}$$

As indicated by (4.9) and (4.10), the S-parameters of the device can be derived from the VNA transmission measurements and parameter k. It will be shown in Section III that the coupled power to the coupling slots is very small over most of the full band ($k \cong 1$). For a better estimation of the S-parameters, the simulated value of k will be used in (4.9) and (4.10).

For a non-symmetric N-port device, only *N-1* other device configurations are required where the nth port is connected to the input of the VNA and the rest of the ports are terminated with matched loads. This is by a factor *(N-1)/2* smaller than the conventional method that requires *N(N-1)/2* device configuration measurements.

1.21.2 Coupling Slot Array Design

Here the design and analysis of the slot array and the probe measurement configuration for J-band is presented. It is known that electromagnetic energy may be coupled to free space by creating small apertures at suitable location on a waveguide.

However, the insertion of slot apertures also creates reflection in the waveguide. This reflection can cause error in the calculations presented in Section 4.5.1. To solve this problem, an array of small slots is designed as shown in Figure 4.18 (a). The size of the array is optimized to achieve maximum reflection cancellation from individual apertures and minimize the total reflected power. The optimized coupling slot array is composed of 14 closely spaced small slots occupying an area of 555μm × 300μm (0.5λ × 0.27λ at 272 GHz). Full-wave analysis of the optimized design shows more than 20 dB return loss over the entire J-band. The transmitted power through the waveguide (k in Section 4.5.1) is more than 99% of the input power at 220 GHz and drops to 85% at 325 GHz.

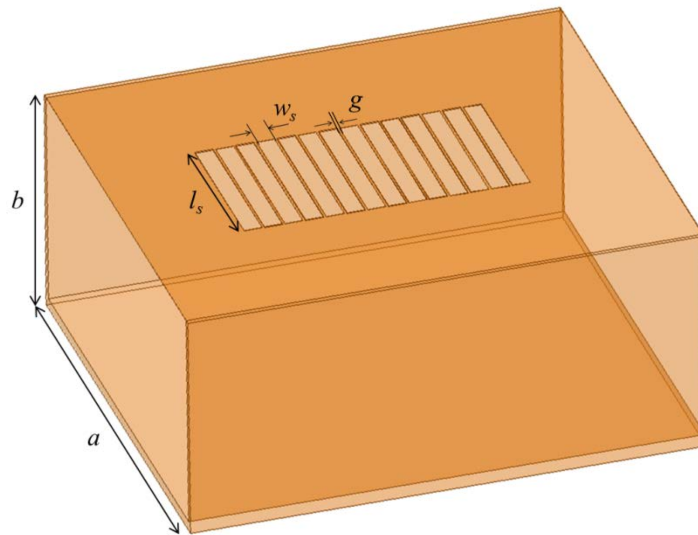

(a)

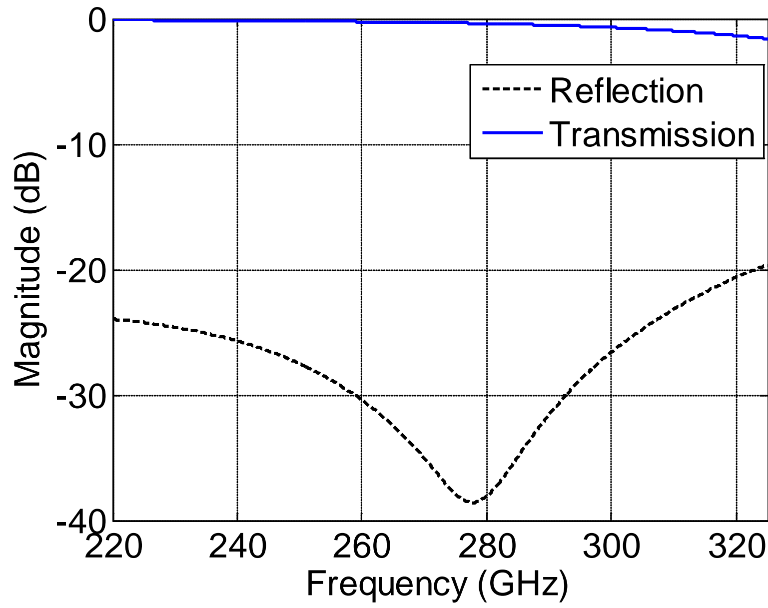

(b)

Figure 4.18 (a) Schematic of the optimized 14-slot array (a = 860µm, b = 430µm, l_s = 300µm, w_s = 35µm, g=5µm), (b) Reflection and transmission of the waveguide section with slots

The simulated coupled power from the slot array to free space as received by a WR-3 open-ended waveguide probe is shown in Figure 4.19. The probe is positioned at a short vertical distance (300µm) over the slot array. The probe position is adjusted precisely in the horizontal plane to maximize the coupled power to the probe. Figure 4.19 (b) shows the reflected, transmitted and coupled power versus the position of the waveguide probe in the horizontal plane with respect to the center of the slot array. The return loss in the waveguide is more than 25 dB and the transmission into the waveguide varies by less than 0.1 dB for all probe positions in the 2×2 mm^2 area around the slot array. This ensures that the presence of the probe does not perturb the measured characteristics of the DUT. The maximum coupling (S31) is achieved when the probe is located at (200µm, 0) with a power

coupling factor of about -12 dB. The coupling drops rapidly in all direction as the probe moves away from the maximum coupling position. The coupling drops down to below -25 dB when the probe is outside 1-mm radius of the slot array. This ensures that, if the slot arrays are far enough from each other, the radiated power from the other ports do not couple to the probe over a given port and cause measurement errors.

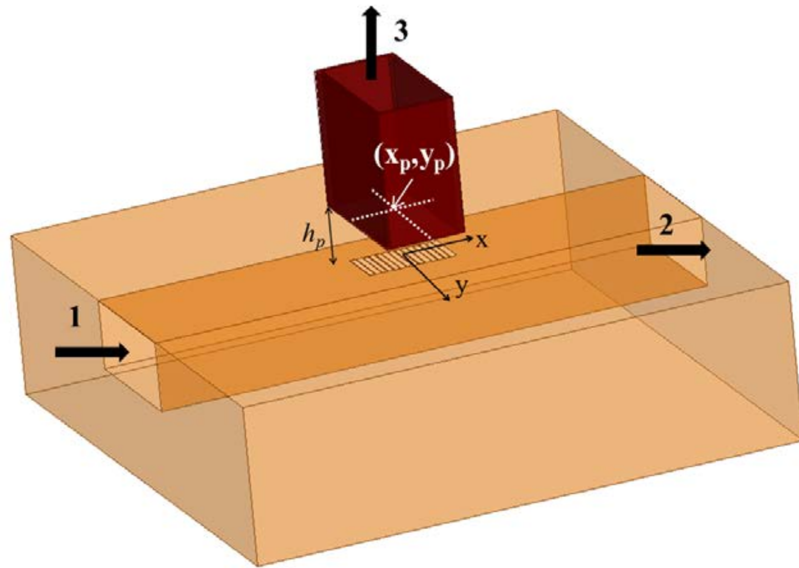

(a)

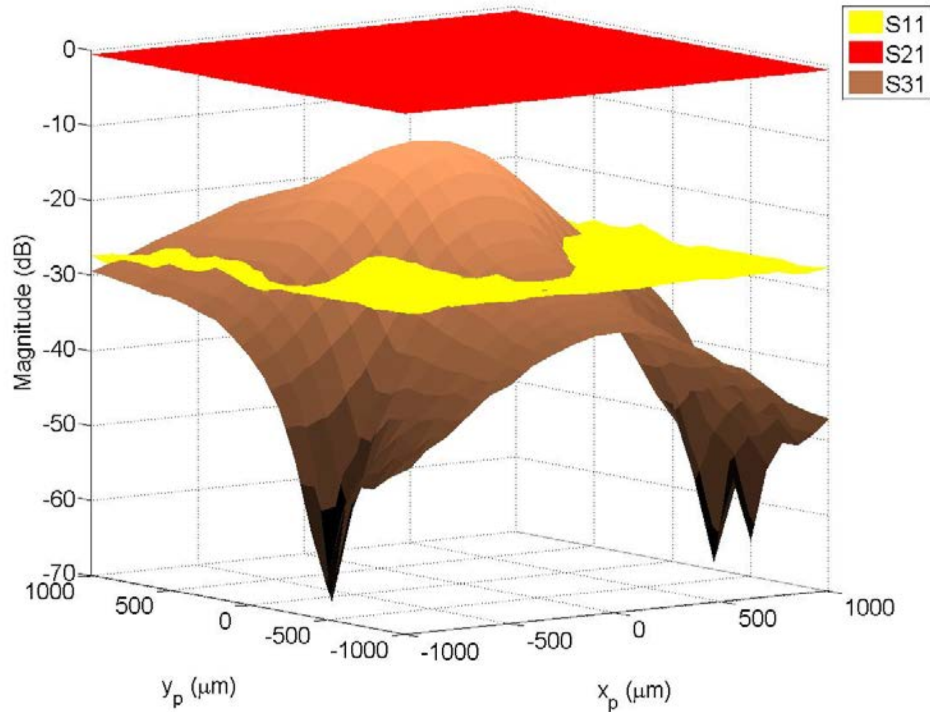

(b)

Figure 4.19 (a) The optimized 14-slot array schematic, (b) Reflection (S11), transmission (S21), and the coupled power to waveguide probe (S31) versus the position of the waveguide probe with respect to center of the array (x_p,y_p) (h_p=300μm, f=300 GHz)

1.21.3 Match Load Design

The output ports of the multi-port device must be terminated with good loads having a very low reflection in order for the proposed measurement approach, as described in Section 4.5.1, to work properly. A radiating load is the easiest to implement in terms of bandwidth, lack of parasitics, and compatibility to micro-fabrication. Here, a traveling wave slot array over the broad-wall of the waveguide is considered for terminating the ports. To achieve a broadband response over the entire J-band, the array is implemented in multiple sections. The first section is an array of small slots that shows a good return

loss at the higher end of the band. The length of the slots (l_s) is increased gradually to increase the radiated power by the slots at lower frequencies while maintaining a high return loss over the band. Finally, the last section is composed of two very large slots which radiate the remaining power in the waveguide. The dimensions of the slots and length of the array are optimized to achieve the maximum return loss for the minimum length of the array over the full band. Full-wave analysis shows the optimized load has more than 22 dB return loss over the entire J-band as shown in Figure 4.20. In this implementation the length of the antenna is 11.1mm.

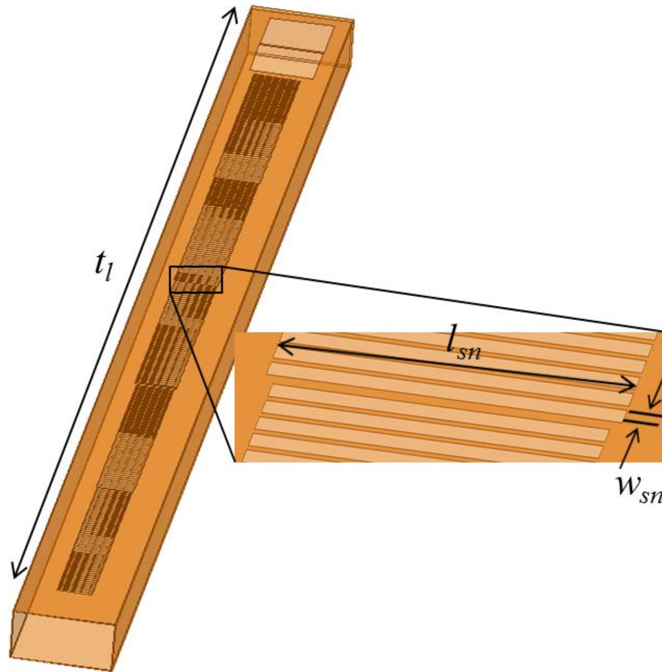

(a)

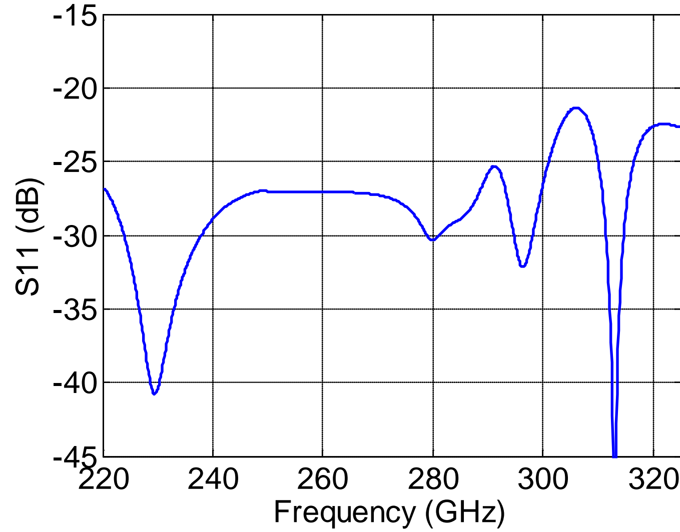

(b)

Figure 4.20 (a) The matching load based on slot array over micromachined waveguides (optimized dimensions: t_l=11.1 mm, l_{s1}=300 µm, l_{s2}=320 µm, l_{s3}=360 µm, l_{s4}=380 µm, l_{s5}=400 µm, l_{s6}=550 µm, w_{s1}=w_{s2}= w_{s3}= w_{s4}= w_{s5}=30 µm, w_{s6}=500 µm), (b) simulated return loss of the optimized load

1.21.4 Coupler Measurements

To characterize the couplers designed in Section 2.5, using the proposed measurement method, the output ports of the couplers (through, coupled, isolated) are terminated with the matched load described in Section 4.5.3. The radiating slots on each port are separated by more than 5 mm to ensure little coupling between the coupling slots and the radiating loads. The input port is connected to an E-plane transition to enable excitation of this port using the waveguide probe described in Section 4.3. Figure 4.21 shows the schematic of the test configuration. It is noted that the input structure for the coupler and the reference waveguide are identical to meet the requirement stated in Section 4.5.1.

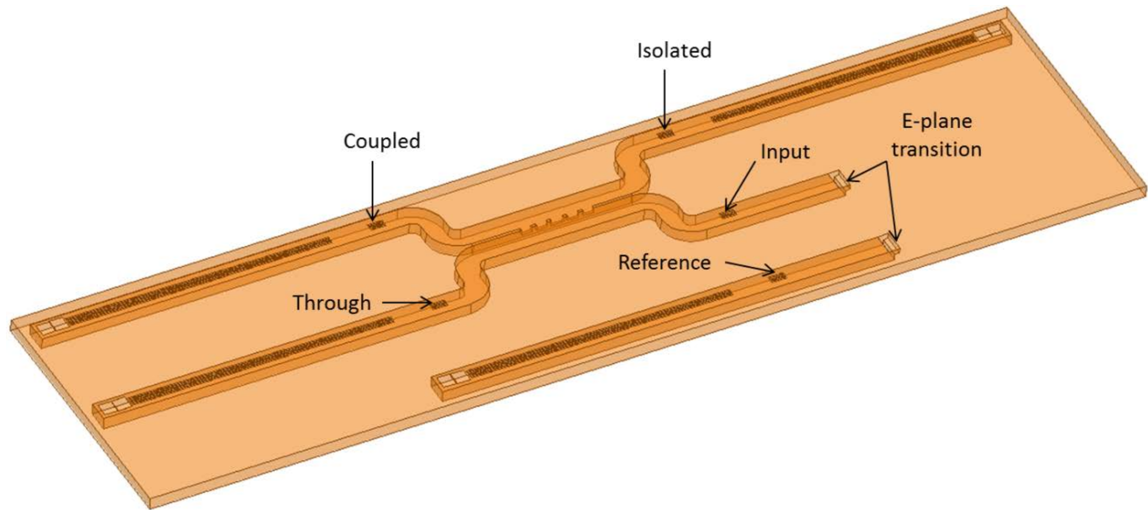

Figure 4.21 Schematic of the test configuration for coupler characterization

The measurement setup is shown in Figure 4.22. The two-port J-band measurement system described in 4.3.3 is utilized to perform full two-port S-parameters. One of the custom-made waveguide probes is connected to the waveguide port of one of the frequency extenders (port 1) to excite the device through an E-plane transition. Another open-ended waveguide probe is connected to the port of the other frequency extender to measure the signal from the coupling slots. The open end of this probe is tapered to minimize the reflections at the probe cross section. The location of this probe over the slot arrays is obtained by adjusting its position until a maximum signal is measured by the network analyzer.

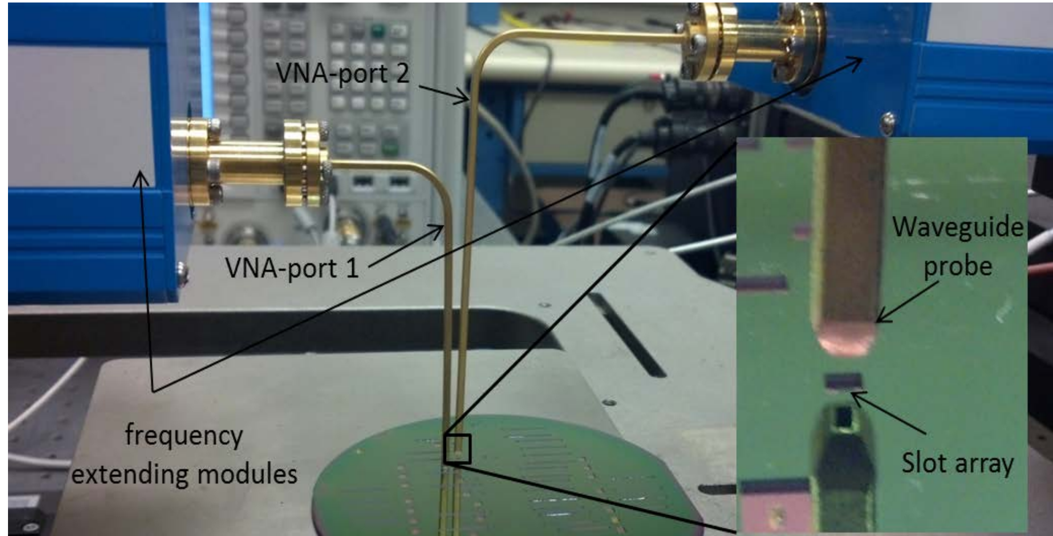

Figure 4.22 The measurement setup; the signal coupled from the waveguide through the slot array is measured with the near-field probe. The frequency extenders are mounted on micropositioners to enable manipulation of the probe positions in three dirctions.

The measured and simulated characteristics of the three fabricated couplers are shown in Figure 4.23 (a)-(c). The measured return losses of the couplers are shown in Figure 4.24. Repeating the experiment multiple times, it is noticed that the measurements are highly reliable and repeatable.

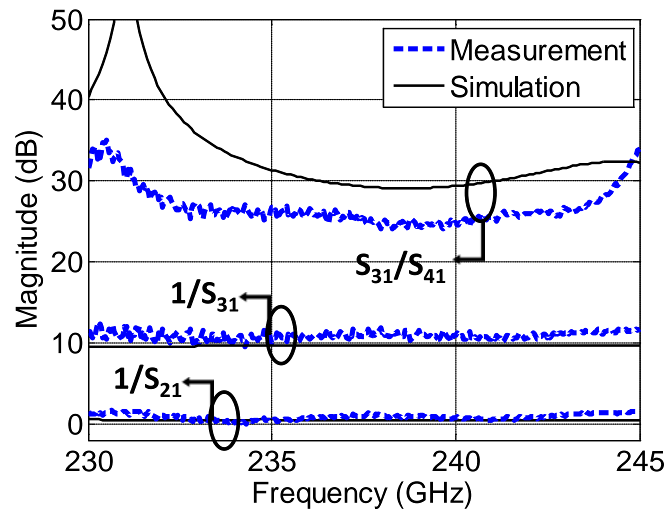

(a)

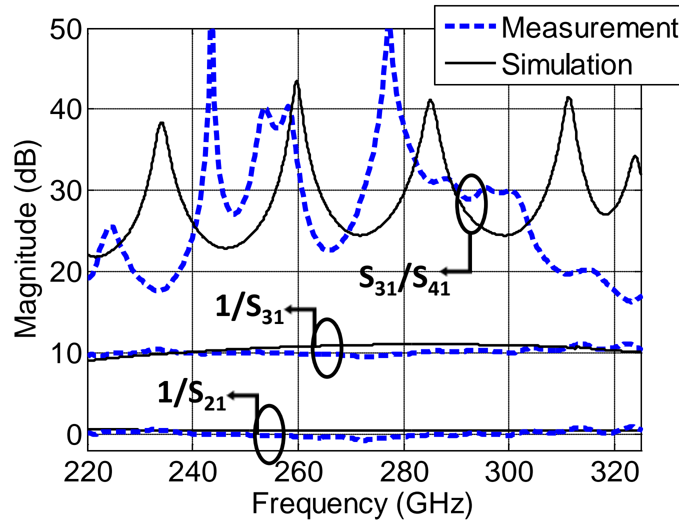

(b)

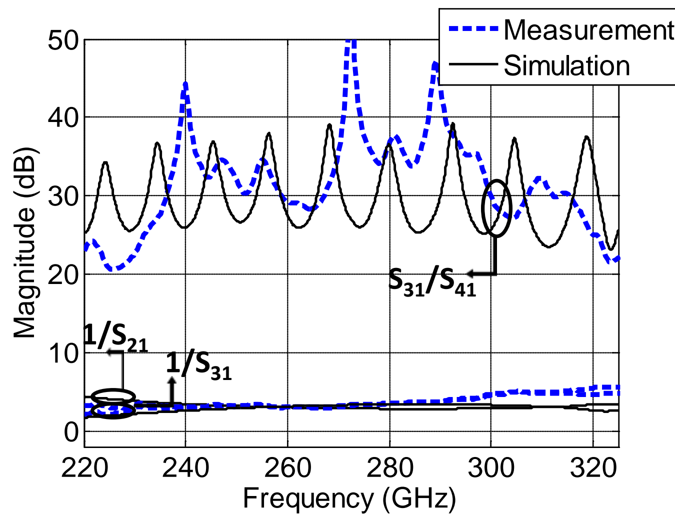

(c)

Figure 4.23 Through ($1/S_{21}$), coupling ($1/S_{31}$), and directivity (S_{31}/S_{41}) of the directional couplers: (a) 10-dB coupler (230-245 GHz), (b) 10-dB coupler (220-325 GHz), (c) 3-dB coupler (220-325 GHz)

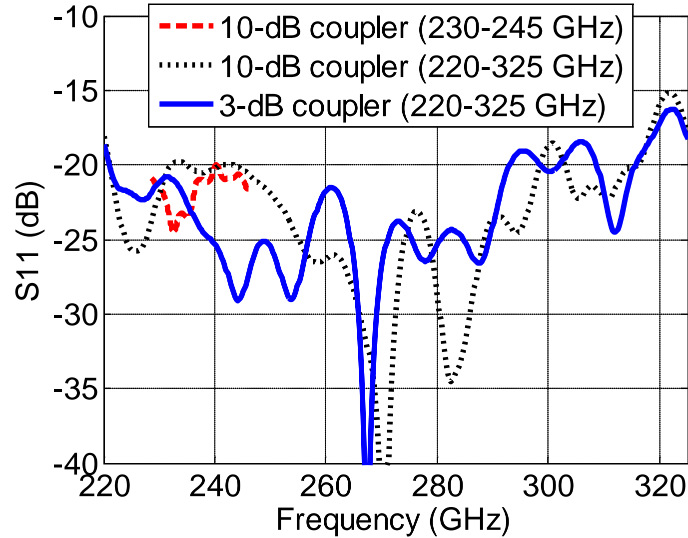

Figure 4.24 Return loss of the directional couplers

1.21.5 Sensitivity Analysis

The accuracy and repeatability of the measurements are subject to two sources of error; 1) VNA measurement uncertainties, 2) probe positioning error. The uncertainties in VNA measurements due to thermal noise, drift of the local oscillators, temperature stability of active components, phase stability of the cables connected to the frequency extenders, etc., cause error in the S-parameter measurements. These uncertainties have been studied before [87] and are present in any measurement technique that utilizes VNAs for measurements. The accurate lateral position of the probe with respect to the slots can cause error by changing the coupling factor ($c\delta$) from one measurement to other. The vertical distance from the probe to the slots does not affect the S-parameter calculation since it is kept the same for all the measurements.

We have performed 6 measurements of a single coupler to study the reparability of the proposed method. The input port connection and the waveguide probe are repositioned

each time to capture the waveguide positioning error. The measured magnitude of the S-parameters of the 10-dB coupler is shown in Figure 4.26 (a). The coupled and thru signal (S31 and S21) have a variance of about 0.2 dB around the mean. The variations in return loss and isolation (S11 and S41) are larger since these signals are weak and dominated by the thermal noise. The phase difference between the coupled and thru signal is shown in Figure 4.26 (b). The measured phase differences are within ±5˚ of the expected 90˚ value. The normalized standard deviations of the coupled and thru are shown in Figure 4.26.

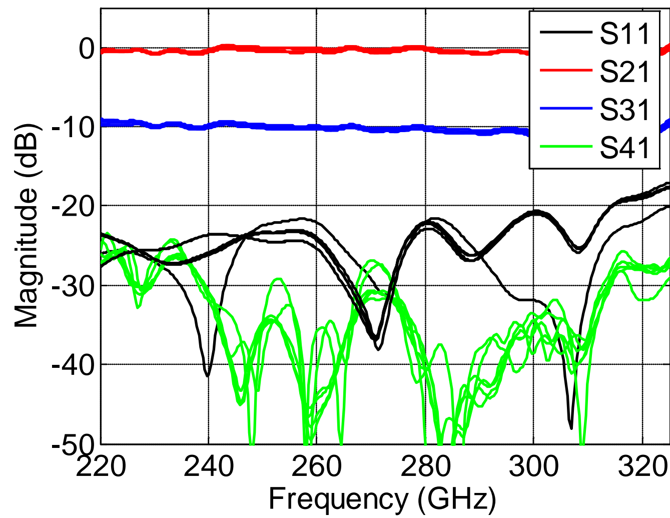

(a)

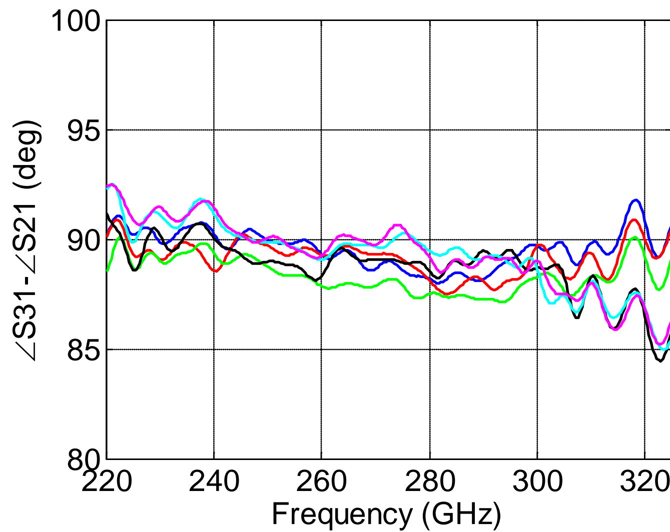

(b)

Figure 4.25 (a) Repeated measurement of a 10-dB coupler, (b) the phase difference between the coupled signal and thru signal

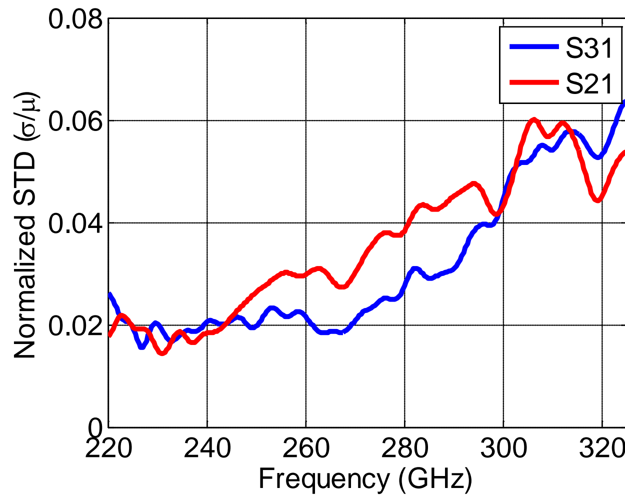

Figure 4.26 Normalized standard deviation of repeated measurements of S21 and S31

1.22 Summary

In this chapter, new S-parameter measurement techniques were developed to enable accurate and repeatable characterization of on-wafer components at MMW and higher frequency bands. The current measurement techniques and their limitations at high frequency bands were presented. To overcome the difficulties associated with these techniques, a new waveguide probe measurement technique was proposed. An E-plane transition was micromachined on the wafer to enable measurement of the on-wafer components using this technique. A waveguide choke was machined on the probe end to ensure perfect electrical connection at the contact point. The micromachined waveguides,

CBCPW line, and waveguide to CBCPW transition were measured using this technique. A non-contact S-parameter measurement method for characterization of on-wafer multi-port devices using a two-port VNA is presented to characterize the fabricated directional couplers. The proposed method is based on sampling the magnitude and phase of the signal at each port. In this method, a small fraction of the signal at each port is coupled to free space using an array of reflection canceling slots and measured using an open-ended waveguide probe. It is shown that the S-parameters of the device under test can be calculated using the measured signals at each port. A broadband waveguide slot array antenna with good return loss is utilized as the matched load to terminate all ports except the input port of the device. The measured results are in good agreement with the simulations which indicates the accuracy of the proposed measurement method. It is shown that the proposed S-parameter measurement approach for sub-MMW is accurate, repeatable, far easier and faster than the conventional method.

CHAPTER 5
MMW IMAGE-REJECTION SPATIAL FILTER

1.23 Introduction

MMW and sub-MMW radar front-ends typically have a harmonic mixer to upconvert a modulated IF signal to the desired RF transmit frequency. For example, the block diagram and output spectrum of the Y-band instrumentation radar which is utilized for phenomenology study in Chapter 6, is shown in Figure 5.1.

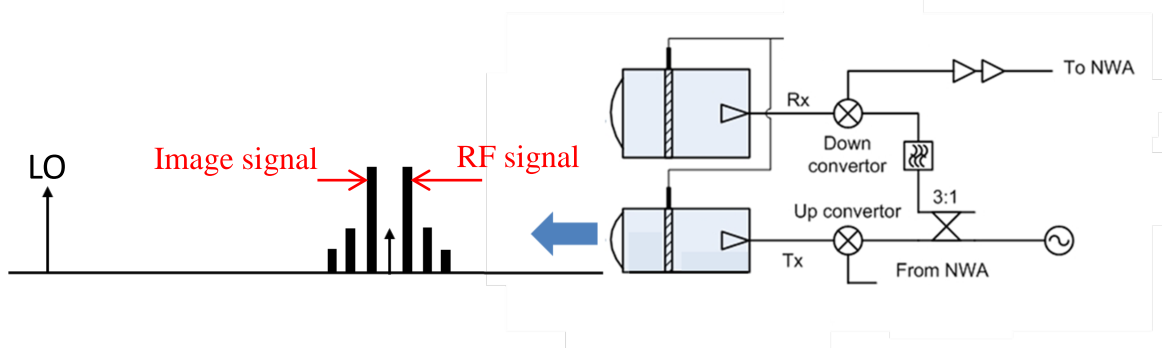

Figure 5.1 The spectral output of the Y-band instrumentation radar system

The Harmonic mixer nonlinear intermodulation creates different mixing products of LO and IF signals. Among these signals, the image signal has the highest amplitude and is downconverted into the same band as the RF signal. Mixture of these signals in the receiver can cause a significant error in radar measurements. To avoid measurement errors, a bandpass filter is required to provide high isolation between adjacent bands of the RF signal and its image.

Waveguide and planar MMIC filters have been traditionally used in communication and radar systems to achieve band isolation between different channels [88, 89]. To achieve

channel selection between adjacent bands, high order filters are required to achieve the necessary suppression of the undesired sideband. The design and realization of multipole filters at high MMW and sub-MMW frequencies is very difficult and leads to higher than desired insertion loss. Planar MMIC filters, on the other hand, are easy to fabricate but their loss is prohibitively high for most radar and communication applications at these high frequencies. To overcome the limitations associated with waveguide and MMIC filters, frequency selective surfaces are considered to perform spatial filtering on the transmitted EM wave.

1.23.1 Frequency Selective Surfaces (FSS)

Frequency selective surface (FSS) structures have been utilized in MMW and sub-MMW remote sensing instruments to provide spatial filtering [90-92]. A frequency selective surface is usually made up of planar metallic patterns on a dielectric substrate. The metallic pattern usually forms a 2D periodic array of resonant unit cells which has a certain frequency response for the incident electromagnetic wave.

1.23.1.1 Resonant-element FSS

The common feature among traditional resonant FSS structures is that the size of the resonant elements and their spacing are comparable to the wavelength at the operating frequency. Multilayer resonant-element FSSs are reported with low insertion losses (as low as 0.6 dB) and 30 dB isolation in adjacent bands with a band separation of 1:1.07 [90, 91] (Figure 5.2).

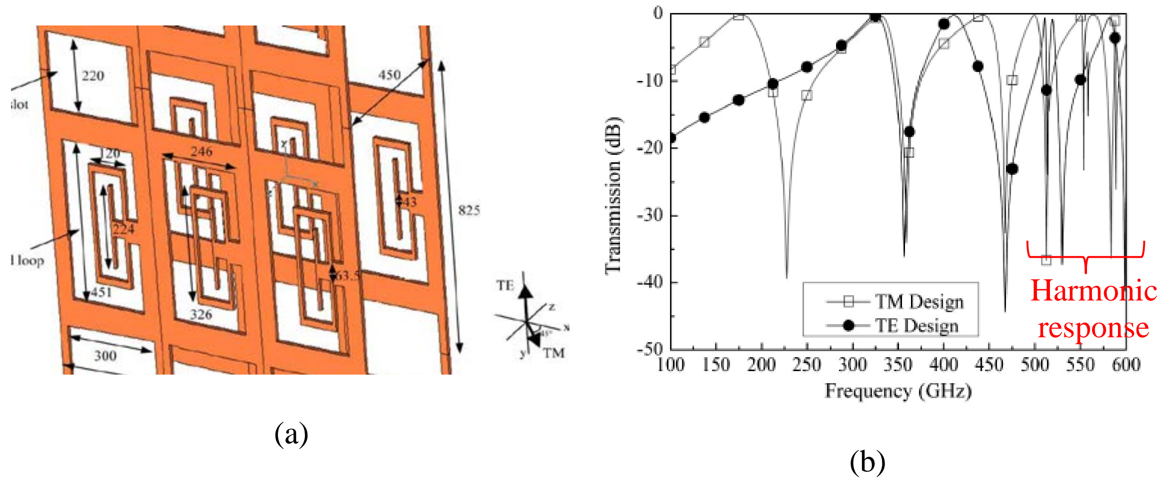

Figure 5.2 An image-reject resonant-element FSS (a) Geometry, (b) Transmission response at 45˚ incidence [91]

The frequency response of these structures is the result of mutual interactions of many adjacent unit cells and energy coupling of many slowly decaying evanescent Bragg modes. Hence, in order to observe the desired frequency response, the surface must include a large number of resonant elements and be illuminated by a planar phase front at a particular designed angle of incidence (i.e. 45˚ in Figure 5.2 (b)). This requires a large number of unit cells in the periodic array to create the desired frequency response. This needs a large screen size which causes limitations in applications where incident EM wave does not have uniform phase front. In addition, in radar applications, the FSS structure needs to be embedded inside the transmitter antenna which does not allow large screen sizes. Another limitation of resonant-element FSS is the harmonic response, as shown in Figure 5.2 (b), due to presence of higher order Bragg modes. To address this problem, a new class of frequency selective surfaces called miniaturized-element frequency selective surfaces (MEFSS) takes a different approach toward the design of unit cells.

1.23.1.2 Miniaturized-element FSS (MEFSS)

For certain applications FSS structures with relatively small electrical dimensions that are less sensitive to the incidence angle and can operate with non-planar phase fronts are highly desirable. A new class of FSSs called miniaturized-element FSSs (MEFSS) was introduced in [93] which incorporates these characteristics.

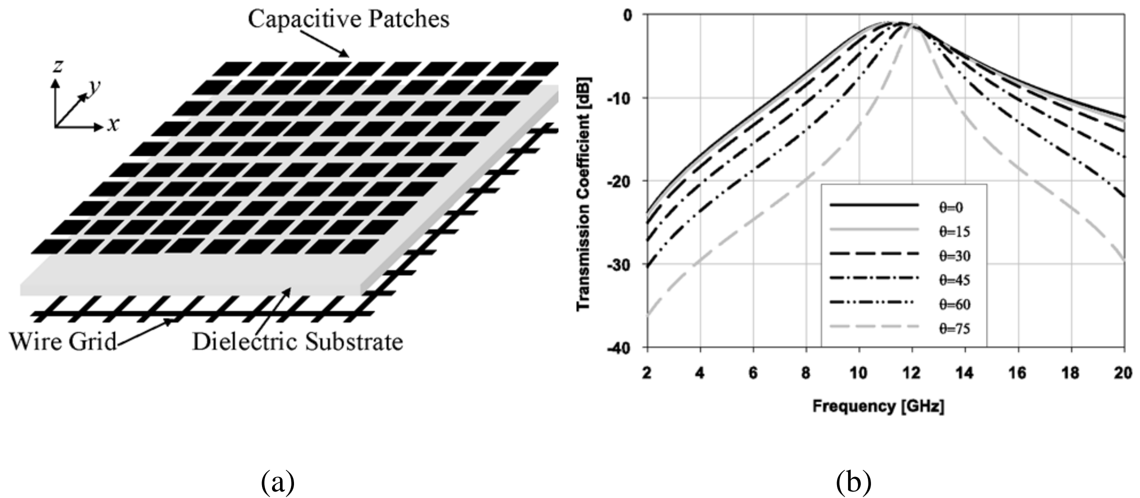

Figure 5.3 One pole bandpass MEFSS (a) Geometry, (b) Transmission response at different incidences [93]

The MEFSSs consist of a multilayer periodic array of metallic structures with dimensions that are much smaller than the wavelength at the operating frequency. This design allows for localization of bandpass characteristics to a small area on the surface, which allows flexible spatial filtering for an arbitrary wave phase front. Another advantage of the miniaturized-element design lies in the fact that the interaction of the surface and incident plane wave is predominantly in the TEM mode. As a result, higher order Bragg modes are suppressed, and harmonic responses are eliminated. In addition, the interaction of these MEFSS structures with an incident electromagnetic wave can be modeled as

lumped inductive and capacitive elements. This allows for design and tuning of MEFSS structures with arbitrary frequency responses based on their equivalent circuit model. In recent years, numerous variations of the miniaturized-element FSSs have been reported with operating frequencies up to 26 GHz [94, 95]. Single and multilayer multipole MEFSSs are fabricated using standard printed circuit board (PCB) technology at these frequency bands.

In this chapter, development of image-rejection band pass filters based on miniaturized-element frequency selective surfaces for application in MMW radar systems is presented. The work is motivated by the need for a high isolation between upper-side band (UPS) and lower-side band (LSB) signals present in the output spectrum of the Y-band instrumentation radar described in Chapter 6. The filter objective is to provide minimum insertion loss in the 221-223 GHz band and more than 25 dB signal suppression in the 205-207 GHz band. In addition, the spatial filter needs to be placed at a small distance from the radar feed antenna where we have a spherical phase front. A new MEFSS consisting of arrays of patch and I-shaped wires [96], as shown in Figure 5.4, is proposed to meet the required filtering characteristics for a vertically polarized incident wave. In this design, metallic elements are supported on a thin membrane sheet. The circuit design for image-rejection filters is presented in Section 5.2. In Section 5.3, the design procedure based on the equivalent circuit model is described and a full-wave numerical analysis is performed to verify the model accuracy. In Section 5.4, sources of loss have been analyzed to improve the insertion loss and the out of band rejection of the MEFSS. It will be shown that the transmission response of the proposed FSS has small dependency on the angle of incidence near the normal direction. Section 5.6 describes the MEFSS fabrication process

using a microfabrication technique. In Section 5.7, the experimental response of the fabricated prototype is presented using a free-space MMW measurement setup. Finally, a summary of the chapter is presented in Section 5.8.

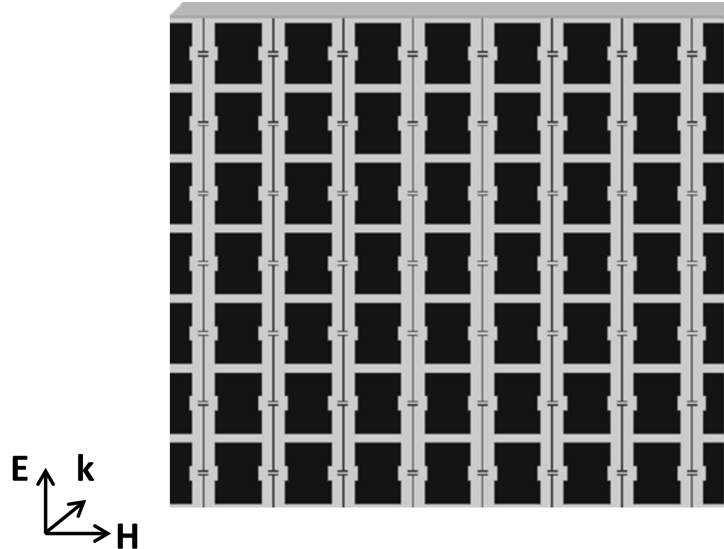

Figure 5.4 The proposed single face, membrane supported, MEFSS illuminated by a vertically polarized plane wave.

1.24 Image-Rejection Filter Circuit Design

The miniaturized-element frequency-selective surface parametric study begins with development a circuit model to describe the frequency behavior of the structure qualitatively. A circuit model is highly desirable at the design stage to quickly predict the response of the structure with some level of accuracy.

To achieve the desired filtering response using a simple structure with a low insertion loss, a single pole filter with an adjacent transmission zero is considered. This simple filtering response can be obtained from the circuit model shown in Figure 5.5.

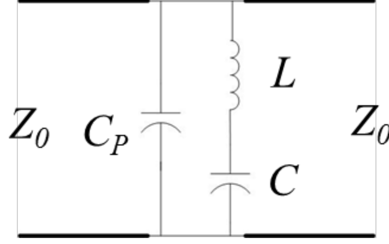

Figure 5.5 Circuit model for one pole bandpass filter with adjacent transmission zero

As can be noted in the circuit above, there is no coupling between the two parallel branches. The loop element (series LC branch) resonant frequency is:

$$\omega_{zt} = \frac{1}{\sqrt{LC}} \tag{5.1}$$

The pole frequency can be tuned by changing the patch size while maintaining the same transmission zero frequency as:

$$\omega_{bp} = \frac{1}{\sqrt{L(C + C_p)}} \tag{5.2}$$

It can be noted that the pole frequency is always higher than the transmission zero which is desired in many applications. The ratio is only a function of the ratio of the capacitors as:

$$\frac{\omega_{bp}}{\omega_{zt}} = \sqrt{1 + \frac{C_p}{C}} \tag{5.3}$$

The image-rejection response based on the above circuit model can be achieved through various MEFSS configurations. In Appendix C, a patch-loop MEFSS filter is proposed for incorporation in a 26 GHz UWB rangefinder radar. The spatial filter has a passband at 26 GHz and a transmission zero at 13 GHz. However, the patch-loop configuration has low quality factor at higher frequencies. In the following section, a novel

MEFSS configuration is proposed and designed to achieve low insertion loss in the passband and high rejection in the stopband for the Y-band instrumentation radar.

1.25 The Patch-Wire MEFSS

The circuit described in Section 5.2 can easily be realized in terms of a MEFSS structure. The configuration of such a MEFSS is shown in Figure 5.6.

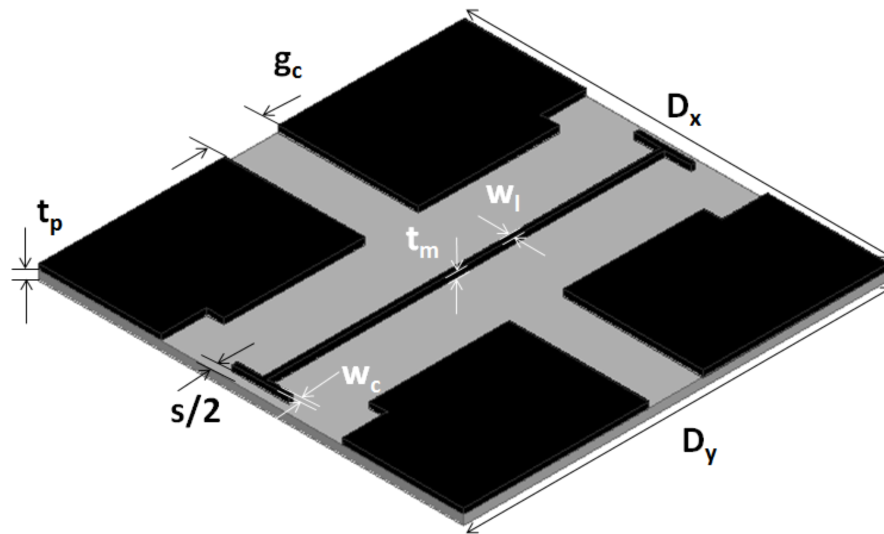

Figure 5.6 A unit cell of the MEFSS. The optimized dimensions are: $D_x = D_y = 470\mu m$, $g_c = 60\mu m$, $s = 20\mu m$, $t_m = 7\mu m$, $w_l = 5.7\mu m$, $w_c = 5\mu m$, $t_p = 10\mu m$.

The I-shaped elements interact with a V-polarized wave and behave as a series *L-C* branch. The inductance is a function of the length, width, and thickness (D_y, w_l, t_m) of the wire section, while the capacitance is mainly affected by the gap between two adjacent caps (s). The spacing between the I-shaped elements and patches can affect the inductance of the I-shaped elements if it becomes small enough. Basically the inductance of the I-shaped elements decreases as the metallic patch gets too close because it suppresses the circulating magnetic field around the wire. The patch array is modeled by a capacitor which

is in parallel with the *L*-*C* branch. The patch capacitor value, C_p, is a function of the gap between adjacent elements (g_c) and the dielectric constant of the supporting membrane.

At high frequencies, there is a small inductance associated with the patch elements which is modeled as an inductor, L_p, in series with C_p. This creates a second zero associated with the L_p-C_p branch which occurs at a much higher frequency compared to the other two resonant frequencies. The conductor loss in the wire elements is modeled as series resistanse within the *L*-*C* branch. The equivalent circuit model for the patch-wire MEFSS is shown in Figure 5.7.

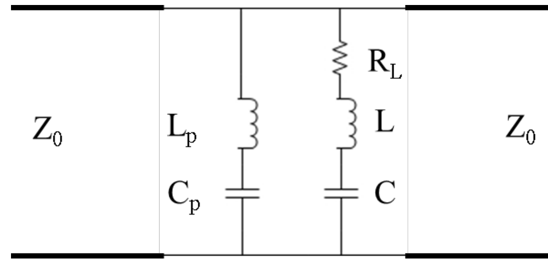

Figure 5.7 Equivalent circuit model of the patch-wire MEFSS for a vertically polarized wave front at a normal incident angle. The optimized parameters are: L = 0.5837 nH, C = 1.0105 fF, C_p = 7.147 fF, L_p = 0.0166 nH, R_L= 6.4479 Ω, Z_0 = 377Ω.

Since $\omega L >> R_L$ these resonant frequencies are approximately equal to:

$$\omega_{z1} = \frac{1}{\sqrt{LC}} < \omega_p = \frac{1}{\sqrt{(L + L_p)\frac{CC_p}{C + C_p}}} \ll \omega_{z2} = \frac{1}{\sqrt{L_p C_p}} \quad (5.4)$$

All the lumped element values in the model can be tuned independently using elements dimensions in the structure. This provides flexibility in adjusting the resonant frequencies in the transmission response by changing the dimensions of the structure. ω_{z1} is determined by the dimensions of the I-shaped elements. Considering $L_p << L$, Equation (5.3) holds, and hence the passband frequency can be pushed as close as desired to the first

transmission zero by increasing C_p, or equivalently reducing g_c, without changing the transmission zero frequency.

1.26 Design Challenges

Two main sources of loss, namely substrate loss and conductor loss, limit the performance of spatial filters by increasing the insertion loss and decreasing the rejection in the transmission response at sub-MMW frequencies and higher,. The dielectric substrate increases insertion loss by creating an impedance mismatch with free space. In addition, the dielectric loss in the substrate can become large in these frequency bands. To reduce losses associated with the substrate, the MEFSS is designed on a 10µm thick (~λ/80) Parylene membrane. Excellent physical and electrical properties such as low intrinsic thin film stress, homogeneous surface and low dielectric constant, makes Parylene suitable for this application. Large areas of thin Parylene layer can be released and handled which makes it ideal for freestanding structures. The low dielectric constant and loss tangent (ε_r =2.9 @ 1MHz, tanδ=0.004 @ 60 GHz [97]) of Parylene is desirable to reduce the mismatch and dielectric loss of the FSS structure. Ohmic loss in the metallic elements is another source of loss which increases the insertion loss in the passband and reduces the rejection in the bandstop. This loss is modeled as a resistance R_L in series with the inductor in the circuit model. This loss is a function of the surface resistivity of the metal strips and the current distribution on the wire elements. Gold has a high bulk conductivity ($\sigma = 4.1\times10^7$ S/m) and its surface resistivity is $R_s = 0.146\ \Omega$ at 220 GHz. However, similar to planar transmission lines, e.g. microstrips and coplanar waveguides, the induced currents are not uniformly distributed on the wire strip surface, as they are mostly concentrated near the

edges of the strips. This effect is due to the singular behavior of the electromagnetic field near a conductor wedge [98]. Figure 5.8 shows the magnetic field distribution around the wire element.

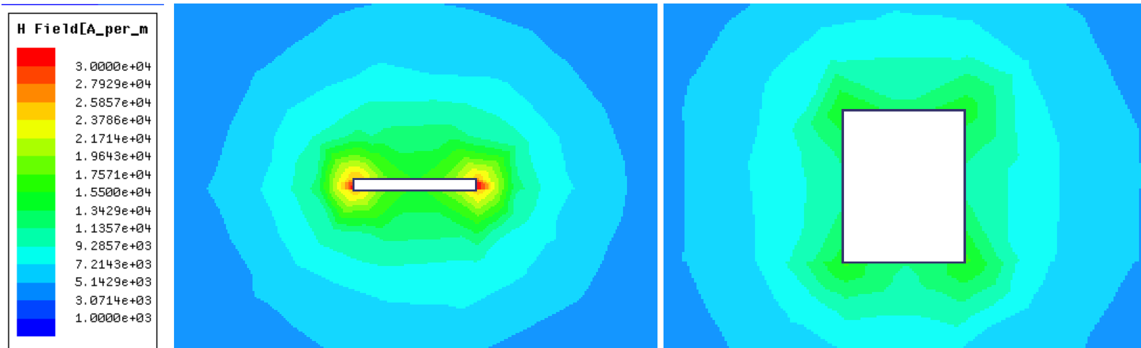

Figure 5.8 Magnetic field distribution around a wire element for two different thicknesses: (a) $t_m = 0.5\mu m$, (b) $t_m = 7\mu m$

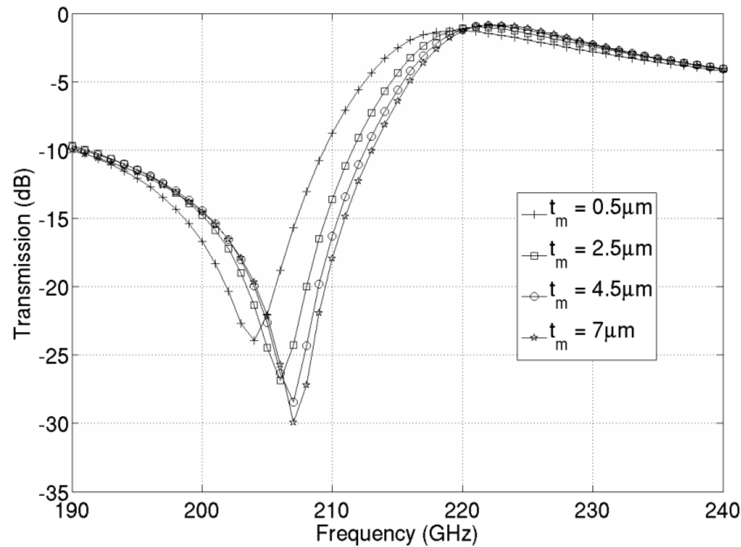

Figure 5.9 Simulation results for the patch-wire MEFSS with different element thicknesses. The insertion loss in the passband and the rejection out of the band improves as the element thicknesses increase.

The surface current density is equal to the tangential component of the magnetic field. To reduce the current density on the edges and increase the effective surface of the

strip, the curvature of the strips near the edges must be reduced. This can be done essentially by increasing the thickness of the strips. Numerical simulations verify that the current distribution is much more uniform on a thick strip as shown in Figure 5.8 (b). Figure 5.9 shows that the insertion loss and isolation are improved as a result of increasing the wire thickness.

1.27 Design Analysis

Full-wave analysis of the structure was performed using HFSS. A single unit cell (Figure 5.6) is excited by Floquet ports and the reflection (S11) and transmission (S21) responses of the proposed MEFSS are computed. Master and slave boundaries are incorporated to model the planes of periodicity for the array and to ensure phase continuity across the unit cells for a desired angle of incidence. The transmission response of the FSS as a function of angle of incidence is shown in Figure 5.10. As shown, the transmission response is not very sensitive to the angle of incidence. Resonant frequencies shift by 1% and 5% for angles of incidence equal to 20° and 50°, respectively, with respect to the normal direction.

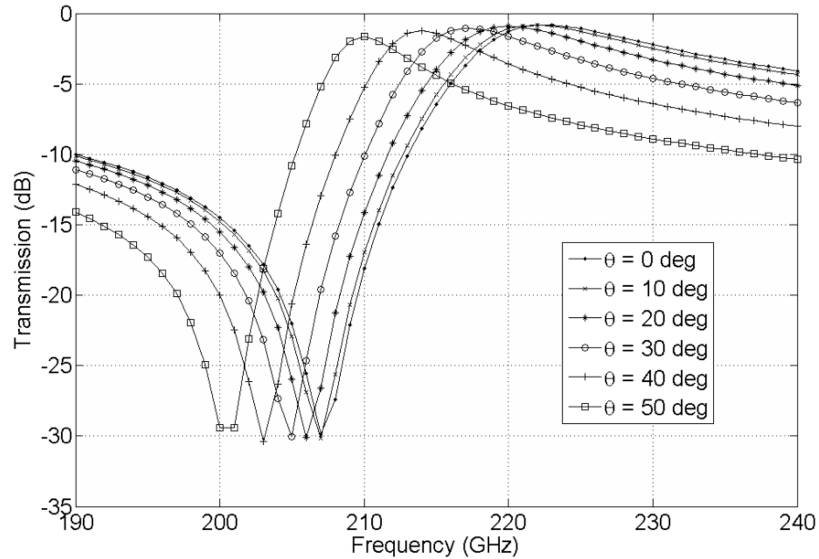

Figure 5.10 Simulation results of the patch-wire MEFSS for different angles of incidence

The equivalent circuit model is simulated with Advanced Design System (ADS). The circuit parameters have been optimized to fit the full-wave analysis results. The lumped-element model is valid as long as the interaction of the FSS elements and the incident wave remains mostly in TEM mode. The first Bragg mode contribution starts to come to effect when the periodicity approaches $\lambda/2$. As the frequency increases and the unit cell dimensions become comparable to the wavelength, the lumped-element circuit model accuracy drops, especially for oblique angles of incidence. Figure 5.11 shows the reflection and transmission responses of the optimized structure and the equivalent circuit model up to 450 GHz. The responses are in close agreement over the entire band. It can also be noted that the second harmonic response is not present (at 414~444 GHz) unlike an equivalent resonant FSS structure design.

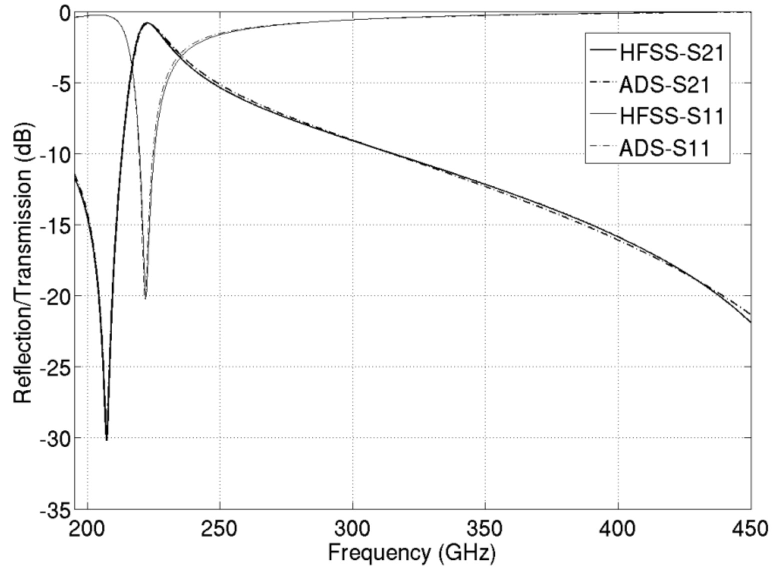

Figure 5.11 Numerical simulations for patch-wire MEFSS at normal incidence

The structure dimensions can be scaled to create the same filtering response at higher sub-MMW and terahertz frequencies. Full-wave simulation results for the scaled MEFSS structures are shown in Figure 5.12. It can be seen that the scaled structures create a filtering response with characteristics identical to the original structure in the corresponding bands. The insertion loss and lower side-band rejection are slightly degraded as the operating frequency increases due to higher conductor loss on the metallic traces.

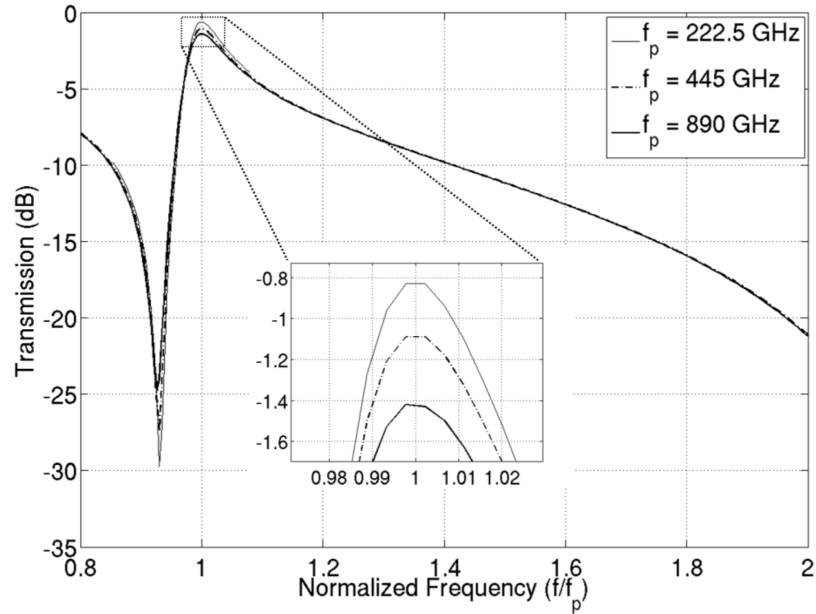

Figure 5.12 Full-wave simulation of the scaled MEFSS for terahertz applications

1.28 Microfabrication Process

The membrane-supported FSS structure was fabricated using wafer microfabrication technology. The fabrication process consists of three major steps: deposition of a thin Parylene sheet on a carrier wafer, patterning and growth of miniaturized elements over the Parylene layer, and release of the Parylene-supported structure from the carrier wafer. More details of the fabrication process are shown in Figure 5.13.

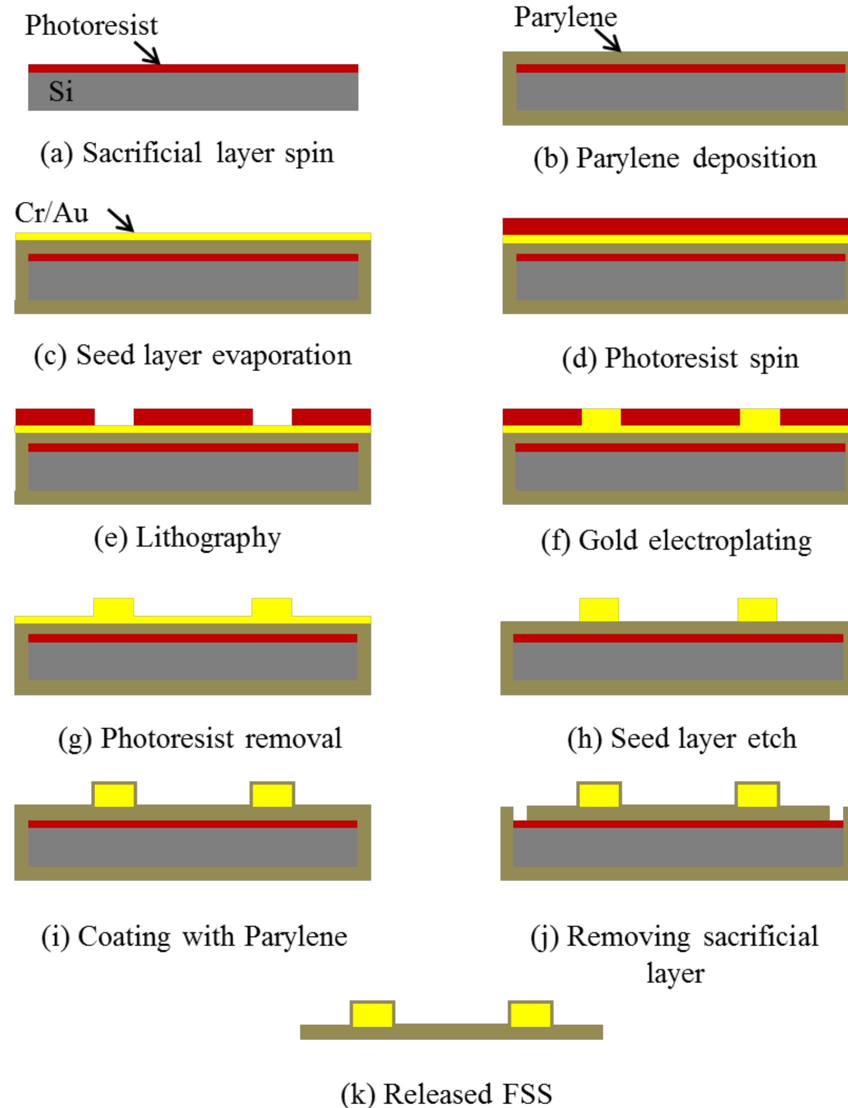

Figure 5.13 Schematic diagram of microfabrication of membrane-supported MEFSS

First, a bare polished silicon wafer is coated with a thin photoresist layer and a 10µm thick layer of Parylene-C is deposited. Photoresist is used as a sacrificial layer which will be dissolved on the last step to release the Parylene membrane. The structure consists of 7µm thick elements with feature dimensions as small as 5µm. Gold electroplating is used to achieve thick elements with highly accurate dimensions. First, a thin layer of chrome and gold (500°A /500°A) is evaporated on the Parylene membrane as a seed layer. Next, the seed layer is patterned with the 2D array of FSS elements shown in Figure 5.4.

A 10µm thick layer of photoresist AZ 9260 is patterned with the features to allow electroplating up to 7µm. Then, the features are electroplated to the desired thickness. After electroplating, the photoresist is dissolved and the seed layer on the previously covered areas is removed by wet etching gold and chrome. Although chrome/gold elements have good adhesion to Parylene, the elements will fall off the membrane when moved and shaken on portable radar systems. To resolve this problem, a thin layer of Parylene (0.5µm) is deposited on the FSS to seal the surface and keep the gold elements in place. This thin Parylene layer increases the capacitance in the circuit model and so the thickness of this layer can be further used as a parameter to tune the resonant frequencies of the filter. Microscopic images of the fabricated structure are shown in Figure 5.14.

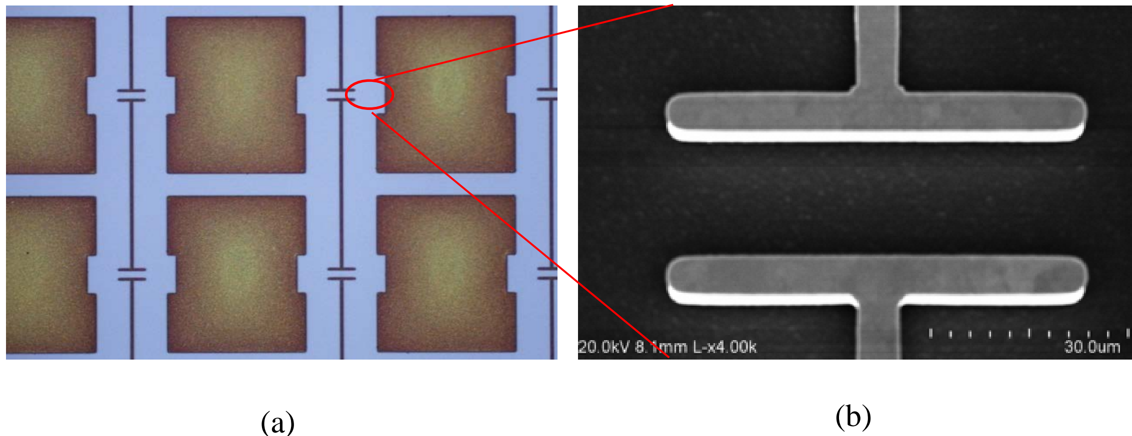

(a) (b)

Figure 5.14 The fabricated membrane-supported MEFSS (a) microscopic image, (b) Scanning electron microscope (SEM) image of electroplated gold elements.

The membrane-supported FSS needs to be detached from the carrier wafer in the last step. This is done by dissolving the photoresist underneath the Parylene layer in an acetone solution. Acetone dissolves the photoresist through cuts made at several locations near the edge of the wafer. After the photoresist is completely removed the sample is placed in

isopropanol to remove any acetone residues on the membrane. A PVC circular support is glued to the FSS and the membrane is cut and released from the carrier as shown in Figure 5.15.

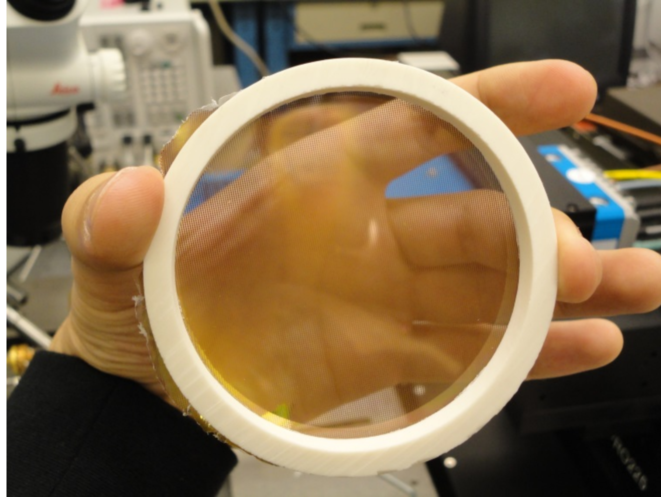

Figure 5.15 The membrane-supported MEFSS after release.

1.29 Free-Space Measurements

The transmission response of the fabricated structure is obtained experimentally using the free-space measurement setup shown in Figure 5.16. The Agilent N5245 4-port performance network analyzer is used along with OML MMW frequency extending modules to perform full 2-port S-parameter measurements at Y-band. Two identical pyramidal horn antennas are connected to the frequency extending modules to create a vertically polarized wave front. The beamwidth of the antennas is 13° in the E-plane and 10° in the H-plane and the far-field range is 16cm. The two antennas are separated by 32cm and the FSS is placed in between, normal to the broadside of the antennas, equally spaced from each antenna.

Figure 5.16 Free-space measurement setup. FSS screen is placed normal to antennas broadside.

The antennas foot print at the FSS location is 3.6cm which is far less than 10cm diameter of FSS holder. Hence, there is little perturbation due to scattering from the edges of the holder. Transmission (S_{21}) measurements are range gated in the time domain to eliminate multiple reflections from the frequency extending modules. Range gating is achieved by applying the Kaiser-Bessel gating function (β=15) centered at 1.07 ns on the time-domain transmission response. The two antennas are aligned for maximum transmission response and system is calibrated using the free-space thru response. Figure 5.17 shows the measured transmission response of the membrane-supported MEFSS at normal angle of incidence.

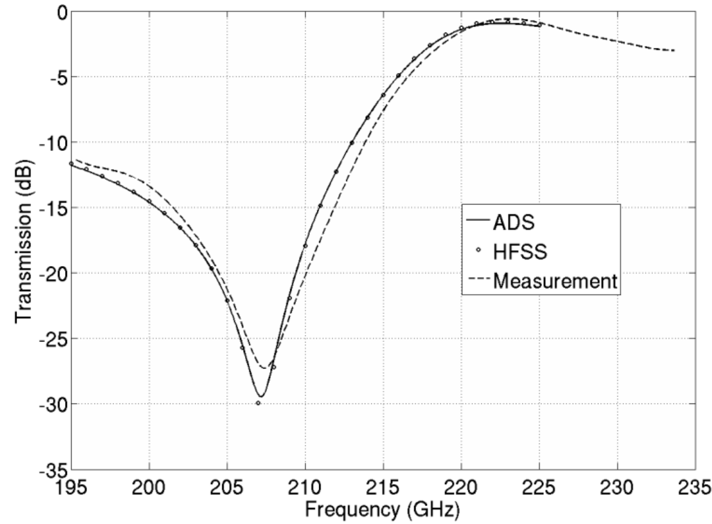

Figure 5.17 Measured and simulated transmission response of membrane-supported miniaturized-element FSS.

The measured response shows a 0.6 dB insertion loss in the 221-223 GHz band and more than 25 dB rejection in the 206-208 GHz band for vertical polarization at a normal angle of incidence.

1.30 Summary

A new single face, membrane-supported bandpass MEFSS with an adjacent zero in the transmission response for image rejection in a 222 GHz radar system is presented. The proposed miniaturized-element patch-wire configuration creates a pole and an adjacent transmission zero filtering response for a vertically polarized electromagnetic wave. The location of the pole and the zero can be independently adjusted by varying the geometrical dimensions of the structure. The proposed MEFSS is designed using a simple circuit model and a full-wave analysis which is then realized on a thin Parylene sheet to minimize losses associated with the substrate. The thickness of the metallic traces is optimized to reduce

the conductor loss. The membrane-supported MEFSS is fabricated using microfabrication techniques and its transmission response is measured using a free-space measurement setup. Measurement results show that the transmission response has 0.6 dB insertion loss in the passband (221-223 GHz) and more than 25 dB rejection around the lower side-band (206-208 GHz) which is in good agreement with numerical simulations of both the structure and its circuit model. In the next chapter the instrumentation radar is utilized to investigate radar scattering phenomenology in an indoor setting.

CHAPTER 6
MMW RADAR INDOOR PHENOMENOLOGY

1.31 Introduction

To examine the utilization of the proposed 240 GHz radar for collision avoidance and building interior mapping applications, a study of the interaction of electromagnetic waves with objects in the indoor environments is needed. The phenomenology of indoor environments at Y-band frequencies is investigated in this chapter. A stepped-frequency 215 GHz instrumentation radar system capable of vertical and horizontal polarization transmission and reception is utilized to collect backscatter data in an indoor environment as the radar is moved within the building [99]. In Section 6.2, the detail specifications of the 215 GHz radar front-end and the measurement setup are presented. In Section 6.3, the measurement results are used to create two-dimensional images of the scanned area. These images can be generated in real time for obstacle-detection and navigation of autonomous robots. To analyze the interior layout detection accuracy for different polarizations, backscatter measurements are performed for VV and HH polarizations. As will be shown in Section 6.4, HH measurements give much higher quality images of the environment compared to the vertical polarization.In Section 6.5, these images are integrated in a global coordinate reference frame to create a complete map of the interior layout of the building. In Section 6.6, a number of image processing techniques are applied to the raw radar range profile maps to enhance the image quality and to remove the undesired effects. A linear feature extraction method based on the Hough transform is used to extract the rectilinear

features (walls, doors, etc.) in the complete map. Algorithms are developed to eliminate the ghost targets resulting from multi-path in the hallways. Polarimetric backscatter measurement of different indoor materials is performed in Section 6.7 to gain a better understanding of radar backscatter in the hallways and complete the indoor phenenomenology study.

1.32 Instrumentation Y-band Radar System

An instrumentation radar operating at 215 GHz is assembled using off-the-shelf components at the University of Michigan Radiation Lab (Figure 6.1) to investigate the performance of Y-band radars in the indoor environment.

Figure 6.1 The Y-band instrumentation radar

This radar is quasi-polarimetric which can measure the backscatter response in the four principal polarization configurations (VV, HV, VH, HH). The radar can operate in FMCW or stepped frequency modes. For the indoor navigation application, the Y-band

radar is operated by a vector network analyzer (VNA) for data collection and signal processing to acquire the range information.

1.32.1 Radar Front-End Module

A block diagram of the University of Michigan 215 GHz radar front-end is shown in Figure 6.2. A single Indium Phosphide (InP) Gunn oscillator generates the necessary LO power at 106 GHz for both up-conversion and down-conversion to maintain the signal coherence in the system.The LO signal is divided by a 6-dB waveguide directional coupler between transmitter and receiver stages. The input IF signal is fed into the upconvertor by the VNA. The LO signal is mixed with IF signal and then upconverted to 215 GHz through a multiplier varactor. In the receiver, the received RF signal is mixed with a sample of LO signal and downconverted to IF signal in a sub-harmonic mixer. Two amplifier stages amplify the IF signal by 53 dB. A bandpass filter at the input of the downconvertor blocks the leakage of RF transmit signal into the receiver.

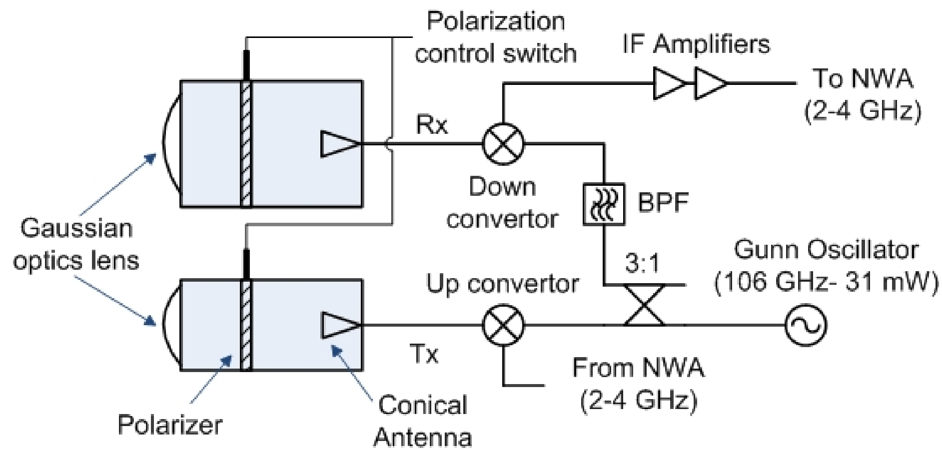

Figure 6.2 Block diagram of the Y-band radar front-end

To achieve significant isolation between the transmit and the receive channels, two separate antennas for the transmitter and receiver are used. Gaussian Optics Lens Antennas (GOLAs) are used as transmit and receive antennas with narrow beamwidths of 2.5° and 1.5° respectively. The transmitter antenna has a wider beamwidth to minimize the parallax problem. The polarization of the transmit and the receive signals are controlled by wave plate polarizers that are placed in the lens house between the conical horn antenna and the lens. These polarizers can be appropriately oriented to achieve pure vertically (/horizontally) polarized waves.

1.32.2 Measurement Setup

A full scan of the environment is needed to map the hallways and obstacles in the indoor environment. As shown in Figure 6.3 (a), the radar is placed on a turntable with full rotation capability (360°). The turntable is controlled with an Aerotech Soloist SC motion controller. The radar is connected to a HP 8735 (30kHz-6GHz) VNA for data acquisition. A LabView interface has been developed to control the radar angular position and the data collection. The whole setup is placed on a portable cart to facilitate data collection in the hallways (Figure 6.3 (b)).

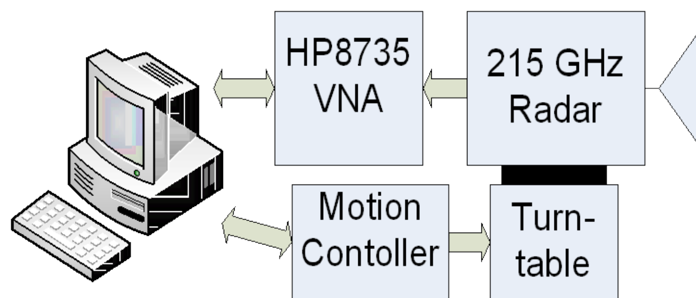

(a)

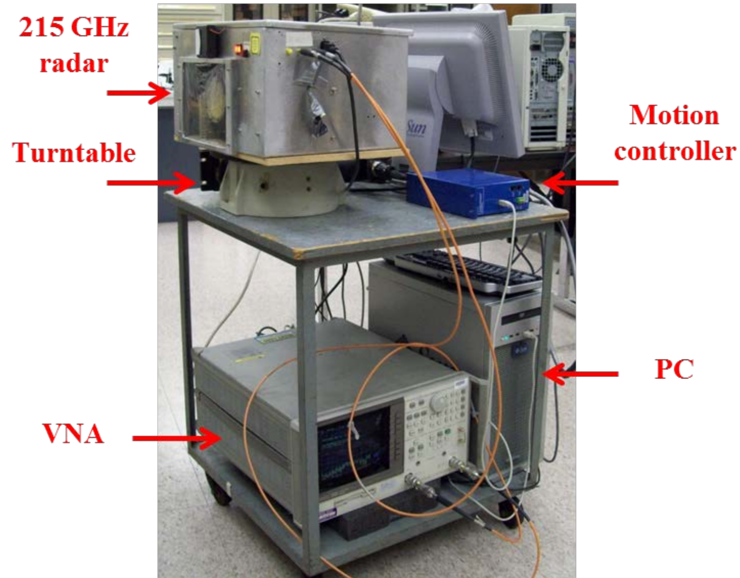

(b)

Figure 6.3 The measurement setup for indoor backscatter phenomenology study (a) block diagram [100] (b) the setup placed on a portable cart

1.33 Data Collection and Image Formation

The radar system is moved in the University of Michigan's EECS building hallways, as shown in Figure 6.4, to create a complete radar map of the interior layout. The measurement setup is moved in steps of 1 meter for a total of 127 steps. At each step, the radar scans the environment from -90° to 90° in angular steps of 1°.

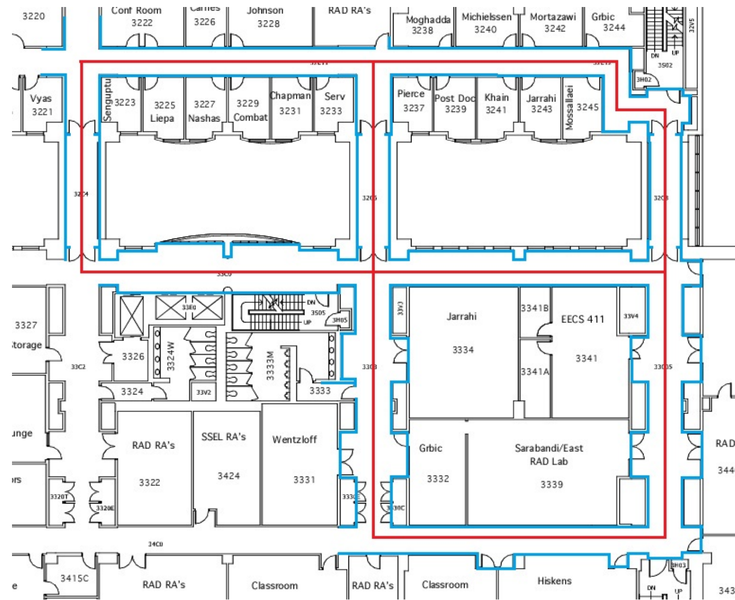

Figure 6.4 EECS building layout and the radar path in the corridors

Backscatter data collection is performed by sweeping the IF frequency from 2.2 GHz to 3.2 GHz, resulting in a range resolution of 15 cm. The collected frequency domain data is then transformed from frequency domain to the time domain. Time domain data for a sample backscatter measurement is shown in Figure 6.5. The actual distance of the target to the radar must be calibrated with respect to the RF leakage. The RF leakage is the result of finite isolation between the transmitter and the receiver.

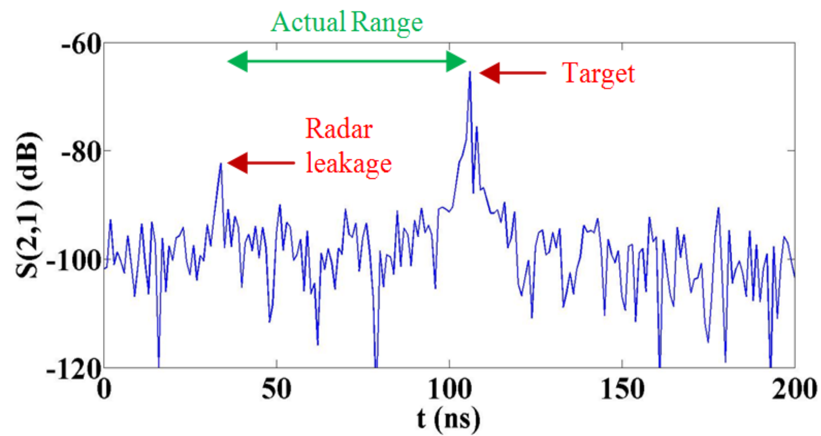

Figure 6.5 Time domain response of a sample backscatter measurement

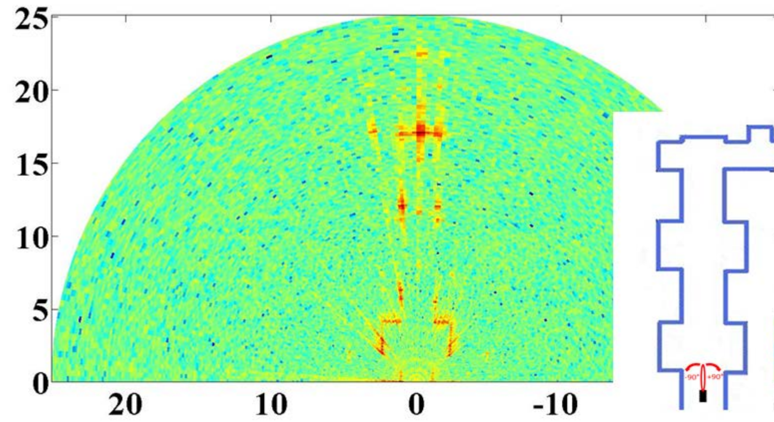

(a)

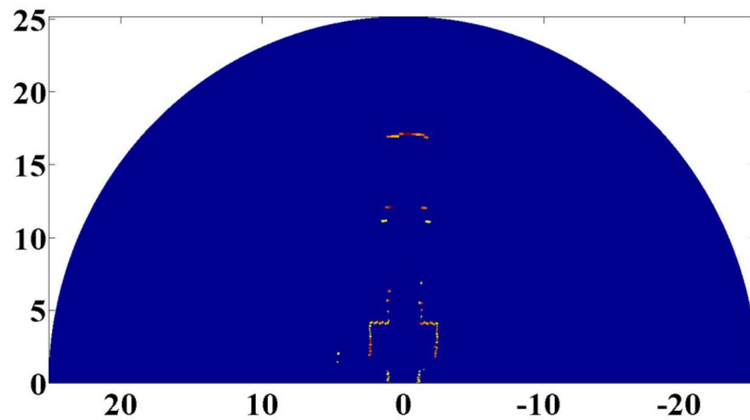

(b)

Figure 6.6 2D image created by 180° scan of the hallway (a) raw data (b) after applying peak detection method

Two dimensional radar images of the scanned scene can be formed by mapping the time domain calibrated backscatter amplitude of the 181 measurements from -90° to 90° scan on a polar plot. Figure 6.6 (a) is an image of a sample scan with HH polarization. As can be seen, partial layout of the hallway is detectable in the image. However, background noise and the ripples created by double bounce off the large scatterers reduce the quality of the image. A simple peak detection method has been used to eliminate these undesired

effects. As can be seen in Figure 6.5, the largest backscatter amplitude corresponds to the actual target. Hence, the largest peak in each measurement is selected and the rest of the points are discarded. The corrected image is shown in Figure 6.6 (b).

1.34 Polarization Analysis

Polarimetric backscatter measurements in the hallways show that there are significant differences between the images created by the backscatter responses of vertical and horizontal polarizations. Figure 6.7 shows a hallway with tile walls and Figure 6.8 shows the corresponding VV and HH radar images.

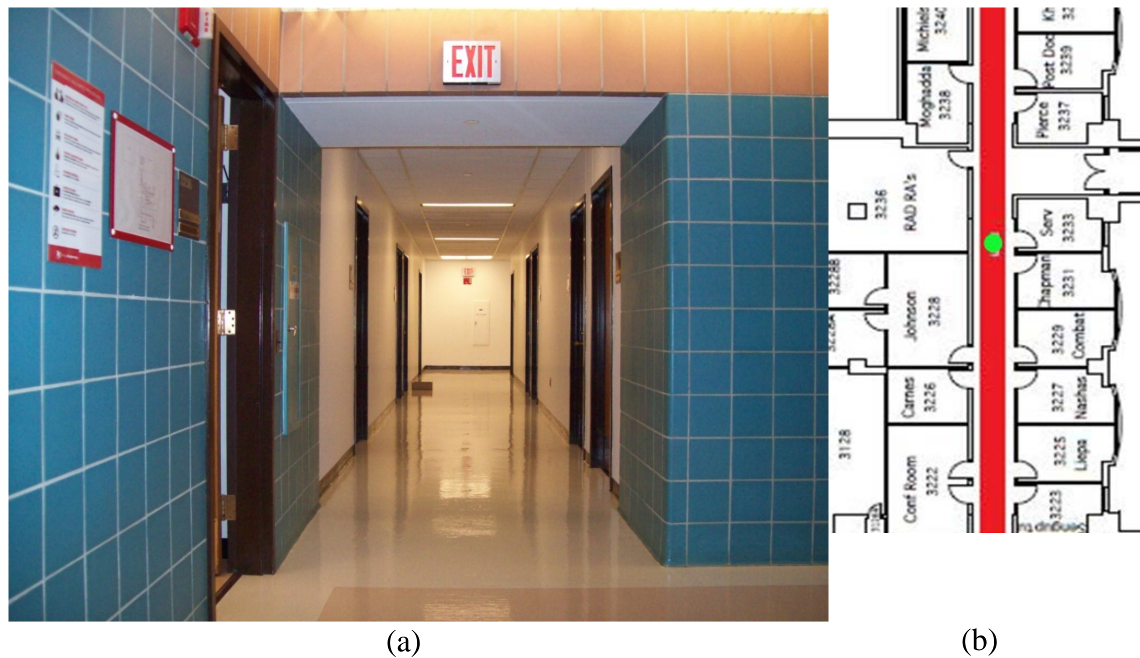

(a) (b)

Figure 6.7 (a) Photo of the scanned view (b) radar position in the hallway

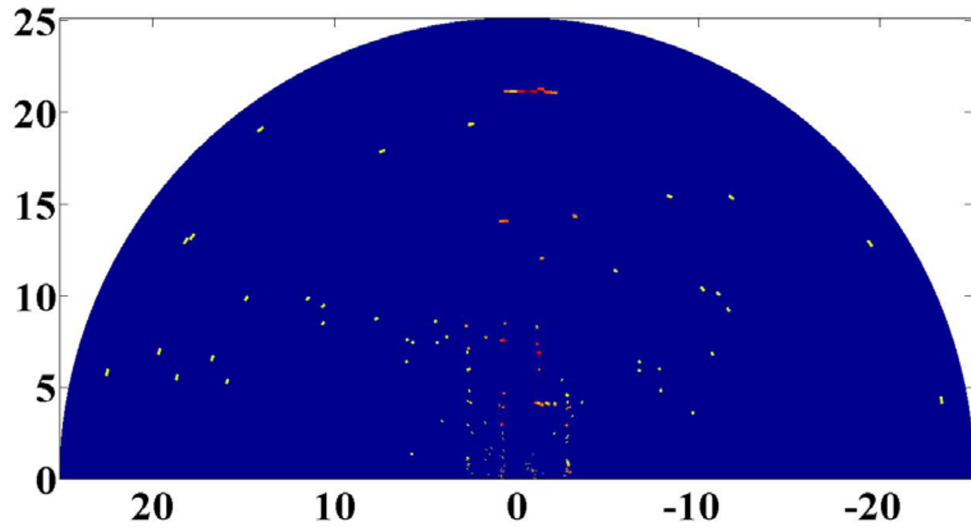

(a)

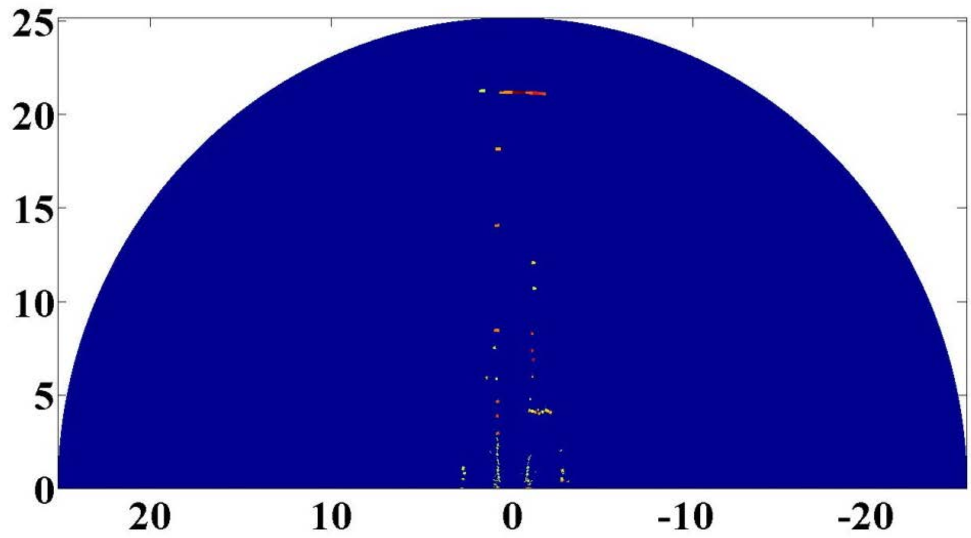

(b)

Figure 6.8 The 2D image created by 180° scan of the scene shown in (a): (b) Vertical polarization (c) Horizontal polarization

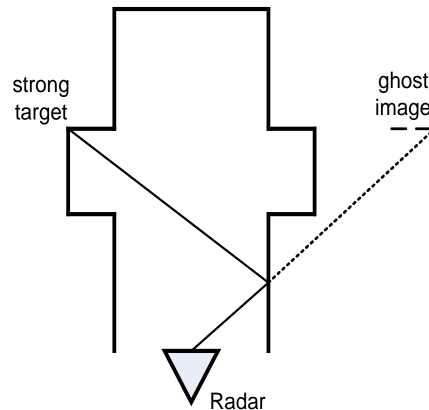

Figure 6.9 Ghost images are result of specular reflection of large scatterers from smooth surfaces at oblique angles of incidence.

For angles near the normal incidence the two polarizations show little difference in the target detection. However, the backscatter signal is significantly different for oblique angles of incidence. This can be explained by the fact that, at oblique angles of incidence, the specular reflection from planar surfaces is higher for TE (vertically polarized) waves compared to TM (horizontally polarized) waves. At oblique angles of incidence, the specular reflection is not in the backscatter direction and, hence, does not contribute to the surface detection. However, the specular reflected power can get re-reflected from strong targets in the environment creating “ghost” targets in the image (Figure 6.9). The unrealistic targets in Figure 6.8 (a) are result of the reflected signal from targets in the hallway. Due to Brewster angle effect the TM polarized incidence has a higher transmission coefficient into the wall and lower reflection coefficient. The advantage of TM polarization is twofold: 1) higher transmission into inhomogeneous dielectric wall material which causes higher volume scattering and larger backscatter coefficient at oblique incidence, and 2) lower reflection coefficient which reduces multipath and thus the

number of the ghost targets. The effect of polarization on the backscatter response is studied and discussed more in Section 6.7.

1.35 Mapping the Building Interior Layout

The polar radar data collected at all positions along the radar path can be integrated to create a map of the entire scanned interior region. The scanned area is discretized into square elements, as shown in Figure 6.10, corresponding to elements of a global coordinate frame. The square elements are 7.5cm by 7.5cm which sets the resolution of the final map. The detected target from the polar map at each radar location can be associated with a single element in the global coordinate frame if the relative position and attitude of the radar with respect to the global coordinate system is known.

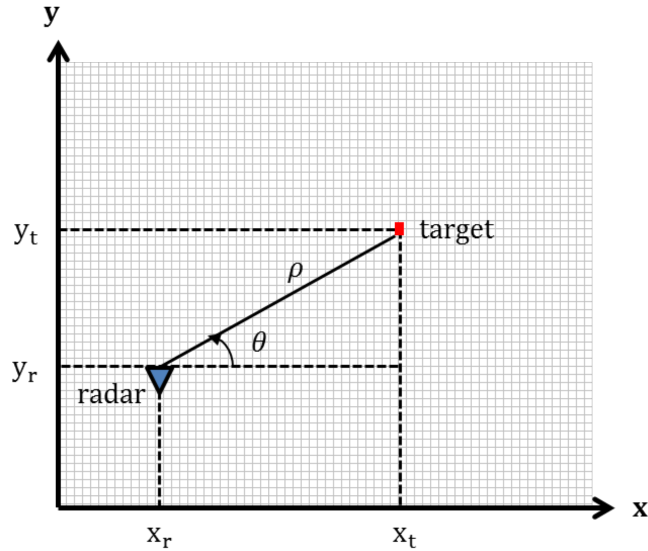

Figure 6.10 The target location is associated with an element in the global coordinate matrix corresponding to the discretized scanned area

The measured target at (ρ,θ) is associated with the element (m,n) of the global matrix by the following equations:

$$m = \left\lfloor \frac{x_t + \rho\cos\theta}{\delta x} \right\rfloor \quad , \quad n = \left\lfloor \frac{y_t + \rho\sin\theta}{\delta y} \right\rfloor \qquad (6.1)$$

The location of the radar was determined crudely by marking the floor at regular distances. The complete map of the building after integrating all polar radar images into a global coordinate frame is shown in Figure 6.11.

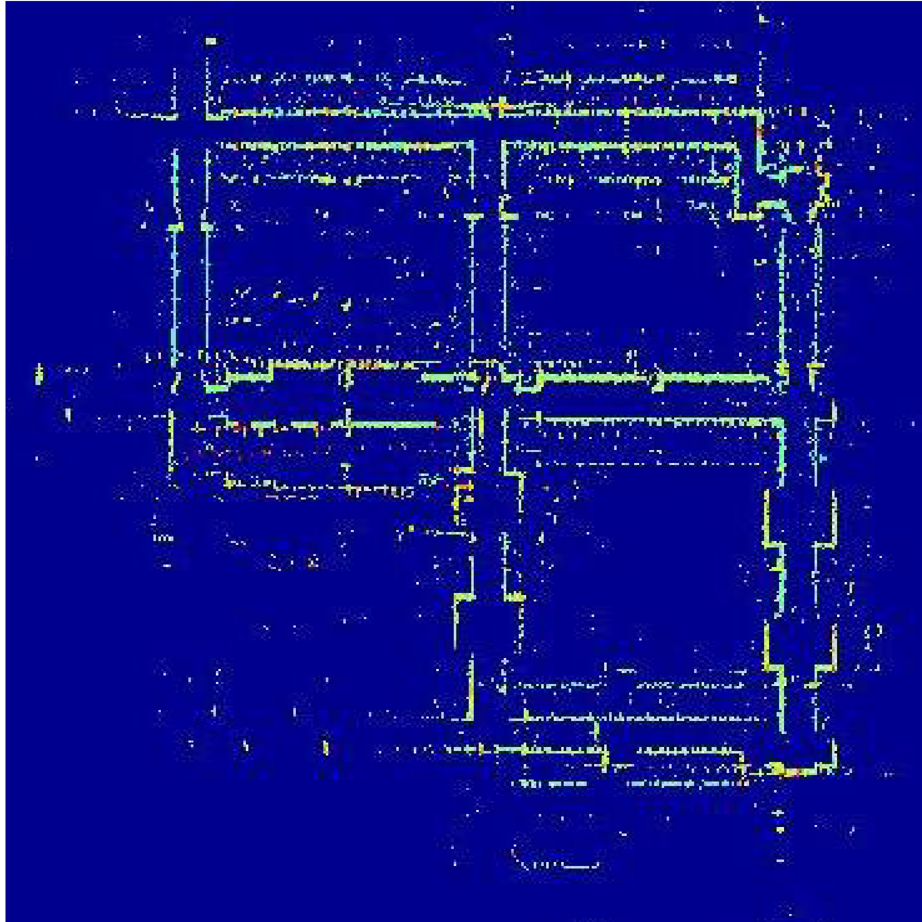

Figure 6.11 The complete map of the building is created by integrating the radar images at each step

1.36 Image Processing and Feature Extraction

Although the approximate layout of the hallways can be detected in the raw map shown in Figure 6.11, the aggregated radar map still contains significant number of missing elements (gaps) in the interior layout. In addition, unrealistic targets due to noise and multipath effects are present in the map. A number of image processing techniques are employed to extract the features in the indoor scenario and enhance the accuracy and interpretability of the map.

1.36.1 Linear Feature Extraction

Most of the obstacles in an indoor scenario, i.e. walls and doors, have rectilinear patterns. In a two-dimensional map, these obstacles reduce to linear features. Hence, a linear feature extraction method can be applied to extract the interior layout from the raw map.

1.36.1.1 Hough Transform

The Hough transform is a feature extraction technique used in image analysis, computer vision, and digital image processing. This transform is a computationally efficient line detection technique that is utilized for line feature extraction in images [101, 102]. The main advantages of the Hough transform are that it is relatively unaffected by gaps in lines and by noise, as is required for this application. Hough transform is based on the parameterization of straight lines in the x-y plane using the following equation:

$$x \cos\theta + y \sin\theta = \rho \qquad (6.2)$$

As shown in Figure 6.12, this parameterization specifies a straight line, uniquely, by its distance from the origin (ρ) and the angle of the normal to the line with respect to the x-axis (θ). Hough transform maps the image plane (x-y space) to the parameters plane (ρ-θ space) where each point in the image plane is mapped to a sinusoid in the parameters plane. However, based on the equation (6.2), sinusoids corresponding to co-linear points in the image plane intersect at a single point in the parameters plane (Figure 6.13). Therefore, the problem of finding lines (co-linear points in the image plane) is converted to problem of finding concurrent sinusoids in the parameters plane.

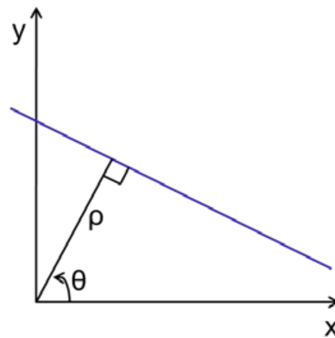

Figure 6.12 ρ-θ parameterization of straight line

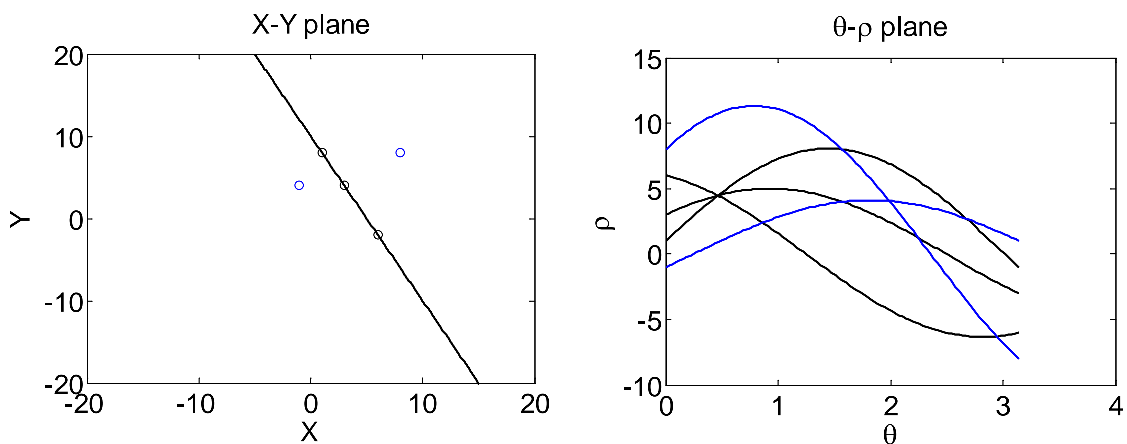

Figure 6.13 Sinusoids corresponding to co-linear points (black points) intersect at a unique point in the image plane a) x-y plane, b) Hough transform image plane

1.36.1.2 Line Detection Using Hough Transform

To perform line segment detection, the ρ-θ plane is discretized into grids of $\Delta\rho$ and $\Delta\theta$ (the desired error margin) in the region $0 \leq \theta < \pi$, $-R \leq \rho \leq R$ where R is the distance of the farthest point from the origin in the image plane. This forms a two-dimensional array for the parameters space. For each point (x,y) in the image space, the corresponding sinusoid is entered in the array by incrementing the element which the sinusoid crosses in the array. The next step is finding local maxima in the parameters array which correspond to lines in the image. A threshold is set for the maxima selection to select long enough lines to remove the noise. The threshold level is set to 5 sinusoid crossings based on this mapping's typical feature sizes. After the local maxima in the array are detected, the lines corresponding to these elements are drawn in the image plane. This is done by selecting all the elements in the global coordinate matrix that satisfy equation (2) for the particular point (ρ_i, θ_i) in the parameters space. However, the original map may not contain the complete lines that are detected by the inverse Hough transform, but only segment/s of those lines. To identify these line segments the original image is examined for pixels lying on the detected lines. The detection algorithm selects a group of pixels as a line segment if they satisfy the following two criteria: 1) the number of pixels forming a line segment must be larger than a predefined parameter n and 2) the number of missing pixels on a line segment must be less than a predefined parameter m. Based on the map characteristics, the parameters are set to $m=6$ and $n=2$. The feature extracted mapping after Hough transform is shown in Figure 6.14.

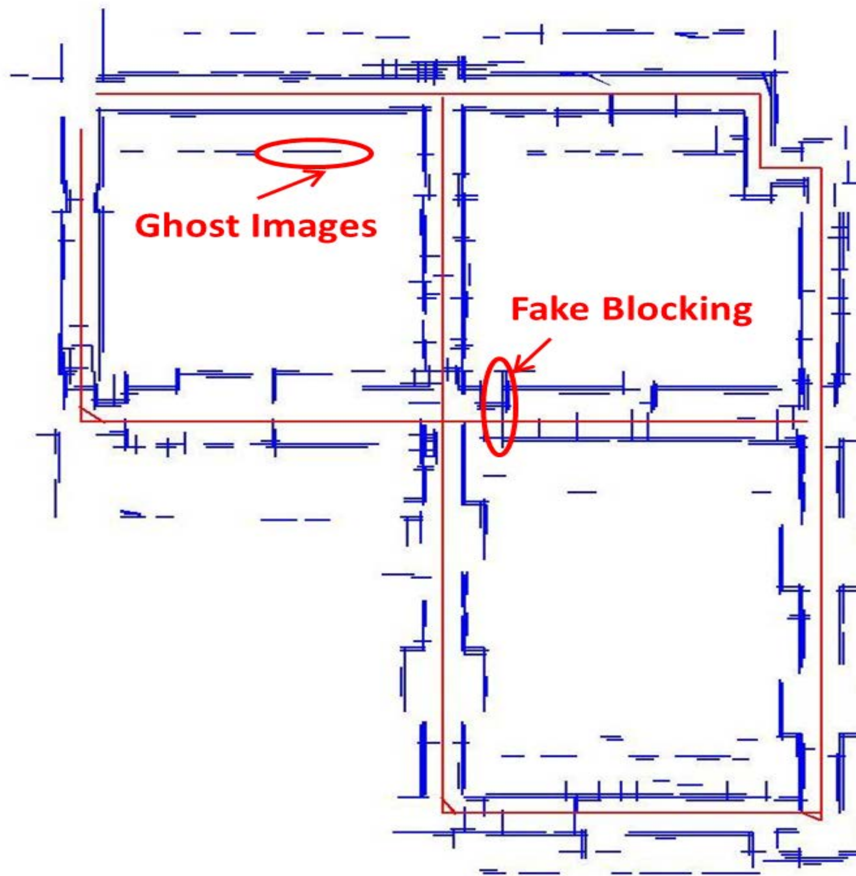

Figure 6.14 The final map after linear feature extraction using Hough transform. Ghost images and fake blockings are still present in this image.

1.36.2 Ghost Image Elimination

As shown in Figure 6.14, there are "ghost" images present in the final map that are not real targets. These false image segments are result of multiple signal bounces among walls and other objects (Figure 6.9). The smooth surfaces are easily detected as the radar moves forward and the angle of incidence approaches the normal direction. In addition, Hough transform fills in the missing elements of the line segment containing that surface. This allows for development of a straight forward algorithm based on the following observation to remove the ghost images in the final map: if the line-of-sight line between

the radar and a target is blocked by another target, that target is not real and must be eliminated. This simple algorithm eliminates most of false targets.

1.36.3 False Passage Blocking Elimination

As shown in Figure 6.14, some of the hallway openings in the map are blocked by unrealistic obstacles. This effect happens when the radar is far from the opening in a hallway and the radar antenna foot print becomes comparable with the width and height of the hallways. At far distances from the radar, the radar beam overlaps with the corners and ledges at hallway junctions that create backscatter and appear as blockage. However, as the radar approaches the opening and the beam becomes narrower these backscatter components disappear. Based on this observation an algorithm is developed to distinguish and remove the radar responses at boresight that are present in one scan and gradually disappear in the consecutive radar scans. The final map after applying ghost image and false blockage elimination algorithms is shown in Figure 6.15. As can be seen, the final image is a very accurate representation of the actual map shown in Figure 6.4.

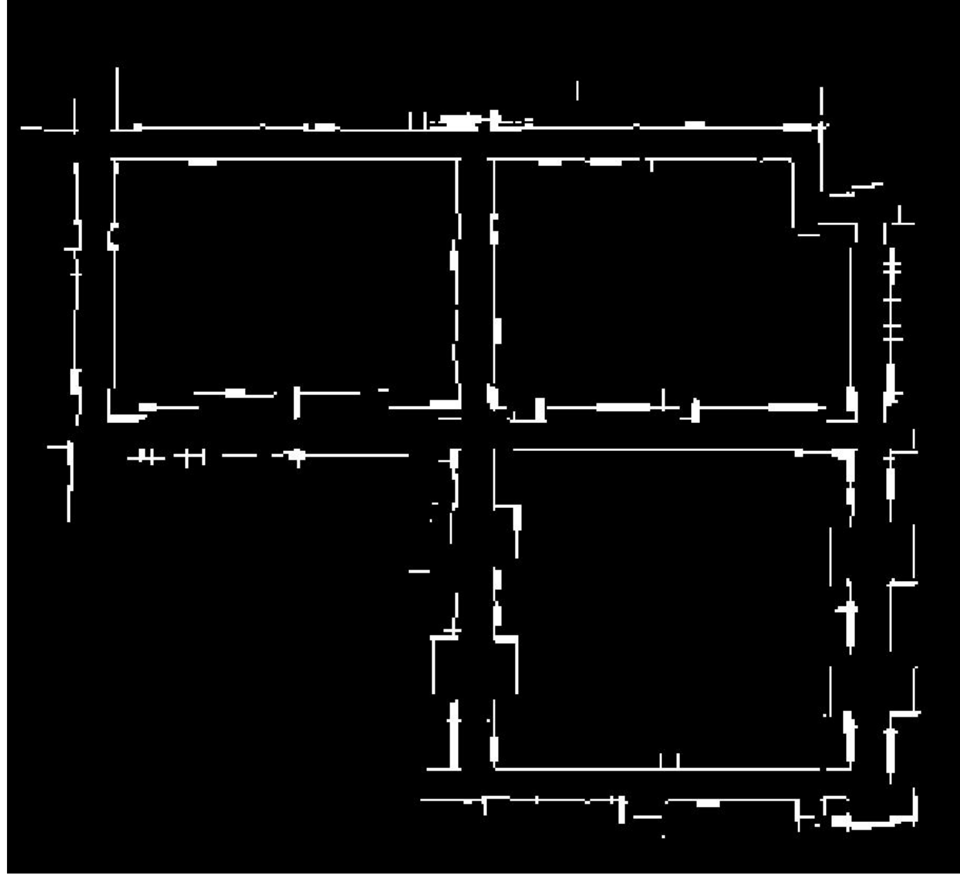

Figure 6.15 The final map after ghost image and fake blocking elimination

1.37 Y-band Backscatter Measurements

To gain a better understanding of Y-band radar backscatter in the hallways, backscattering coefficients measurement of indoor building material as a function of incidence angle is performed. Backscattering coefficients are the common quantities for characterizing scattering behavior of distributed targets which is defined by

$$\sigma_{mn}^{0} = \frac{4\pi}{A}\langle|S_{mn}|^{2}\rangle \quad , \quad m,n = v,h \tag{6.3}$$

where A is the illuminated area and S_{mn} are the scattering matrix elements.

1.37.1 Measurement Setup

The measurement setup shown in Figure 6.16 is utilized to measure the backscatter response of indoor samples.

Figure 6.16 The backscatter measurements setup. The sample distance to the antenna is 2 meters.

(a)

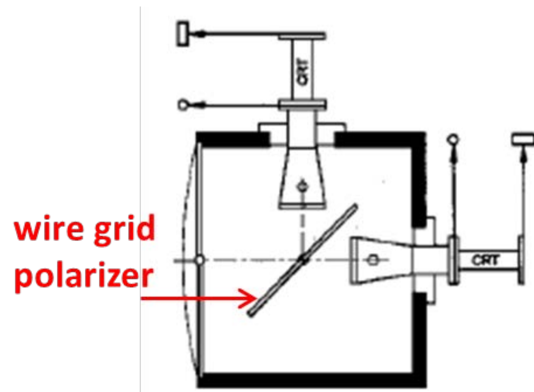

(b)

Figure 6.17 The 3-inch dual-polarized lens antenna (a) front view (b) schematic

The targets are placed on a turntable at 2 meter distance from the antenna enabling accurate rotation in the azimuth direction. The turntable is controlled with an Aerotech Soloist SC motion controller. A custom design Millitech dual-polarized lens antenna is

utilized to perform fully polarimetric (VV, HH, VH, HV) backscatter measurements (Figure 6.17).

The antenna has a very narrow beam enabling measurement of targets with small RCS. Radiation pattern of the antenna in E-plane and H-plane is shown in Figure 6.18.

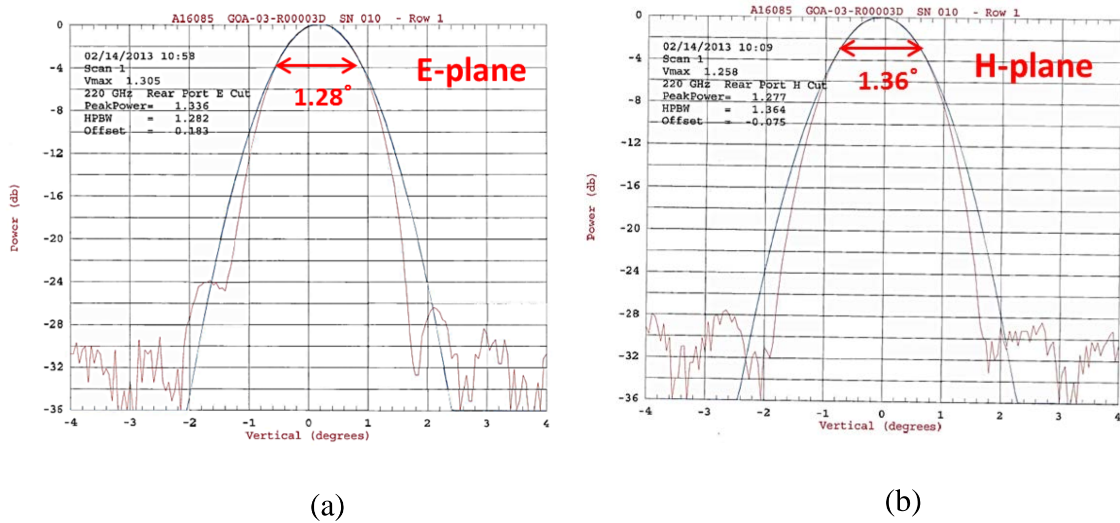

(a) (b)

Figure 6.18 Antenna pattern (a) E-plane (b) H-plane

The antenna is connected to the J-band measurement system (the OML frequency extenders and the 4-port PNA described in Chapter 4) to perform phase-coherent co-pol and cross-pol measurements as a function of incidence angle (Figure 6.19). A MATLAB code is developed to control the turntable and the PNA-X simultaneously to fully automate the data acquisition process.

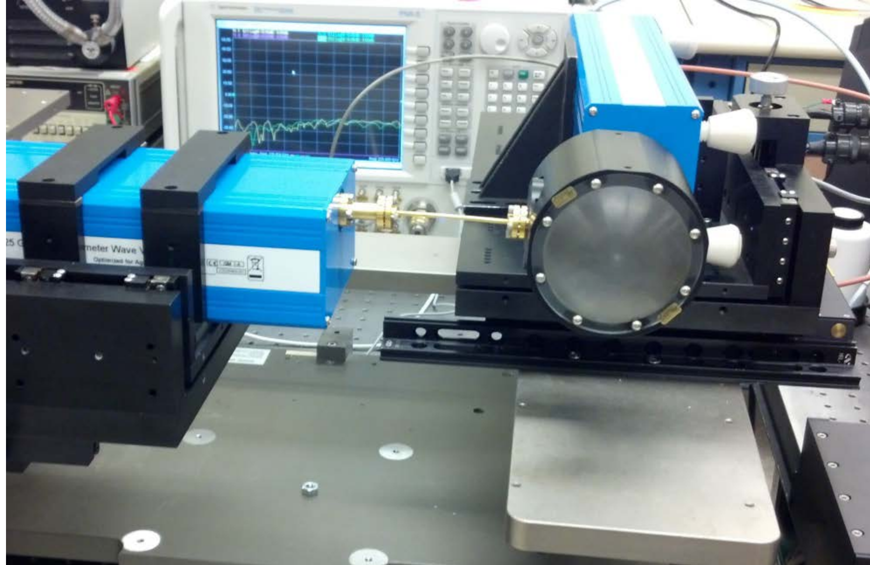

Figure 6.19 The 240 GHz polarimetric measurement system

1.37.2 Data Acquisition and Calibration

At each angle of incidence, the two-port s-parameters data corresponding to the co-pol and cross-pol backscatter responses are collected. The data collection specifications are listed in Table 6.1.

Table 6.1 Data collection specifications

Frequency Range	220 - 325 GHZ
Number of points	401
IF Frequency	1 KHz
Range resolution	1 cm

1.37.2.1 Background Subtraction

Background subtraction is used to reduce the clutter level and enhance target detection. The measured response of the setup environment without the presence of the sample is subtracted from the sample measurements. This reduces the noise level by more than 10 dB down to -90 dB, as shown in Figure 6.20.

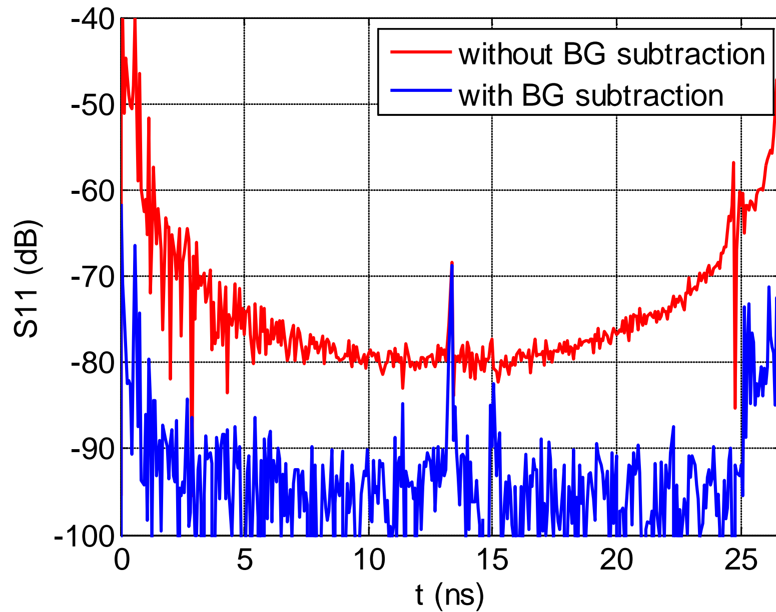

Figure 6.20 Backscatter response of a tilted cylinder in the time domain

1.37.2.2 Range Gating

The time domain response in Figure 6.20 shows that radar leakage and backwall clutter are present in the measured backscatter response. To isolate the target response and eliminate the leakage and other undesired components, the backscatter response is gated in the time domain. The frequency domain response before and after range gating is shown in Figure 6.21.

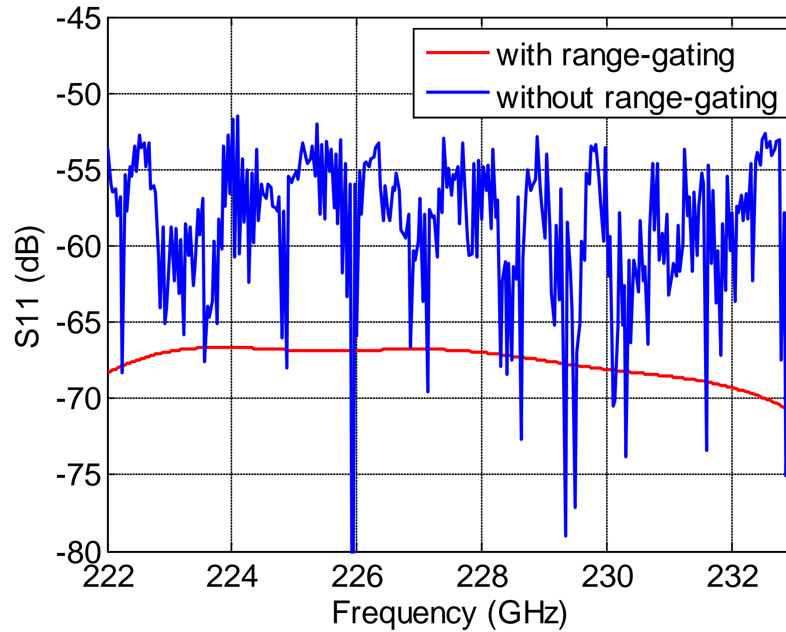

Figure 6.21 Backscatter response of a tilted cylinder before and after range gating

1.37.2.3 IACT Calibration

The measured responses are calibrated using the isolated-antenna calibration technique (IACT). This is a technique for calibrating single-antenna polarimetric radar systems using a metal sphere plus any second target with a strong cross-polarized radar cross section [103]. This technique is suitable for this system since there is good isolation between the two channels (>30 dB).

1.37.2.4 Antenna Spot Size

To make the statistical parameters of the scattered fields independent of the illumination area, the scattering coefficients are normalized to the illuminated area as shown in (6.4). Therefore, the illuminated area (the antenna spot size on the sample) is required to evaluate the backscattering coefficients.

Since the samples are not in the far-field of the antenna, backscatter measurement of a known distributed target is required to calculate the antenna effective spot size. The RCS of a conducting infinite cylinder is analytically known:

$$\sigma = \frac{2\pi L^2 a}{\lambda} \tag{6.4}$$

The measured backscatter response of a copper cylinder is shown in Figure 6.22. Inserting the measured σ in above equation, we have:

$$L = 3.2\ cm \tag{6.5}$$

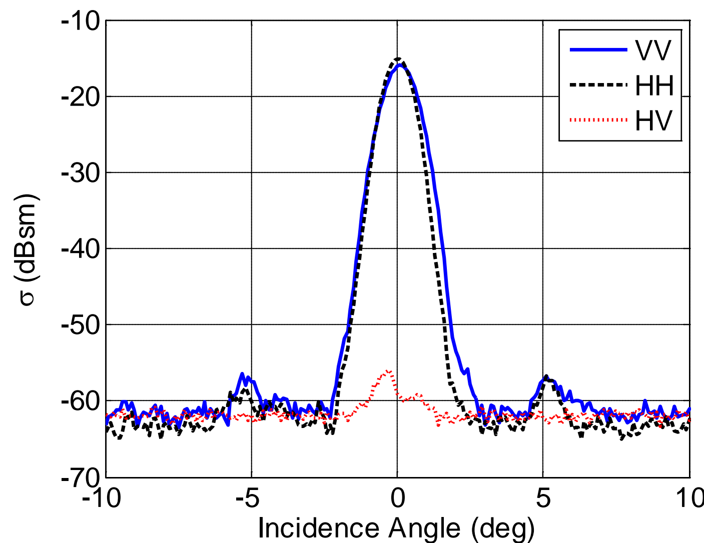

Figure 6.22 Backscatter response of copper cylinder (a=1.2cm)

1.37.2.5 Independent Samples

For distributed targets, to achieve statistical representation of the measured backscatter, 20 spatially independent samples are taken at each incidence angle. Data points in the frequency domain are used to achieve statistical independent samples at oblique angles of incidence. The number of frequency independent samples that can be obtained is calculated from:

$$N = 1 + 2D \tan\theta \frac{BW}{c} \tag{6.6}$$

where D, BW and c are the spot size, bandwidth and speed of light respectively.

1.37.3 Results and Analysis

Backscatter response measurements of the drywall samples are performed at angles of incidence from 0˚ to 70˚. The results are shown in Figure 6.23.

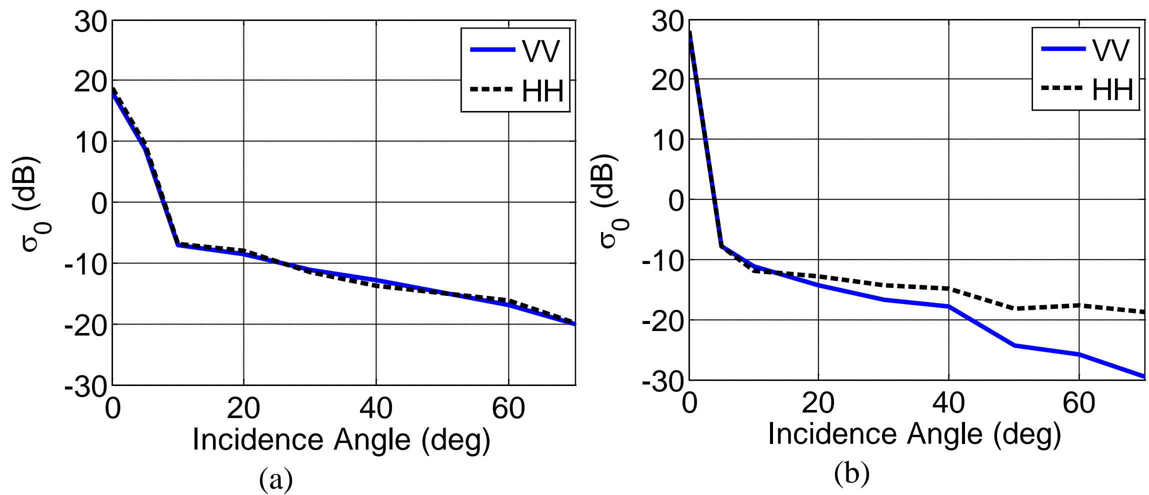

Figure 6.23 Measured backscattering coefficients of (a) drywall without paint (b) drywall with paint

At normal incidence, the backscatter coefficients of the samples (σ_{hh}, σ_{vv}) are high due to the specular reflection from the surface and drops very fast as the incidence angle increases. It is noted that for unpainted drywall (Figure 6.23 (a)) the backscatter coefficients for HH and VV are not much different. However, for painted drywall (Figure 6.23 (b)) the backscatter coefficient for HH is larger than VV at oblique angles of incidence. For painted drywall, the difference between σ_{hh} and σ_{vv} increases to more than 10 dB at 70˚ incident angle.

The difference between the HH and VV backscattering coefficients for painted drywall can be explained by the Brewster angle effect, as mentioned in Section 6.4. The cross section of the wall samples are shown in Figure 6.24. In the case of unpainted drywall, the low dielectric paper layer covering the core of the drywall acts as matching layer for the wave. Hence, the Brewster angle effect is not exhibited for the horizontal polarization and the responses for horizontal and vertical polarization are almost equal at oblique incidence. However, the homogeneous paint layer with high dielectric constant over the drywall causes higher transmission of horizontal polarization into the inhomogeneous gypsum core material at oblique incidence. This results in higher volume scattering from the core material which increases the HH backscatter coefficient at oblique angles of incidence.

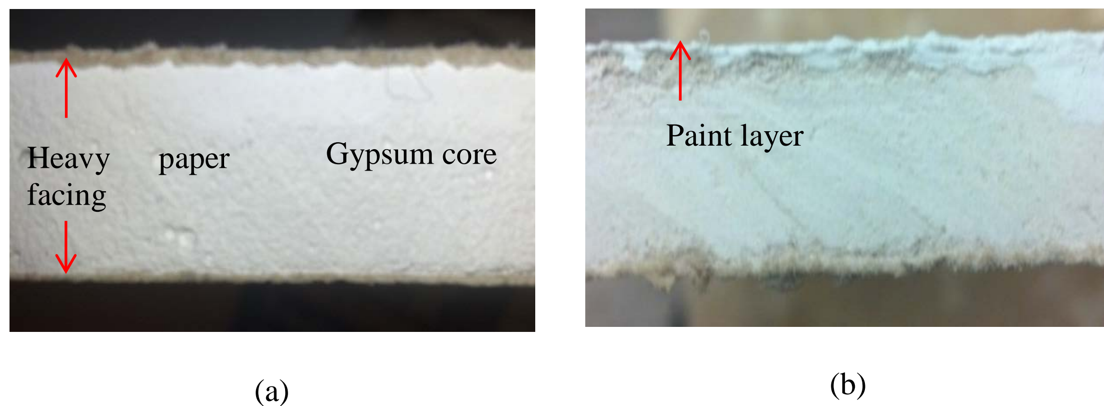

Figure 6.24 Cross section of (a) unpainted drywall and (b) painted drywall

Measured backscatter coefficients of other indoor surfaces are shown in Figure 6.25. Comparing backscattering coefficients (a) to (d), it can be noted that the backscattering coefficients at normal incidence is higher for marble and ceramic surfaces compared to concrete blocks and wood door. However, at oblique incidence the latter surfaces have higher backscattering coefficient compared to the former surfaces. This can be explained by the fact that marble and ceramic are dense (less porous) compared to

concrete and wood. Therefore, specular reflection which is the dominating component at normal incidence is higher due to higher effective dielectric constants. On the other hand, the more porous material creates higher volume scattering which results in higher backscatter coefficients at oblique incidence.

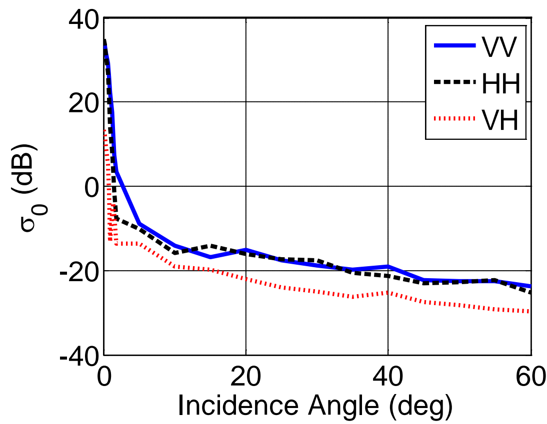

(a)

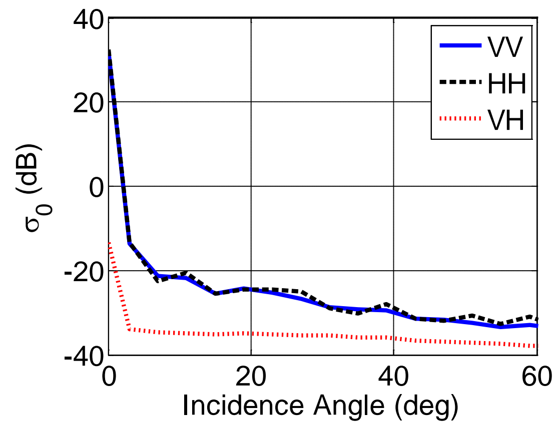

(b)

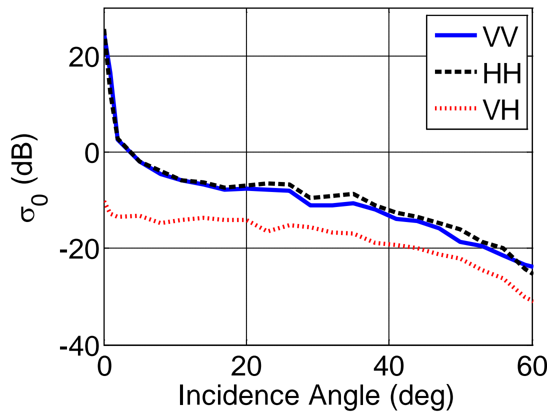

(c)

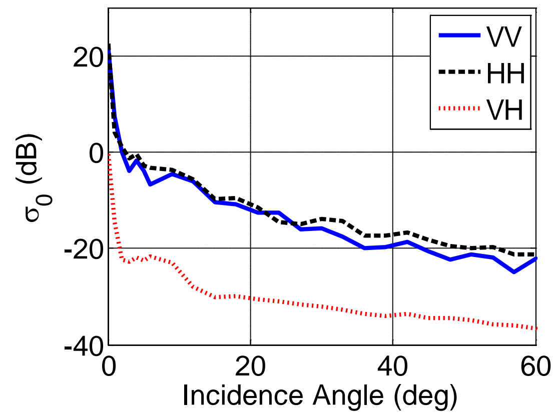

(d)

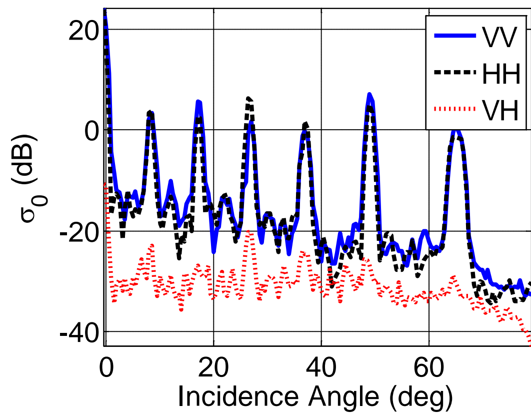

(e)

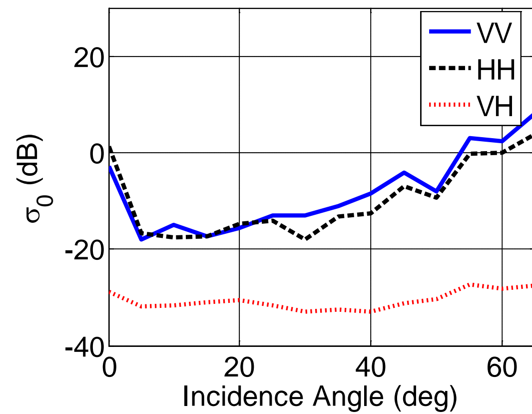

(f)

Figure 6.25 Measured backscattering coefficient of (a) marble, (b) ceramic, (c) concrete blocks, (d) wood door with paint, (e) tile, (f) 6-mm wire mesh

The measured backscattering coefficients of tile surface are shown in Figure 6.25 (e). Unlike the previous surfaces, significant backscatter is created at certain angles. This can be explained by noting the periodic corrugation on the backside of the tile (Figure 6.26). Since the periodicity of the surface corrugation is larger than the wavelength, Bragg scattering create significant backscatter at

$$\theta_n = \sin^{-1}(\frac{n\lambda}{2L}) \tag{6.7}$$

where λ is the wavelength and L is the period.

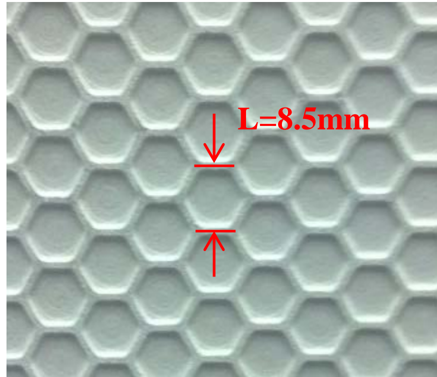

Figure 6.26 Backside view of the measured tile

The measured backscattering coefficients of a 6-mm metal mesh (fence) are shown in Figure 6.25 (f). As can be seen, the fence has considerable backscattering which increases at oblique angles of incidence. This makes the mesh detectable at any angle in this frequency band. It should be noted that although the fence is a periodic structure, Bragg modes are not seen at the expected oblique angles. This is because the irregularities of the wires in the mesh are comparable to the wavelength which avoids coherent addition of scattered field from the wires at Bragg angles.

1.38 Summary

The phenomenology of Y-band radars for navigation and mapping applications in an indoor environment is investigated. A stepped-frequency, instrumentation radar operating at 215 GHz capable of vertical and horizontal polarization transmission and reception is utilized to perform backscatter measurements. A portable measurement system is assembled for data collection in indoor environments. Backscatter measurements are performed at VV and HH polarizations and it is shown that images based on HH backscatter measurements provide a higher quality map of the environment with higher

sensitivity in detection of smooth walls, less multipath effects, and fewer ghost targets compared to that obtained from the vertical polarization. A full radar scan of the environment is performed at each radar location as the radar moves along the corridors of the building in order to create 2D images of the building interior. These images can be generated real time for obstacle-detection and navigation of automated robots. These images are integrated in a global coordinate frame to create a map of the interior layout of the building. A number of image processing techniques are applied to the aggregated radar map to enhance the map quality and remove the undesired effects A linear feature extraction method based on Hough transform is used to extract the rectilinear features (walls, doors, etc.) in the complete map. Algorithms are developed to eliminate the false targets resulted from multipath and beam overlap on the corners and ledges at the hallway junctions. The final radar map shows a good agreement with the actual building layout. Accurate backscattering coefficients of different indoor material have been performed and analyzed to complete the indoor phenomenology study.

CHAPTER 7
CONCLUSIONS AND FUTURE WORK

1.39 Summary and Conclusions

This thesis presented the development of passive components and structures for a low-mass, compact MMW radar operating at 240 GHz using micromachining technology as well as performance assessment of such radars for indoor navigation and mapping applications. Challenges in the development of components and structures for such high frequency applications required novel approaches in the design procedure, the fabrication process, and the measurement methodology. The design of novel components and structures that enable full integration of the MMW radar front-end is presented in Chapter 2. The structures are designed to be compatible with micromachining technology and are optimized for minimum insertion loss. The first structure is a cavity-backed CPW line (CBCBW) which is designed and optimized for minimum loss with a 50 Ω characteristic impedance. This line has less than 0.12 dB/mm loss over the entire J-band (220GHz-325GHz). The second essential structure is a transition from rectangular waveguide to CBCPW line. The transition from CBCPW to waveguide is realized in three steps to achieve a broadband response with a topology amenable to silicon micromachining. The first step is a tapered transition from the CBCPW line to a 50 Ω reduced-height waveguide. The next two steps utilize a novel in-plane impedance tapering technique to transition from the reduced-height waveguide to the on-wafer regular height waveguide. The full transition has less than 0.9 dB insertion loss and more than 13 dB return loss over the entire J-band

(39% bandwidth). The third structure is a through-wafer chip packaging configuration with an optimized transition from on-chip microstrip line to on-wafer CBCPW line to enable active chip integration. The fourth set of components are waveguide directional couplers to divide the FMCW signal between the transmit antenna and receiver mixer. Multiple apertures on the common wall between the adjacent waveguides are designed and optimized to achieve high directivity couplers over a broad frequency range.

One of the major accomplishments of this dissertation is the development of optimal microfabrication processes for realization of the micromachined radar front-end. The details of these processes are presented in Chapter 3. The designed components are fabricated on two silicon wafers using micromachining technology. The multi-step structures are implemented on one of the wafers using the DRIE process. A new process to create multi-step structures based on a glass-in-silicon reflow technique is proposed to improve the loss performance of the fabricated devices compared to the standard multi-mask method. The suspended lines and slots are implemented on the other silicon wafer. These features are patterned on a thin membrane which is released from the wafer at the final stage. The two wafers are bonded to form the complete structures using a gold-to-gold themocompression bonding technique. At each process stage, diffrenet methods have been investigated to achieve the optimal sequence of processes.

Another significant contribution of this dissertation is the development of novel measurement methods for accurate and reliable characterization of on-wafer components at MMW and higher frequencies. These new measurement methods are presented in Chapter 4. First, a waveguide probe measurement technique for characterization of two-port components is proposed. This measurement technique is used to characterize the

micromachined waveguides, CBCPW line, the waveguide to CBCPW transition and the chip transition. Then, a non-contact on-wafer S-parameter measurement technique for characterization of multi-port devices at MMW and higher frequencies is presented. The proposed method enables S-parameters measurement of multi-port micromachined devices using a two-port measurement setup. In this method, a small fraction of the signal at each waveguide port is weakly coupled to free space using a small array of reflection canceling slots which is then measured by an open-ended waveguide probe. The S-parameters of the device-under-test (DUT) are calculated from the measured signals obtained from each port and from that of a reference match waveguide. A broadband waveguide slot array antenna with high return loss is designed as a matched load to terminate all ports of the device except the input port.

In the second part of this thesis, the phenomenology of MMW radars in indoor environments is investigated. A Y-band instrumentation radar is setup to study the performance of such radars in an indoor environment. Chapter 5 presents the development of a spatial image-reject filter for incorporation in this radar. A single-face, membrane-supported, miniaturized-element frequency selective surface (MEFSS) is designed for image rejection of the upconvertor mixer. In this design, a new miniaturized-element patch-wire MEFSS configuration is proposed to select the upper-side band (USB) response of a wave radiated from an upconvertor. The MEFSS is implemented on a 10μm thick Parylene membrane. The thickness of the metallic traces is increased to reduce the conductor loss. A salient feature of this design is the low sensitivity of its frequency response to the angle of incidence and the absence of a harmonic response. This feature allows placement of the spatial filter in close proximity to radiating elements with spherical wavefronts. In Chapter

6, the polarimetric backscattering phenomenology of walls and doorways are studied to aid the design of such radar systems. Polarimetric backscatter measurements of different wall covers, such as dry-wall, concrete blocks, wood, etc., as a function of incidence angle are carried out using a network analyzer operating at J-band. The instrumentation radar is used to collect backscatter data from corridors in an indoor setting. At each radar position, radar range profiles for both vertical and horizontal polarizations as a function of angle are used to form polar images for obstacle detection. It is shown that horizontally polarized incident wave can generate higher backscatter level and less reflection from smooth walls at steep angles of incidence and thus is the preferred polarization for this application. The polar images at each location are then co-registered in a global coordinate matrix to form a complete map of the interior layout. Feature extraction and image processing methods are then applied to remove multipath and enhance the radar map of building interiors.

1.40 Future work

The future work for the MMW radar involves assembly of the complete radar and integration and testing of the radar system on micro robotic platforms. As mentioned in Chapter 4, BAE systems is developing the upconverting and downconverting modules using 50nm mHEMT technology. The 20 GHz VCO and the base band processing units are developed using CMOS technology by other research groups in University of Michigan. The main focus of the future work is the integration of the active modules and the base band processing units with the micromachined front-end to realize and test the functional radar prototype.

The current microfabrication process of the micromachined radar described in Chapter 3 involves many steps which makes it costly for mass production. It also requires constant characterization of the fabrication tools (e.g. DRIE tool, lapper) to maintain the specifications required for optimal performance of the radar components. A possible future direction for the radar project is to use casting process to mass produce the radar front-end. The idea is to make permanent glass molds of the multi-step radar structure using the glass-in-silicon reflow technique described in Chapter 3 and employ the mold to cast the radar front-end. This technique makes the radar fabrication fairly simple and highly repeatable.

As for the phenomenology study of the radar scattering MMW and sub-MMW frequency bands, we have just a scratched the surface. While radar scattering phenomenology of differenet material at lower frequency bands has been studied intensively in the literature, little has been investigated at high MMW bands and above. Dielectric constant and RCS measurement of other material and surfaces and development of theoretical models to support the imperical assessments are among the topics that can be investigated in the future.

APPENDICES

APPENDIX A

Optimal Launch Pad Design for Microstrip Lines on InP Substrate

To accurately evaluate the performance of the launch pads in an actual measurement setup, full-wave analysis of the pads fed with GSG probes is performed in HFSS (Figure A.1 (a)). Simulations show that the current design on the BAE chips (Figure A.1 (b)) has a very poor performance in the radar frequency band (RL = 5.2 dB, IL = 1.7 dB @ 240 GHz).

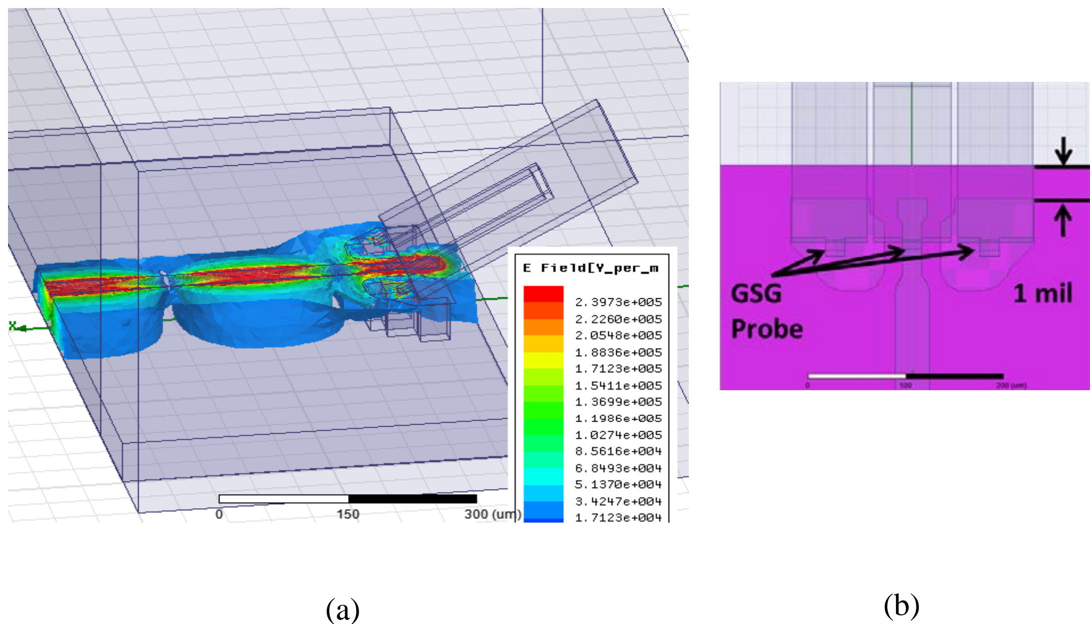

(a) (b)

Figure A.1 (a) The GSG probe fed microstrip line model in an actual setup, (b) current launch pad configurations

Reducing the distance from the backside of the chip to pads showed significant improvement in the performance of the pads. It is shown that the position of the probes on

the pads also affects the performance of return loss and insertion loss of the GSG contact (Figure A.2).

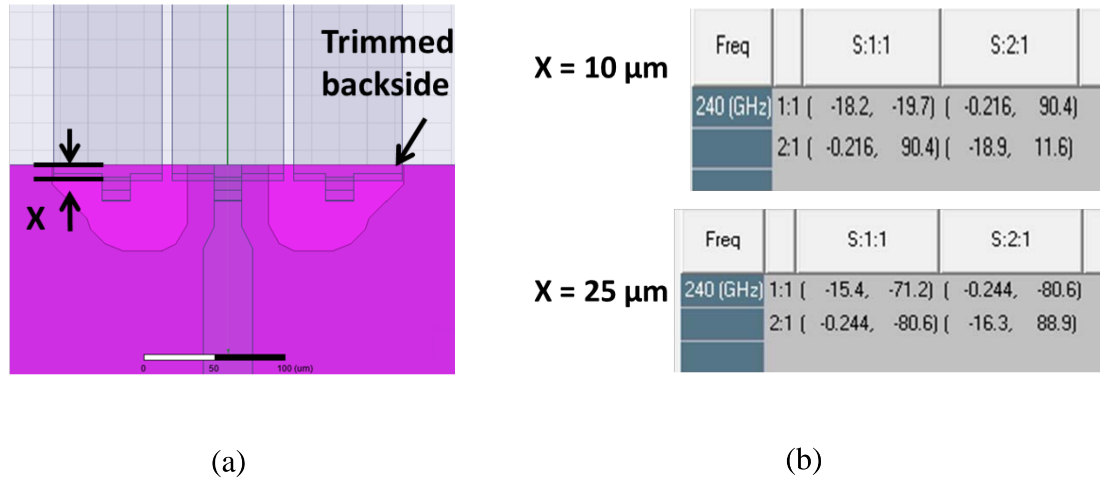

(a) (b)

Figure A.2 (a) The backside of the chip is trimmed reducing the distance to the launch pads, (b) RL and IL as a function of the distance of the tips from the edge of the chip (x)

However, the design of the transition from the pads to the microstrip line has the most effect on the performance of the insertion and return loss. The proposed tapered transition shown in Figure A.3 shows very good performance (RL = 24dB, IL=0.14 dB).

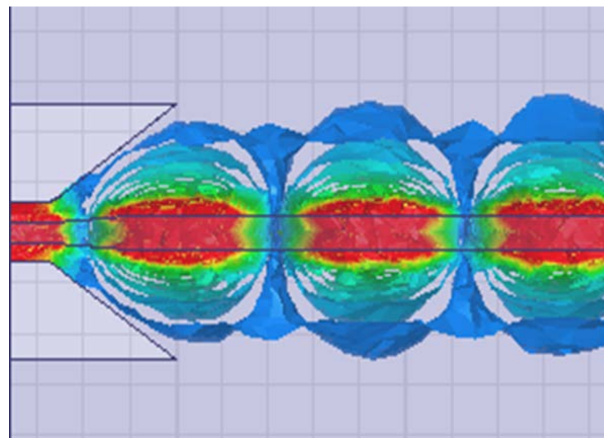

Figure A.3 The proposed tapered transition from pads to the microstrip line

After the addition of the 1 mil (25µm) distance from the chip edge to the pads which is a dicing requirement and optimization of the position of the vias under pads (Figure A.4),

the return loss and insertion loss are 19 dB and 0.18 dB which is a significant improvement to the current design. This new design will be used in the next generation of BAE chips.

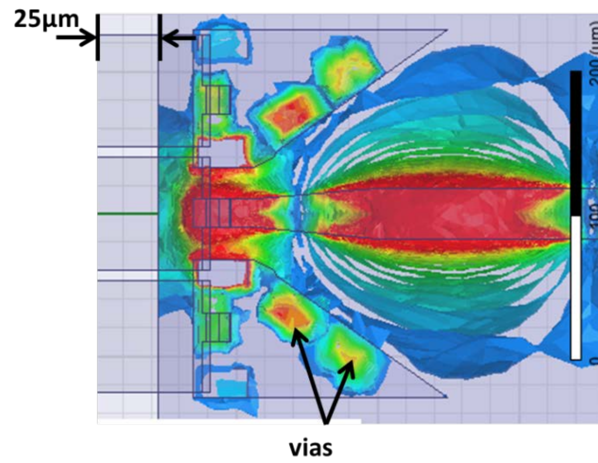

Figure A.4 The final transition design with optimum via positions

APPENDIX B

Micromachined Coupled Line Directional Coupler Fabricated on CBCPW line

In this Appendix, design of a tightly-coupled (~4.5 dB) micromachined directional coupler fabricated on CBCPW transmission line is presented. The proposed design is compatible with micromachining technology and can be integrated with active RF components through the CBCPW lines. In this design, two center strips are edge-coupled over a metallic cavity. The design criteria on impedances and phases are obtained using the traditional even- and odd-mode analysis. To achieve tight coupling, a silicon block is mounted over the coupling edge of the strips. A wiggly gap pattern is designed to change the odd-mode delay to satisfy the criterion on the phases. On-wafer matched loads have been designed and optimized to terminate the coupler ports for measurement purposes.

B.1 Design Criteria

The coupler is designed using CBCPW line structure described in Section 2.2. The two center conductors are edge coupled over the ground trench. Here, we will develop the design criteria for a coupler with arbitrary even- and odd-mode phase velocities. The cross section of the three conductor structure with the equivalent capacitance network is shown in Figure B.1.

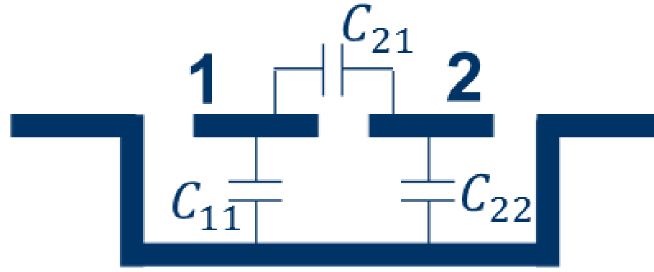

Figure B.1 The capacitance network representation of a coupled-line structure

The even- and odd-mode impedances are

$$Z_{0e} = \frac{1}{v_{pe}C_e} \quad , \quad Z_{0o} = \frac{1}{v_{po}C_o} \tag{B.1}$$

where

$$C_e = C_{11} = C_{22} \quad , \quad C_o = C_{11} + 2C_{21} \tag{B.2}$$

and v_{pe} and v_{po} are even- and odd-mode phase velocities respectively. Using the even and odd mode analysis, it can be shown that the input impedance at the ports of the coupler is

$$Z_{in} = Z_0 + \frac{2(Z_{in}^o Z_{in}^e - Z_0^2)}{Z_{in}^e + Z_{in}^o + 2Z_0} \tag{B.3}$$

where

$$Z_{in}^e = Z_{0e}\frac{Z_0 + jZ_{0e}tan\theta_e}{Z_{0e} + jZ_0 tan\theta_e} \tag{B.4}$$

$$Z_{in}^o = Z_{0o}\frac{Z_0 + jZ_{0o}tan\theta_o}{Z_{0o} + jZ_0 tan\theta_o} \tag{B.5}$$

Hence, to match the impedance at the ports ($Z_{in} = Z_0$) the following criteria should be satisfied:

$$Z_0 = \sqrt{Z_{0e}Z_{0o}} \tag{B.6}$$

$$\theta_e - \theta_o = 2n\pi, \quad n = 0, \pm 1, \pm 2, \ldots \tag{B.7}$$

It can also be shown that to achieve maximum coupling, the even-delay must be

$$\theta_e = (m + \frac{1}{2})\pi, \quad m = 0, \pm 1, \pm 2, \ldots \tag{B.8}$$

B.2 Coupling Enhancement

If Equations (B.6)-(B.8) are satisfied, then the coupling factor can be computed from

$$C = \frac{Z_{0e} - Z_{0o}}{Z_{0e} + Z_{0o}} \tag{B.9}$$

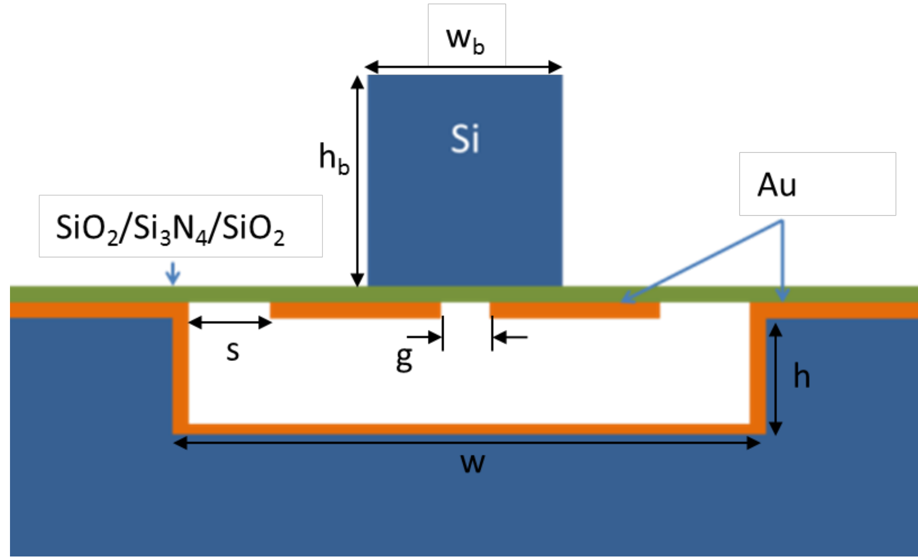

Figure B.2 Cross section of the proposed CBCPW coupler (optimized dimensions: h = 45µm, g = 5µm, w = 100µm, s = 97.5µm, $w_b = h_b$ = 50µm)

Based on Equations (B.1) and (B.2), C is maximized when the ratio of the capacitance between two strips to the capacitance of between each strip and the ground ($\frac{C_{21}}{C_{11}}$) is maximized. The capacitance between the two strips is a function of the gap size and the effective dielectric constant. The gap size cannot be made smaller than certain limit (~5 µm) due to fabrication tolerances. Analysis shows that for the configuration shown in Figure B.1, the maximum achievable coupling factor is about 17 dB for a gap size of 5µm.

To achieve a tight coupling, the structure shown in Figure B.2 is proposed where a silicon block is placed over the gap area. The silicon block (ε=12) on top of the gap increases the effective dielectric constant for the odd-mode (ε^{o}_{eff}) and does not change the even-mode effective dielectric constant (ε^{e}_{eff}). This is expected since for the even-mode the electric field is mostly in the air and as a result the effective dielectric constant is near 1 (Figure B.3 (a)). However, for the odd-mode the field is concentrated in the silicon (and membrane) and this increases the effective dielectric constant (Figure B.3 (b)).

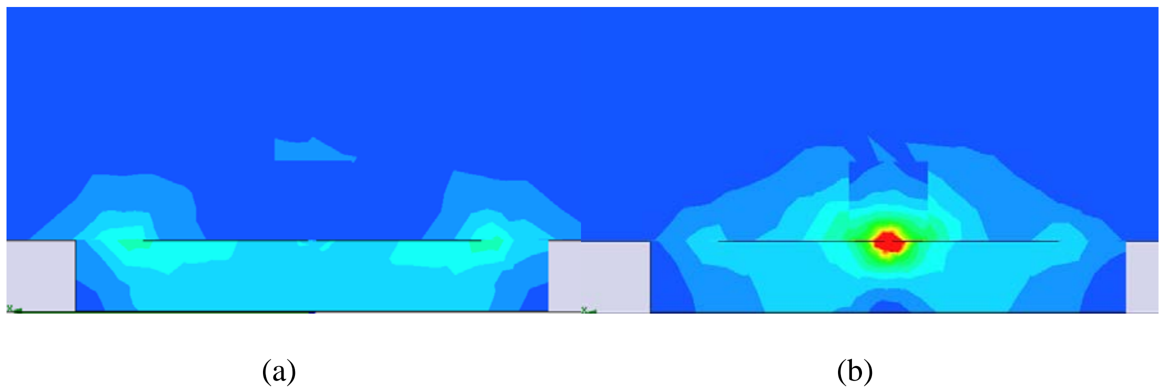

(a) (b)

Figure B.3 Electric field distribution in the proposed coupler structure (a) even mode, (b) odd mode

This increases the coupling factor to 4.4 dB for the same gap size. The even- and odd-mode characteristics of the proposed structure with and without the silicon block are shown in Table B.1.

Table B.1 Even- and odd-mode characteristics of the proposed coupler

	g (μm)	$\varepsilon_{eff,o}$	$\varepsilon_{eff,e}$	$v_{p,o}$ (m/s)	$v_{p,e}$ (m/s)	C (dB)
Without silicon block	5	1.18	1.06	2.85e8	2.91e8	17

With silicon block	5	3.81	1.07	1.54e8	2.90e8	4.4

The cross section dimensions of the structure are optimized to achieve the first criteria for perfect matching at the ports (Equation (B.6)). The optimized dimensions are shown in Figure B.2.

B.3 Phase Matching

To achieve phase matching, the length of the coupler should be designed such that the electrical lengths of the even and odd modes satisfy the Equations (B.7) and (B.8) simultaneously. In conventional coupled line designs where the phase velocity of both modes are approximately equal, the coupled lines are typically quarter-wavelength long for which $\theta_e = \theta_o = 90^{\circ}$. However, in the proposed structure, the phase velocity of the even mode is much higher than that of the odd mode ($v_{p,e} > v_{p,o}$) due to the presence of the silicon block. It can be shown that Equations (B.7) and (B.8) cannot be satisfied simultaneously for any given coupled line length. For example, by choosing the length of the coupler $l = \frac{3}{4}\lambda_e = 917\mu m$, Equation (B.8) is satisfied but the phase difference between the even- and odd-mode is $\theta_e - \theta_o = 240^{\circ}$.

To circumvent this difficulty there should also be an electrical delay between the even and odd modes. This is realized by zigzaging the edge of the coupled lines facing each other. The wiggly gap creates a longer propagation path for the odd mode and has been previously considered for making broadband microstrip couplers [104, 105]. The proposed wiggly gap design is shown in Figure B.4. The dimensions of the wiggle pattern are optimized so that the two modes arrive in phase:

$$\theta_e - \theta_o = 360^{\circ} \tag{B.10}$$

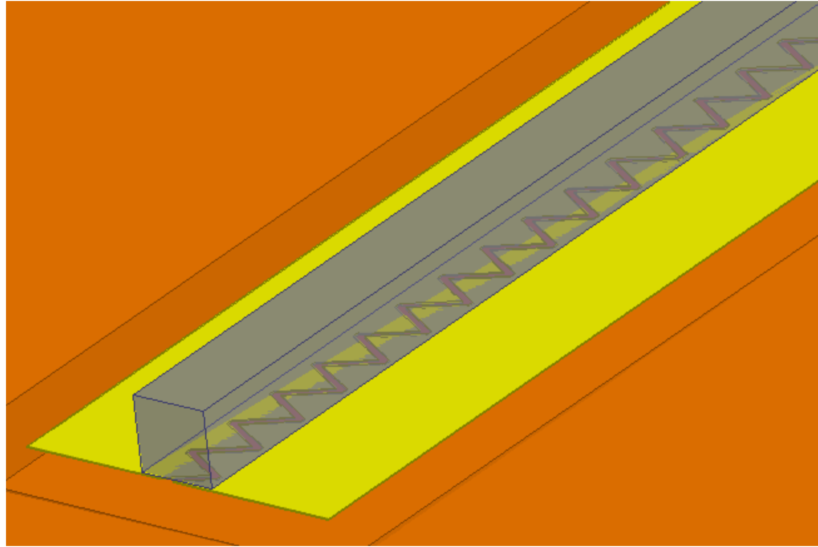

Figure B.4 Zigzag edge of the coupled line to create longer propagation path for the odd mode

B.4 Connection to CBCPW

The final step in the coupler design is to connect the ports to the 50 Ω CBCPW line. Considering that the width of 50 Ω CBCPW line is 210μm, a direct connection to the 100μm wide coupled line strips is not feasible. Connecting the ports to CBCPW line at angles would also introduce significant parasitics which deteriorates the performance of the coupler.

To solve this issue, half-wavelength long line sections are inserted between the coupler ports and the 50Ω CBCPW lines. This ensures a perfect impedance match between the ports and the CBCPW line while introducing minimum parasitics. The complete coupler structure with port connections to CBCPW lines is shown in Figure B.5.

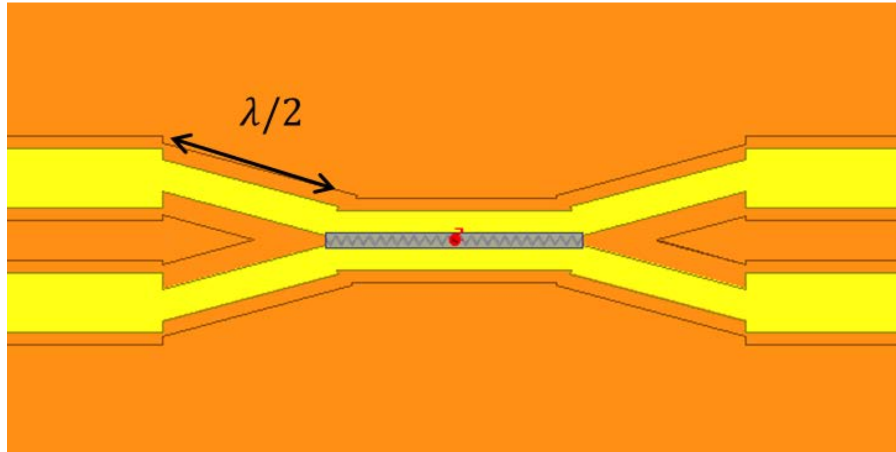

Figure B.5 The micromachined coupler with port connections to CBCPW

Full-wave analysis of the proposed coupler is performed in HFSS. The coupler has less than 4.6 dB of coupling and more than 20 dB of return loss and isolation over the 230-245 GHz band (see Figure B.6).

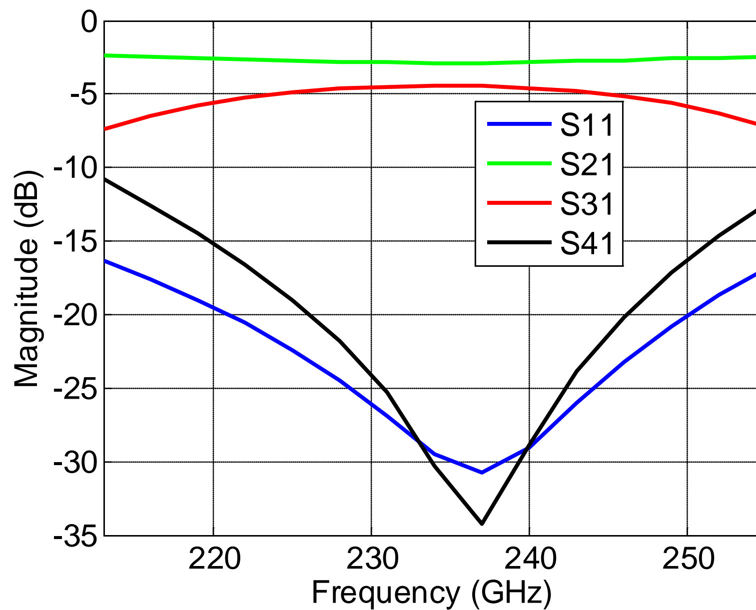

Figure B.6 Simulated performance of the micromachined coupler

B.5 On-Wafer Matched Load

To fully characterize the designed directional coupler, three independent measurements, namely through, coupled, and isolated, need to be performed. To perform each of these measurements using a two-port network analyzer, two ports should be terminated with a perfect matched load.

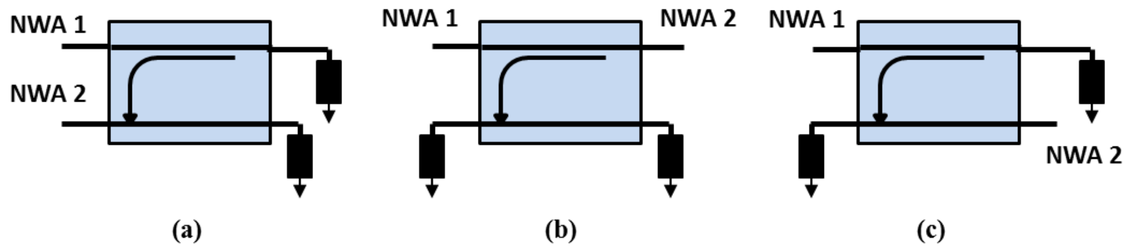

Figure B.7 Measurement configurations for full characterization of directional couplers; (a) coupled (b) through (c) isolated

Thin films of lossy metals and lightly doped substrate layers (e.g. GaAs) are among two common RF resistors used in MMIC design [106, 107]. Thin film resistors are preferred since they are temperature-stable and have smaller parasitics. The process of making these thin films involves highly controlled deposition of metals such as NiCr or TaN onto the substrate. In millimeter-wave frequency range, these resistors have shown good performance up to 60 GHz [86]. We investigated the impedance and return loss of thin films of different material with different dimensions and the results are listed in Table B.2.

As can be seen, the reactance of the load increases as a function of frequency. For high resistivity material (e.g. graphite), the reactance is small enough to achieve a good matching (19 dB return loss). For this application, the film material deposition should be compatible with the coupler fabrication process. The 500 A° thick Titanium film (with sheet resistivity of 11 Ω/sq) which is already used as gold adhesion in the microfabrication

process of the coupler can be utilized as thin film resistors. However, as indicated in Table B.2, the reactance for such film is significant and the return loss is below 10 dB.

Table B.2 Return loss and impedances of various thin film resistances

Load type	Frequency (GHz)	S11(dB)	Impedance (Ω)
Graphite (7e4 S/m) (70um*45um*0.1um)	60	-31	50.2-2.6i
Sheet resistance (11 Ω /sq) (45um*5um)	60	22.2	55.4+5.6i
Graphite (7e4 S/m) (70um*45um*0.1um)	245	-19	48.7-10.9i
Sheet resistance (11 Ω /sq) (45um*5um)	245	-7.2	123+4.7i
Sheet resistance (11 Ω /sq) (45um*10um)	245	-9	35+27.7i

To solve this problem, we propose a matched load design shown in Figure B.8. In this design, the CBCPW line is terminated with two parallel lossy slot lines. The characteristic impedance of the lossy line has a capacitive imaginary part which creates a mismatch at the junction:

$$Z_0 = \sqrt{\frac{R + j\omega l}{G + j\omega C}} = Z_r - jZ_I \tag{B.11}$$

To compensate for this reactance, two short stubs are implemented at the junctions. These short stubs can be modeled as resistors in series with an inductor. By optimizing the dimensions, the reactance can be cancelled to achieve return loss of more than 25 dB in the 100 GHz to 300 GHz range.

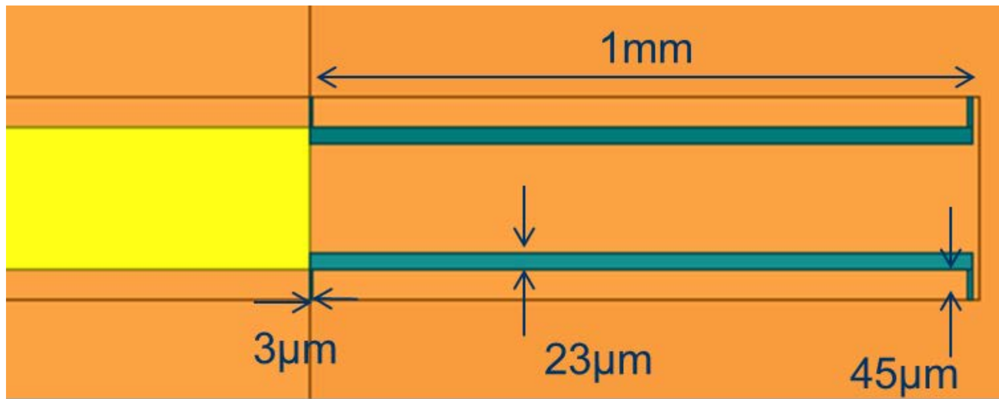

Figure B.8 The proposed matched load design

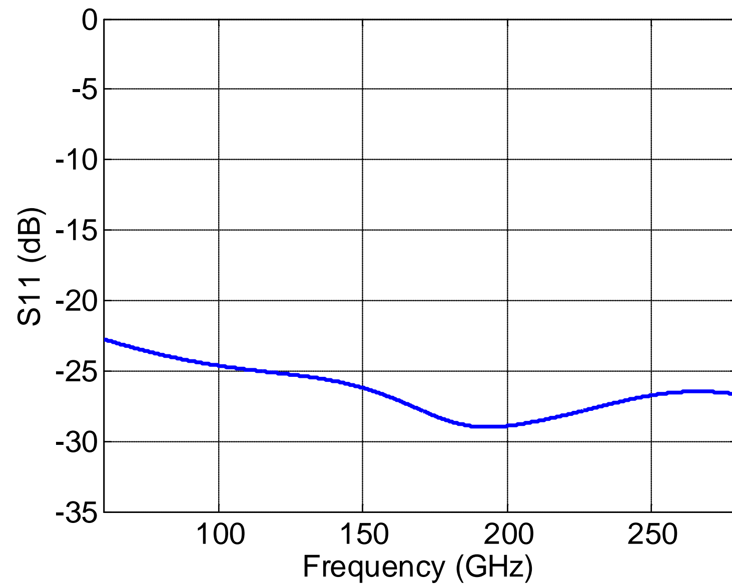

Figure B.9 Simulated return loass of the optimized matched load

APPENDIX C

Ka-Band Bandpass MEFSS and Polarizer

In this Appendix, a new single-face MEFSS structure consisting of loop and patch arrays is proposed to achieve a single passband and a transmission zero at a lower frequency. Then a Ka-band MEFSS and polarizer are designed and implemented on a single substrate. At the end, the designed structure is fabricated and its performance is verified experimentally.

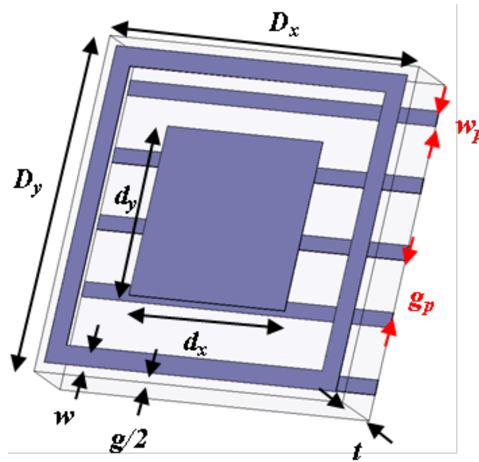

Figure C.1 Unit cell of the MEFSS/polarizer structure (Dx = Dy = 4.5mm, dx = dy = 265mm, w = 254µm, g = 254µm, t = 787µm, wp = 0.2mm, gp = 0.7mm)

C.1 Design and Model Verification

The proposed structure consists of two printed layers separated by a dielectric substrate (Figure C.1). On one surface, a 2D periodic array of patches and square loops are implemented to create the desired bandpass filter. It can be shown that interaction of a loop array with incident EM wave can be modeled as a series LC branch. This series LC branch resonant frequency creates a transmission zero in the frequency response of the FSS. Hence, the transmission zero frequency is independent of the patch dimensions. The

patch array can be modeled as a capacitor which is in parallel with the loop series LC branch.

The equivalent circuit model is shown in Figure 5.5 and the pole and zero frequencies are given by Equations 5.1 and 5.2.

On the other surface of the substrate, a wire-grid polarizer has been implemented. Dimensions of the wire-grid (w_p, g_p) are optimized so that total transmission of one of the polarizations (TE or TM) and total reflection of the other polarization are achieved in the radar passband.

A full wave analysis of the FSS structure has been performed using Ansoft HFSS to verify the performance of the proposed structure. As can be seen in Figure C.2, the result of the circuit model simulation is in a very good agreement with the full wave analysis results.

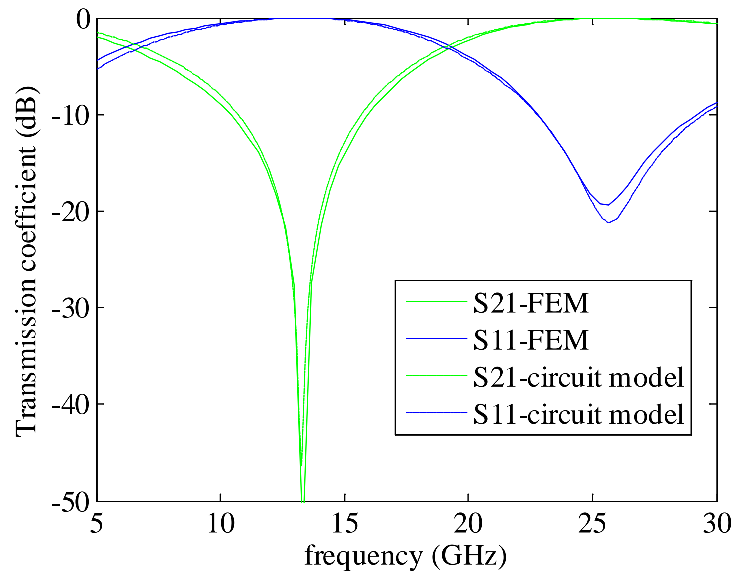

Figure C.2 Numerical simulations of the patch-loop MEFSS

To verify the performance of the combined polarizer and MEFSS, full wave analysis of the complete structure has been performed for both TE and TM polarizations. The selectivity between the two polarizations is more than 20 dB as shown in Figure C.3.

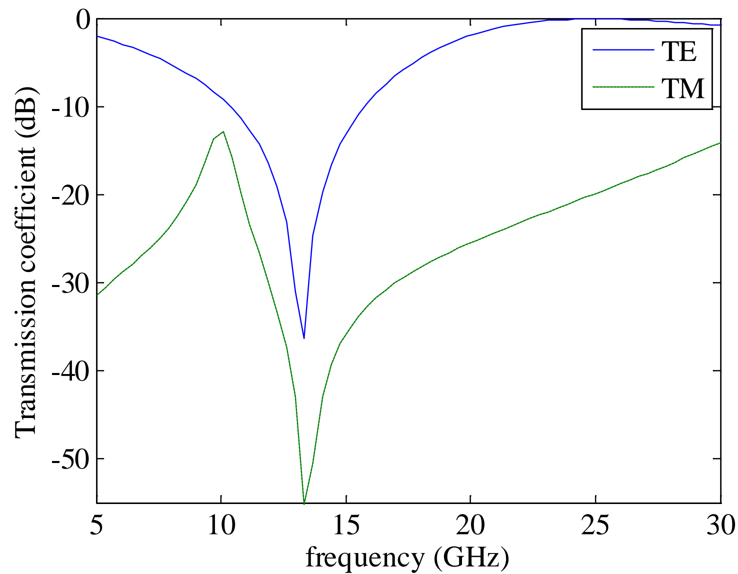

Figure C.3 Full-wave simulation of the combined polarizer and MEFSS for TE and TM polarizations

C.2 Experimental Verification

To verify the simulation results, a 6”×6” prototype of the structure is fabricated and tested using a free-space measurement setup. The structure is fabricated on a 31 mil Duroid 5880 substrate (ε_r=2.2) with ¼ oz. electrodeposited copper foil. To achieve high accuracy for the dimensions of the elements, a thin layer of spin-on photoresist has been utilized, instead of photosensitive laminates, to pattern the copper. The patterned substrate is then etched using standard printed circuit board wet etching process. The fabricated prototype is shown in Figure C.4.

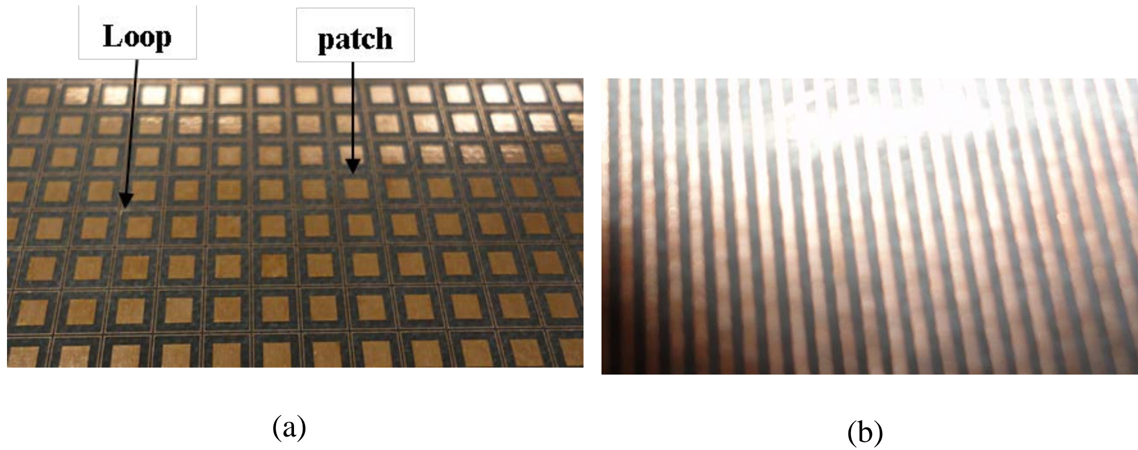

Figure C.4 Fabricated structure (a) patch-loop MEFSS (b) wire-grid polarizer

A free space measurement setup has been utilized to test the performance of the fabricated prototype. The setup consists of a lens-horn as the transmitting antenna for creation of collimated beam and a high gain horn as the receiving antenna at far-field (Figure C.5).

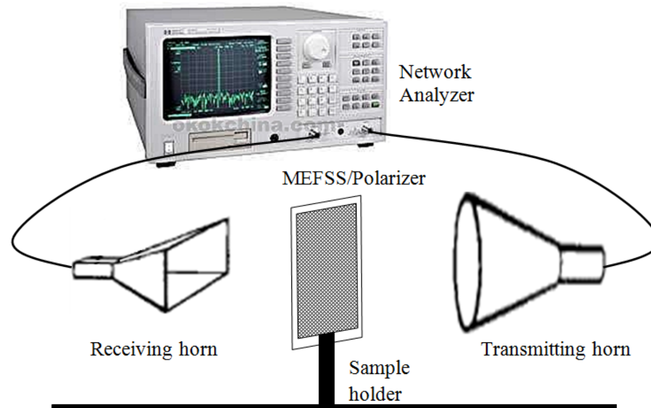

Figure C.5 Ka-band free space measurement setup

The measurement results are shown in Figure C.6. A good agreement between simulation and measurement results can be observed. The measured results show less than 0.5 dB insertion loss in the passband and more than 20 dB rejection in the stopband.

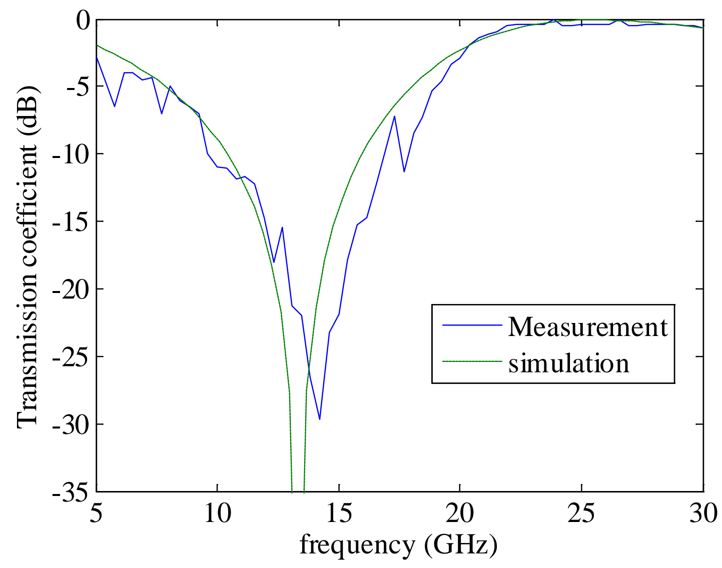

Figure C.6 Measured and simulated responses of the MEFSS structure

BIBLIOGRAPHY

[1] J. S. Humbert, I. Chopra, R. S. Fearing, R. J. Full, R. J. Wood, and M. H. Dickinson, "Development of micromechanics for micro-autonomous systems (ARL-MAST CTA Program)," 2009, pp. 73180L-73180L-6.

[2] X. Deng, L. Schenato, W. C. Wu, and S. S. Sastry, "Flapping flight for biomimetic robotic insects: Part I-system modeling," *IEEE Transactions on Robatics,* vol. 22, pp. 776-788, 2006.

[3] G. T. Sibley, M. H. Rahimi, and G. S. Sukhatme, "Robomote: A tiny mobile robot platform for large-scale ad-hoc sensor networks," in *Robotics and Automation, 2002. Proceedings. ICRA'02. IEEE International Conference on*, 2002, pp. 1143-1148.

[4] I. Kroo, F. Prinz, M. Shantz, P. Kunz, G. Fay, S. Cheng*, et al.*, "The Mesicopter: A miniature rotorcraft concept–phase ii interim report," ed: Stanford university, USA, 2000.

[5] A. M. Hoover, E. Steltz, and R. S. Fearing, "RoACH: An autonomous 2.4 g crawling hexapod robot," in *Intelligent Robots and Systems, 2008. IROS 2008. IEEE/RSJ International Conference on*, 2008, pp. 26-33.

[6] *http://en.wikipedia.org/wiki/Inertial_navigation_system*.

[7] N. Yazdi, F. Ayazi, and K. Najafi, "Micromachined inertial sensors," *Proceedings of the IEEE,* vol. 86, pp. 1640-1659, 1998.

[8] R. Jarvis, "A laser time-of-flight range scanner for robotic vision," *Pattern Analysis and Machine Intelligence, IEEE Transactions on,* pp. 505-512, 1983.

[9] M. J. Brownlow, "A time-of-flight optical range sensor for mobile robot navigation," University of Oxford, 1993.

[10] O. Partaatmadja, B. Benhabib, A. Sun, and A. Goldenberg, "An electrooptical orientation sensor for robotics," *Robotics and Automation, IEEE Transactions on,* vol. 8, pp. 111-119, 1992.

[11] M. U. de Haag, D. Venable, and M. Smearcheck, "Use of 3D laser radar for navigation of unmanned aerial and ground vehicles in urban and indoor environments," in *Defense and Security Symposium*, 2007, pp. 65500C-65500C-12.

[12] D. Nitzan, A. E. Brain, and R. O. Duda, "The measurement and use of registered reflectance and range data in scene analysis," *Proceedings of the IEEE,* vol. 65, pp. 206-220, 1977.

[13] T.-H. Ngo, C.-H. Kim, Y. J. Kwon, J. S. Ko, D.-B. Kim, and H.-H. Park, "Wideband Receiver for a Three-Dimensional Ranging LADAR System," 2012.

[14] A. El Gamal and H. Eltoukhy, "CMOS image sensors," *Circuits and Devices Magazine, IEEE,* vol. 21, pp. 6-20, 2005.

[15] C. Niclass, M. Soga, H. Matsubara, S. Kato, and M. Kagami, "A 100-m Range 10-Frame/s 340 96-Pixel Time-of-Flight Depth Sensor in 0.18-CMOS," 2013.

[16] S. Kurtti and J. Kostamovaara, "An integrated laser radar receiver channel utilizing a time-domain walk error compensation scheme," *Instrumentation and Measurement, IEEE Transactions on,* vol. 60, pp. 146-157, 2011.

[17] R. Moss, P. Yuan, X. Bai, E. Quesada, R. Sudharsanan, B. L. Stann*, et al.*, "Low-cost compact MEMS scanning ladar system for robotic applications," in *SPIE Defense, Security, and Sensing*, 2012, pp. 837903-837903-9.

[18] R. Sudharsanan and R. Moss. (2013) Low cost scanning LiDAR imager. *LiDAR News eMagazine*.

[19] M. Ijaz, Z. Ghassemlooy, J. Pesek, O. Fiser, H. Le Minh, and E. Bentley, "Modeling of Fog and Smoke Attenuation in Free Space Optical Communications Link Under Controlled Laboratory Conditions," *Journal of Lightwave Technology,* vol. 31, pp. 1720-1726, 2013.

[20] E. Araujo and R. A. Grupen, "Feature extraction for autonomous navigation using an active sonar head," in *Robotics and Automation, 2000. Proceedings. ICRA'00. IEEE International Conference on*, 2000, pp. 3823-3828.

[21] J. Steckel, A. Boen, and H. Peremans, "Broadband 3-D Sonar System Using a Sparse Array for Indoor Navigation," 2012.

[22] J. H. Ko, W. J. Kim, and M. J. Chung, "A method of acoustic landmark extraction for mobile robot navigation," *Robotics and Automation, IEEE Transactions on,* vol. 12, pp. 478-485, 1996.

[23] "Ultrasonic Ranging System ", ed. Polaroid Corporation Commercial Battery Division, Cambridge, MA, 1984.

[24] "Ultrasonic Displacement Sensors for Distances up to 5000 mm," ed, 1994.

[25] M. D. Adams, "Coaxial range measurement-current trends for mobile robotic applications," *Sensors Journal, IEEE,* vol. 2, pp. 2-13, 2002.

[26] *Micron Sonar-Ultra Compact Imaging Sonar*.

[27] T. Deissler and J. Thielecke, "UWB SLAM with Rao-Blackwellized Monte Carlo data association," in *Indoor Positioning and Indoor Navigation (IPIN), 2010 International Conference on*, 2010, pp. 1-5.

[28] C. Zhang, M. J. Kuhn, B. C. Merkl, A. E. Fathy, and M. R. Mahfouz, "Real-time noncoherent UWB positioning radar with millimeter range accuracy: Theory and experiment," *Microwave Theory and Techniques, IEEE Transactions on,* vol. 58, pp. 9-20, 2010.

[29] B. Yamauchi, "Daredevil: Ultra wideband radar sensing for small UGVs," in *Proc. SPIE*, 2007, p. 65610B.

[30] I. Kallfass, J. Antes, T. Schneider, F. Kurz, D. Lopez-Diaz, S. Diebold*, et al.*, "All active MMIC-based wireless communication at 220 GHz," *Terahertz Science and Technology, IEEE Transactions on,* vol. 1, pp. 477-487, 2011.

[31] T.-Y. Kao, Y. Yan, T.-M. Shen, A.-K. Chen, and J. Lin, "Design and Analysis of a 60-GHz CMOS Doppler Micro-Radar System-in-Package for Vital-Sign and Vibration Detection," 2013.

[32] F. Rodriguez-Morales, K. S. Yngvesson, R. Zannoni, E. Gerecht, D. Gu, X. Zhao*, et al.*, "Development of integrated HEB/MMIC receivers for near-range terahertz imaging," *Microwave Theory and Techniques, IEEE Transactions on,* vol. 54, pp. 2301-2311, 2006.

[33] T. Mitomo, N. Ono, H. Hoshino, Y. Yoshihara, O. Watanabe, and I. Seto, "A 77 GHz 90 nm CMOS transceiver for FMCW radar applications," *Solid-State Circuits, IEEE Journal of,* vol. 45, pp. 928-937, 2010.

[34] P.-N. Chen, P.-J. Peng, C. Kao, Y.-L. Chen, and J. Lee, "A 94GHz 3D-image radar engine with 4TX/4RX beamforming scan technique in 65nm CMOS," in *Solid-State Circuits Conference Digest of Technical Papers (ISSCC), 2013 IEEE International*, 2013, pp. 146-147.

[35] J. Lee, Y.-A. Li, M.-H. Hung, and S.-J. Huang, "A fully-integrated 77-GHz FMCW radar transceiver in 65-nm CMOS technology," *Solid-State Circuits, IEEE Journal of,* vol. 45, pp. 2746-2756, 2010.

[36] M. Vahidpour, "A Millimeter-Wave Radar Microfabrication Technique and Its Application in Detection of Concealed Objects," The University of Michigan, 2012.

[37] M. Lange and J. Detlefsen, "94 GHz three-dimensional imaging radar sensor for autonomous vehicles," *Microwave Theory and Techniques, IEEE Transactions on,* vol. 39, pp. 819-827, 1991.

[38] M. Rangwala, F. Wang, and K. Sarabandi, "Study of millimeter-wave radar for helicopter assisted landing system," in *Geoscience and Remote Sensing Symposium, 2007. IGARSS 2007. IEEE International*, 2007, pp. 777-780.

[39] F. Sadjadi, M. Helgeson, M. Radke, and G. Stein, "Radar synthetic vision system for adverse weather aircraft landing," *Aerospace and Electronic Systems, IEEE Transactions on,* vol. 35, pp. 2-14, 1999.

[40] L. Jiuming and L. Jingqing, "Millimeter-wave radar application in tracking maneuvering target," in *Radar, 2006. CIE'06. International Conference on*, 2006, pp. 1-4.

[41] Y. Kuga, A. Nashashibi, and F. T. Ulaby, "Clutter measurements by millimeter-wave radars," in *Telesystems Conference, 1991. Proceedings. Vol. 1., NTC'91., National*, 1991, pp. 347-351.

[42] M. Vahidpour and K. Sarabandi, "Millimeter-wave doppler spectrum and polarimetric response of walking bodies," *Geoscience and Remote Sensing, IEEE Transactions on,* vol. 50, pp. 2866-2879, 2012.

[43] R. Appleby and R. N. Anderton, "Millimeter-wave and submillimeter-wave imaging for security and surveillance," *Proceedings of the IEEE,* vol. 95, pp. 1683-1690, 2007.

[44] K. B. Cooper, R. J. Dengler, N. Llombart, T. Bryllert, G. Chattopadhyay, E. Schlecht*, et al.*, "Penetrating 3-D imaging at 4-and 25-m range using a submillimeter-wave radar," *Microwave Theory and Techniques, IEEE Transactions on,* vol. 56, pp. 2771-2778, 2008.

[45] D. Wikner, "Millimeter-wave propagation measurement through a dust tunnel," DTIC Document2008.

[46] H. J. Liebe, T. Manabe, and G. A. Hufford, "Millimeter-wave attenuation and delay rates due to fog/cloud conditions," *Antennas and Propagation, IEEE Transactions on,* vol. 37, pp. 1617-1612, 1989.

[47] J. Papapolymerou, J. East, and L. P. Katehi, "GaAs versus quartz FGC lines for MMIC applications," *Microwave Theory and Techniques, IEEE Transactions on,* vol. 46, pp. 1790-1793, 1998.

[48] G. E. Ponchak, I. K. Itotia, and R. F. Drayton, "Propagation characteristics of finite ground coplanar waveguide on Si substrates with porous Si and polyimide interface layers," in *Microwave Conference, 2003. 33rd European*, 2003, pp. 45-48.

[49] K. J. Herrick, T. A. Schwarz, and L. P. Katehi, "Si-micromachined coplanar waveguides for use in high-frequency circuits," *Microwave Theory and Techniques, IEEE Transactions on,* vol. 46, pp. 762-768, 1998.

[50] W. Y. Liu, D. Steenson, and M. B. Steer, "Membrane-supported CPW with mounted active devices," *Microwave and Wireless Components Letters, IEEE,* vol. 11, pp. 167-169, 2001.

[51] A. Dehe, H. Klingbeil, C. Weil, and H. Hartnagel, "Membrane-supported coplanar waveguides for MMIC and sensor application," *Microwave and Guided Wave Letters, IEEE,* vol. 8, pp. 185-187, 1998.

[52] T. M. Weller, L. P. Katehi, and G. M. Rebeiz, "High performance microshield line components," *Microwave Theory and Techniques, IEEE Transactions on,* vol. 43, pp. 534-543, 1995.

[53] G. E. Ponchak, A. N. Downey, and L. P. Katehi, "High frequency interconnects on silicon substrates," in *Radio Frequency Integrated Circuits (RFIC) Symposium, 1997., IEEE*, 1997, pp. 101-104.

[54] M. Moallem, J. R. East, and K. Sarabandi, "A broadband, micromachined rectangular waveguide to cavity-backed coplanar waveguide transition using impedance-taper technique," *Terahertz Science and Technology, IEEE Transactions on,* 2014.

[55] M. Moallem, J. East, and K. Sarabandi, "Optimally designed membrane-supported grounded CPW structure for submillimeter-wave applications," in *Antennas and Propagation Society International Symposium, 2009. APSURSI'09. IEEE*, 2009, pp. 1-4.

[56] A. F. Peterson, S. L. Ray, and R. Mittra, *Computational methods for electromagnetics* vol. 24: IEEE press New York, 1998.

[57] Y. Li, B. Pan, C. Lugo, M. Tentzeris, and J. Papapolymerou, "Design and Characterization of a W-band micromachined cavity filter including a novel integrated transition from CPW feeding lines," *Microwave Theory and Techniques, IEEE Transactions on,* vol. 55, pp. 2902-2910, 2007.

[58] Y. Lee, J. P. Becker, J. R. East, and L. P. Katehi, "Fully micromachined finite-ground coplanar line-to-waveguide transitions for W-band applications," *Microwave Theory and Techniques, IEEE Transactions on,* vol. 52, pp. 1001-1007, 2004.

[59] Y. Li, B. Pan, M. M. Tentzeris, and J. Papapolymerou, "A fully micromachined W-band coplanar waveguide to rectangular waveguide transition," in *Microwave Symposium, 2007. IEEE/MTT-S International*, 2007, pp. 1031-1034.

[60] M. Vahidpour and K. Sarabandi, "2.5 D Micromachined 240 GHz Cavity-Backed Coplanar Waveguide to Rectangular Waveguide Transition," *Terahertz Science and Technology, IEEE Transactions on,* vol. 2, pp. 315-322, 2012.

[61] H.-W. Yao, A. Abdelmonem, J.-F. Liang, and K. A. Zaki, "Analysis and design of microstrip-to-waveguide transitions," *Microwave Theory and Techniques, IEEE Transactions on,* vol. 42, pp. 2371-2380, 1994.

[62] Y. Ding and K. Wu, "Substrate integrated waveguide-to-microstrip transition in multilayer substrate," *Microwave Theory and Techniques, IEEE Transactions on,* vol. 55, pp. 2839-2844, 2007.

[63] D. Deslandes and K. Wu, "Integrated microstrip and rectangular waveguide in planar form," *Microwave and Wireless Components Letters, IEEE,* vol. 11, pp. 68-70, 2001.

[64] X. Shang, M. Ke, Y. Wang, and M. J. Lancaster, "WR-3 Band Waveguides and Filters Fabricated Using SU8 Photoresist Micromachining Technology," 2012.

[65] R. Levy, "Analysis and synthesis of waveguide multiaperture directional couplers," *Microwave Theory and Techniques, IEEE Transactions on,* vol. 16, pp. 995-1006, 1968.

[66] T. Sieverding, U. Papziner, and F. Arndt, "Mode-matching CAD of rectangular or circular multiaperture narrow-wall couplers," *Microwave Theory and Techniques, IEEE Transactions on,* vol. 45, pp. 1034-1040, 1997.

[67] S. Miller and W. Mumford, "Multi-element directional couplers," *Proceedings of the IRE,* vol. 40, pp. 1071-1078, 1952.

[68] R.-U. Haque and K. D. Wise, "A Glass-in-Silicon Reflow Process for Three-Dimensional Microsystems."

[69] D. K. Sparacin, S. J. Spector, and L. C. Kimerling, "Silicon waveguide sidewall smoothing by wet chemical oxidation," *Journal of Lightwave Technology,* vol. 23, p. 2455, 2005.

[70] C. H. Tsau, S. M. Spearing, and M. A. Schmidt, "Characterization of wafer-level thermocompression bonds," *Microelectromechanical Systems, Journal of,* vol. 13, pp. 963-971, 2004.

[71] S. X. Jia, J. Wu, J. Zhu, and Y. X. Wang, "Study on the Gold-Gold Thermocompression Bonding for Wafer-Level Packaging," *Advanced Materials Research,* vol. 60, pp. 325-329, 2009.

[72] J. W. Digby, C. E. McIntosh, G. M. Parkhurst, B. M. Towlson, S. Hadjiloucas, J. W. Bowen*, et al.*, "Fabrication and characterization of micromachined rectangular waveguide components for use at millimeter-wave and terahertz frequencies," *Microwave Theory and Techniques, IEEE Transactions on,* vol. 48, pp. 1293-1302, 2000.

[73] J. Hu, S. Xie, and Y. Zhang, "Micromachined Terahertz Rectangular Waveguide Bandpass Filter on Silicon-Substrate," 2012.

[74] Y. Li, P. L. Kirby, O. Offranc, and J. Papapolymerou, "Silicon micromachined W-band hybrid coupler and power divider using DRIE technique," *Microwave and Wireless Components Letters, IEEE,* vol. 18, pp. 22-24, 2008.

[75] M. Vahidpour and K. Sarabandi, "Micromachined J-band rectangular waveguide filter," in *General Assembly and Scientific Symposium, 2011 XXXth URSI*, 2011, pp. 1-4.

[76] K. M. Leong, K. Hennig, C. Zhang, R. N. Elmadjian, Z. Zhou, B. S. Gorospe*, et al.*, "WR1. 5 silicon micromachined waveguide components and active circuit integration methodology," *Microwave Theory and Techniques, IEEE Transactions on,* vol. 60, pp. 998-1005, 2012.

[77] T. Jamneala, P. D. Bradley, and D. A. Feld, "Employing a ground model to accurately characterize electronic devices measured with GSG probes," *Microwave Theory and Techniques, IEEE Transactions on,* vol. 52, pp. 640-645, 2004.

[78] A. Fung, D. Dawson, L. Samoska, K. Lee, T. Gaier, P. Kangaslahti*, et al.*, "Two-port vector network analyzer measurements in the 218–344-and 356–500-GHz frequency bands," *Microwave Theory and Techniques, IEEE Transactions on,* vol. 54, pp. 4507-4512, 2006.

[79] T. J. Reck, L. Chen, C. Zhang, A. Arsenovic, C. Groppi, A. W. Lichtenberger*, et al.*, "Micromachined probes for submillimeter-wave on-wafer measurements—Part I: Mechanical design and characterization," *Terahertz Science and Technology, IEEE Transactions on,* vol. 1, pp. 349-356, 2011.

[80] H. Atasoy, M. Unlu, K. Topalli, I. Istanbulluoglu, E. Temocin, O. Bayraktar*, et al.*, "Investigation of On-Wafer TRL Calibration Accuracy Dependence on Transitions and Probe Positioning," in *Microwave Conference, 2006. 36th European*, 2006, pp. 1582-1585.

[81] D. F. Williams, "500 GHz–750 GHz Rectangular-Waveguide Vector-Network-Analyzer Calibrations," *Terahertz Science and Technology, IEEE Transactions on,* vol. 1, pp. 364-377, 2011.

[82] E. C. Jameson, *Electrical discharge machining*: SME, 2001.

[83] D. Xu, W. M. Kong, X. Yang, L. Mohnkern, P. Seekell, K. Duh*, et al.*, "50-nm Metamorphic High-Electron-Mobility Transistors With High Gain and High Breakdown Voltages," *Electron Device Letters, IEEE,* vol. 30, pp. 793-795, 2009.

[84] D. Xu, X. Yang, P. Seekell, L. Mohnkern, K. Chu, R. Stedman*, et al.*, "50-nm Asymmetrically Recessed Metamorphic High-Electron Mobility Transistors With

Reduced Source–Drain Spacing: Performance Enhancement and Tradeoffs," *Electron Devices, IEEE Transactions on,* vol. 59, pp. 128-138, 2012.

[85] G. Prigent, E. Rius, H. Happy, K. Blary, and S. Lepilliet, "Design of branch-line coupler in the G-frequency band," in *Microwave Conference, 2006. 36th European*, 2006, pp. 1296-1299.

[86] S. V. Robertson, A. R. Brown, L. P. Katehi, and G. M. Rebeiz, "A 10-60-GHz micromachined directional coupler," *Microwave Theory and Techniques, IEEE Transactions on,* vol. 46, pp. 1845-1849, 1998.

[87] A. Lewandowski, D. F. Williams, P. D. Hale, J. C. Wang, and A. Dienstfrey, "Covariance-based vector-network-analyzer uncertainty analysis for time-and frequency-domain measurements," *Microwave Theory and Techniques, IEEE Transactions on,* vol. 58, pp. 1877-1886, 2010.

[88] M. Stickel, P. Kremer, and G. V. Eleftheriades, "A millimeter-wave bandpass waveguide filter using a width-stacked silicon bulk micromachining approach," *Microwave and Wireless Components Letters, IEEE,* vol. 16, pp. 209-211, 2006.

[89] F. Aryanfar and K. Sarabandi, "Characterization of semilumped CPW elements for millimeter-wave filter design," *Microwave Theory and Techniques, IEEE Transactions on,* vol. 53, pp. 1288-1293, 2005.

[90] R. Dickie, R. Cahill, H. S. Gamble, V. F. Fusco, A. G. Schuchinsky, and N. Grant, "Spatial demultiplexing in the submillimeter wave band using multilayer free-standing frequency selective surfaces," *Antennas and Propagation, IEEE Transactions on,* vol. 53, pp. 1904-1911, 2005.

[91] R. Dickie, R. Cahill, H. Gamble, V. Fusco, M. Henry, M. Oldfield*, et al.*, "Submillimeter wave frequency selective surface with polarization independent spectral responses," *Antennas and Propagation, IEEE Transactions on,* vol. 57, pp. 1985-1994, 2009.

[92] F. Birbir, J. Shaker, and Y. M. Antar, "Chebishev bandpass spatial filter composed of strip gratings," *Antennas and Propagation, IEEE Transactions on,* vol. 56, pp. 3707-3713, 2008.

[93] K. Sarabandi and N. Behdad, "A frequency selective surface with miniaturized elements," *Antennas and Propagation, IEEE Transactions on,* vol. 55, pp. 1239-1245, 2007.

[94] F. Bayatpur and K. Sarabandi, "Multipole spatial filters using metamaterial-based miniaturized-element frequency-selective surfaces," *Microwave Theory and Techniques, IEEE Transactions on,* vol. 56, pp. 2742-2747, 2008.

[95] M. Moallem and K. Sarabandi, "A single-layer metamaterial-based polarizer and bandpass frequency selective surface with an adjacent transmission zero," in *Antennas and Propagation (APSURSI), 2011 IEEE International Symposium on*, 2011, pp. 2649-2652.

[96] M. Moallem and K. Sarabandi, "Miniaturized-element frequency selective surfaces for millimeter-wave to terahertz applications," *Terahertz Science and Technology, IEEE Transactions on,* vol. 2, pp. 333-339, 2012.

[97] H. Sharifi, R. R. Lahiji, H.-C. Lin, P. D. Ye, L. P. Katehi, and S. Mohammadi, "Characterization of Parylene-N as flexible substrate and passivation layer for microwave and millimeter-wave integrated circuits," *Advanced Packaging, IEEE Transactions on,* vol. 32, pp. 84-92, 2009.

[98] R. E. Collin, *Field theory of guided waves* vol. 2: IEEE press New York, 1991.

[99] M. Moallem and K. Sarabandi, "Polarimetric study of MMW Imaging Radars for Indoor Navigation and Mapping," *Antennas and Propagation, IEEE Transactions on,* vol. 62, 2014.

[100] M. Moallem and K. Sarabandi, "Y-band phenomenology of indoor environment," in *Antennas and Propagation Society International Symposium (APSURSI), 2010 IEEE*, 2010, pp. 1-4.

[101] P. V. Hough, "Method and means for recognizing complex patterns," ed: Google Patents, 1962.

[102] J. Wang and P. J. Howarth, "Use Of The Hough Transform In Automated Lineament," *Geoscience and Remote Sensing, IEEE Transactions on,* vol. 28, pp. 561-567, 1990.

[103] K. Sarabandi, F. T. Ulaby, and M. A. Tassoudji, "Calibration of polarimetric radar systems with good polarization isolation," *Geoscience and Remote Sensing, IEEE Transactions on,* vol. 28, pp. 70-75, 1990.

[104] S. Uysal and H. Aghvami, "Synthesis, design, and construction of ultra-wide-band nonuniform quadrature directional couplers in inhomogeneous media," *Microwave Theory and Techniques, IEEE Transactions on,* vol. 37, pp. 969-976, 1989.

[105] A. Podell, "A high directivity microstrip coupler technique," in *Microwave Symposium, G-MTT 1970 International*, 1970, pp. 33-36.

[106] R. Sharma, S. Vinayak, D. Rawal, A. Kumar, and U. Ray, "RF parameter extraction of MMIC nichrome resistors," *Microwave and Optical Technology Letters,* vol. 39, pp. 409-412, 2003.

[107] S. Horst, S. Bhattacharya, S. Johnston, M. Tentzeris, and J. Papapolymerou, "Modeling and characterization of thin film broadband resistors on LCP for RF applications," in *Electronic Components and Technology Conference, 2006. Proceedings. 56th*, 2006, p. 5 pp.